

Abstract

A Tale of Two Nanowires: The Biochemical and Spectroscopic Characterization of the Conductive Cytochrome OmcS and OmcZ Filaments of *Geobacter sulfurreducens*

John Patrick O'Brien III

2020

The conductive filamentous appendages of common soil bacterium *Geobacter sulfurreducens* are commonly referred to as “microbial nanowires” because they perform critical roles in long-range extracellular electron transfer for respiration and interspecies electron exchange. They have been invoked to explain a wide range of globally important redox phenomena that influence carbon and mineral cycling in soils and sediments, bioremediation, corrosion, and anaerobic conversion of organic wastes to electricity in microbial fuel cells. However, these filaments' composition, structure, and underlying conduction mechanism have remained uncertain because the filaments are difficult to solubilize for studies using traditional biochemical methods or structural techniques like X-ray crystallography. Herein I present methods for the growth of *Geobacter* cultures in microbial fuel cells where cells need nanowires for survival and protocols for purifying the conductive filaments for in-depth studies.

The nanowires were previously thought to be type IV pili composed of the protein PilA. Here, I report a 3.7 Å resolution cryo-electron microscopy structure which surprisingly reveals that, rather than PilA, the *G. sulfurreducens* nanowires are assembled by micrometer-long polymerization of the hexaheme cytochrome OmcS, with hemes packed within 3.5–6 Å of each other. The inter-subunit interfaces show unique structural

elements such as inter-subunit parallel-stacked hemes and axial coordination of heme by histidines from neighboring subunits. I also find that the midpoint reduction potential of the OmcS nanowires is -157 mV vs. SHE, comparable to periplasmic cytochromes, which, along with the structure, helps explain the remarkable capacity of these soil bacteria to transport electrons to remote electron acceptors for respiration and energy sharing in its natural environment.

I further show that applying an electric field to electricity-producing *Geobacter sulfurreducens* biofilms stimulates the production of octaheme cytochrome OmcZ nanowires with 1,000-fold higher conductivity (30 S cm^{-1}) and threefold higher stiffness (1.5 GPa) than the OmcS nanowires. The higher conductivity of the OmcZ nanowires enables *Geobacter* to form conductive biofilms with the ability to transport electrons over hundreds of micrometers.

I then dive deeper into the structure-function relationship of both filaments by tracking conformational changes as pH is lowered, a condition which was previously shown to significantly increase conductivity. I combine my bulk spectroscopy studies with a chemical imaging-based nanospectroscopy approach to observe low pH-induced conformational switching to β -sheets in individual OmcS and OmcZ nanowires, which increases their stiffness and conductivity by 100-fold due to enhanced π -stacking of heme groups; this was further confirmed by computational modeling and bulk spectroscopic studies. Additional UV-vis, electron paramagnetic resonance, and X-ray absorption spectroscopy studies on OmcS nanowires reveal that at low pH, half of the hemes lose their axial histidine coordination. UV-vis and circular dichroism spectroscopy, coupled with computational studies, reveal strong excitonic coupling in the OmcS nanowires at

low pH, suggesting a face-to-face rearrangement of hemes to form J-aggregate-like structures with greater π - π stacking which could produce the enhanced conductivity. These nanowires can transduce mechanical and chemical stimuli into electrical signals to perform sensing, synthesis and energy production. Therefore, these findings of biologically produced, highly conductive protein nanowires may help to guide the development of seamless, bidirectional interfaces between biological and electronic systems.

**A Tale of Two Nanowires:
The Biochemical and Spectroscopic Characterization of
the Conductive Cytochrome OmcS and OmcZ
Filaments of *Geobacter sulfurreducens***

A Dissertation
Presented to the Faculty of the Graduate School
of
Yale University
In Candidacy for the Degree of
Doctor of Philosophy

by
John Patrick O'Brien III

Dissertation Director: Nikhil S. Malvankar

December 2020

Copyright © 2021 by John Patrick O'Brien III
All rights reserved.

Table of contents

Abstract	i
Table of contents	vi
List of Figures	ix
Acknowledgments	xi
Abbreviations	xiii
1. Introduction	1
1.1 Electromicrobiology	1
1.2 Extracellular electron transfer to insoluble minerals and electrodes	2
1.2.1 Direct vs. indirect extracellular electron transfer	4
1.3 <i>Geobacter</i> biofilms in microbial fuel cells	6
1.4 Prior attempts to identify the conductive filaments in <i>G.s.</i> biofilms	7
1.5 Thesis Organization	8
2 Culturing <i>Geobacter sulfurreducens</i> and purifying filaments	10
2.1 Introduction.....	10
2.2 Results.....	11
2.2.1 Using a gassing station to culture anaerobic bacteria in liquid cultures	11
2.2.2 Principles of microbial fuel cell architecture and growth principles.....	16
2.2.3 Culturing <i>Geobacter sulfurreducens</i> in microbial fuel cells.....	17
2.2.4 Evaluating MFC-grown biofilms	20
2.2.5 Extracting the OmcS and OmcZ nanowires	20
2.3 Discussion	25
3 Discovering the OmcS and OmcZ nanowires	26
3.1 Author Contributions	26
3.2 Introduction.....	27
3.3 Results.....	27
3.3.1 <i>G. sulfurreducens</i> uses OmcS nanowires for critical iron reduction in its native environment.....	27
3.3.2 <i>G. sulfurreducens</i> uses OmcZ nanowires when grown in engineered biofilm environments where long-range electron transfer is required for survival.....	38
3.3.3 The OmcZ nanowires are 1,000-fold more conductive than OmcS nanowires	52
3.4 Discussion: revisiting the role of PilA	57
4 Determining the mechanism of pH-induced increase in nanowire conductivity	59

4.1	Author Contributions	59
4.2	Introduction.....	60
4.3	Results.....	61
4.3.1	Lowering pH induces an increase in conductivity, shrinking of diameter, and increase in stiffness for both OmcS and OmcZ nanowires	61
4.3.2	Spectroscopic insights into pH induced changes in OmcS and OmcZ protein structure.....	63
4.3.3	Low pH induces change in histidine coordination in OmcS nanowires.....	70
4.3.4	Evidence of excitonic coupling in OmcS nanowires at low pH.....	78
4.4	Discussion.....	81
5	Identifying the pathway for electrons in <i>Geobacter</i> extracellular electron transfer and implications in the field	85
5.1	Introduction.....	85
5.2	Results.....	86
5.2.1	The OmcS nanowires have a midpoint reduction potential comparable to periplasmic cytochromes for efficient electron transfer	86
5.3	Discussion.....	90
6	Conclusions & Next Steps	91
6.1	Conclusions.....	91
6.2	Future Directions	92
7	Methods.....	95
7.1	SDS-PAGE	95
7.2	Immunoblotting.....	95
7.3	Mass spectrometry	96
7.4	Bacterial strains and growth conditions.....	96
7.5	AFM sample preparation	97
7.6	Nanoelectrode design and fabrication.....	100
7.7	IR <i>s</i> -SNOM on individual proteins.....	101
7.7.1	Deconvolution and peak fitting of amide I spectra for IR <i>s</i> -SNOM and bulk FTIR	103
7.8	Conducting-probe atomic force microscopy (CP-AFM) measurements	104
7.9	Conductivity calculations.....	105
7.10	Stiffness measurements.....	106
7.11	Grazing-incidence X-ray microdiffraction (GI μ XRD).....	107
7.12	FTIR.....	108
7.13	Raman spectroscopy	109
7.14	CD spectroscopy	109

7.15	Fluorescence microscopy of nanowires	110
7.16	Molecular Dynamics	111
7.17	EPR Spectroscopy	112
7.17.1	EPR Analysis	113
7.18	X-ray absorption spectroscopy	114
7.19	UV-Vis spectroscopy	114
7.20	UV-vis Spectral Simulations	115
7.21	Spectroelectrochemistry Experiments	115
8	References	117

List of Figures

Figure 1.1 Model for physiologically distinct roles of OmcS and OmcZ nanowires	5
Figure 2.1 Gassing station manifold design	13
Figure 2.2 Preparation of anaerobic media using the gassing station	15
Figure 2.3 MFC Schematic	19
Figure 2.4 Improvement of Filament Purification Purity after Optimizing Purification Protocol	22
Figure 2.5 SDS-PAGE Gels Show Purified OmcS and OmcZ from Filament Purification Studies	24
Figure 3.1 Biochemical Characterizations of Filaments show PilA and OmcS Proteins	29
Figure 3.2 Structure of Microbial Nanowires Reveals Closely Stacked Hemes in an OmcS Filament.	30
Figure 3.3 <i>De Novo</i> Atomic Model Building of OmcS Filaments	32
Figure 3.4 Subunit Interface Interactions within OmcS Filament.....	34
Figure 3.5 Electric Field Stimulates Production of OmcZ Filaments	40
Figure 3.6 Mass Spectrometry and Immunoblotting of Filament Preparations Confirm Current-producing Biofilms Induce Overexpression of OmcZ.....	42
Figure 3.7 AFM Imaging of Nanowires produced by $\Delta omcS$ Strain	44
Figure 3.8 Immunogold Labelling Shows Presence of OmcZ Nanowires.....	45
Figure 3.9 IR s-SNOM Imaging of Bacteriorhodopsin (bR) confirms α -helical Structure	48

Figure 3.10 Bulk FTIR and IR s-SNOM Confirm Lysozyme Structure and IR s-SNOM Spectroscopy of OmcS Nanowires Agrees with Cryo-EM Structure	49
Figure 3.11 IR Nanospectroscopy Confirms OmcZ Nanowires in Biofilms Grown Under Electric Field.....	51
Figure 3.12 OmcZ nanowires show 1,000-fold higher conductivity than OmcS ...	53
Figure 3.13 OmcZ Nanowires Show Improved π -stacking between Hemes Versus OmcS and Protonation Enhances π -stacking	55
Figure 4.1 The OmcS and OmcZ nanowires show reduction in diameter, increase in conductivity, and increase in stiffness as pH is lowered	62
Figure 4.2 Nanoscale IR Spectroscopy Establishes pH-induced Structural Transition in OmcS and OmcZ Nanowires.....	65
Figure 4.3 Raman, CD, and Fluorescence Spectroscopy Further Demonstrates pH-induced Structural Transition in OmcS and OmcZ Nanowire Containing WT and W51W57 Samples, Respectively	67
Figure 4.4 Bulk FTIR Spectra of OmcS and OmcZ Nanowires Show Transition to β -sheets at pH 2 and Conformation Change is Independent of Buffers	68
Figure 4.5 Loss of Axial Histidine Ligand to Heme at pH 2 in OmcS Nanowires.	72
Figure 4.6 X-Ray Absorption Spectroscopy Revealed a Loss of Axial Coordination by Histidine in OmcS Nanowires at pH 2.....	75
Figure 4.7 Experimental and Computed UV-Vis Spectra of Nanowires Confirm the Loss of Axial Histidine Coordination at pH 2.	77
Figure 4.8 Evidence for Excitonic Coupling in OmcS Nanowires	80
Figure 5.1 Redox Characterization of OmcS Nanowires	87

Acknowledgments

It takes more than a village to complete a Ph.D., and I was fortunate to have endless support while I completed my dissertation. I first want to thank Nikhil for providing fantastic mentorship and direction. His curiosity and drive were an inspiration during tough times and I always felt like he had my best interests at heart. I would also like to thank the members of my thesis committee – Gary Brudvig, Joe Howard, and Victor Batista. Gary was a crucial resource and collaborator on many projects, and in the rare circumstance where he wouldn't know the answer, he would know a reference or the name of someone who could help. Joe's keen eye for the big picture and helped keep my research on track and provided perspective. Victor was helpful as a computational resource for complementing the experimental work completed in this thesis. This thesis is extremely interdisciplinary, and I wouldn't have been able to complete it without the help of many members of the Malvankar lab, especially Yangqi Gu, Sibel Yalcin, Sophia Yi, Vishok Srikanth, Winston Huynh, and Cong Shen. Jackie I would also like the MB&B Department and the PEB program for providing supportive communities over the years. I thank Steven Symes and Kristin Whitson, my undergraduate research advisors, for giving me a chance at research and for inspiring me to pursue a graduate degree in the first place.

My family has been extremely supportive during this time, and I am eternally grateful to them for their love and support – even if they don't know exactly what I'm doing all day. I have too many friends to thank individually, but will mention a few: West Campus was lonely at first because I joined a new lab, but many members of the Jacobs-

Wagner lab reached out and became close friends, including William Gray, Sander Govers, Brad Parry, Skye Glenn, and Zach Kloos. My dog Juniper was a wonderful support for my mental health during the later years of my degree, but I could not have done it alone: I am grateful to Skye for her help raising and taking care of Juniper, Nathan and Kaury Kucera and their family for always being willing to watch Juniper or provide any help I needed while I lived in New Haven, and my neighbor Liam who would walk Juniper when I had to stay late in lab. Chelsea Standish was the first person to tell me to do a Ph.D. instead of becoming a dentist, and for that I'm not sure I should be thankful or angry. Lastly, my close friends from the UTC track and cross-country team were my family away from family, and our yearly retreats were a refuge of nostalgia I would look forward to all year.

Abbreviations

AFM	Atomic Force Microscopy
bR	Bacteriorhodopsin
CD	Circular Dichroism
Cryo-EM	Cryo Electron Microscopy
DIET	Direct Interspecies Electron Transfer
DMRB	Dissimilatory Metal-Reducing Bacteria
EET	Extracellular Electron Transfer
EPR	Electron Paramagnetic Resonance
FTIR	Fourier Transform Infrared
GIμXRD	Grazing Incidence micro-x-ray diffraction
HS	High Spin
IR	Infrared
LCSM	Laser Confocal Scanning Microscopy
LS	Low Spin
MFC	Microbial Fuel Cell
MD	Molecular Dynamics
NMR	Nuclear Magnetic Resonance
OmcS	Outer Membrane Cytochrome S
OmcZ	Outer Membrane Cytochrome Z
SHE	Standard Hydrogen Electrode
ThT	Thioflavin T
TEM	Transmission Electron Microscopy
WT	Wild-type
XAS	X-ray Absorption Spectroscopy

1. Introduction

What's in a name?

While this thesis focuses on the discovery and characterization of two *Geobacter sulfurreducens* nanowires, as suggested by the title, the tale of *Geobacter* filaments dates back more than ~18 years ago when Childers *et al.* discovered that *Geobacter metallireducens* produces proteinaceous filaments to grow on insoluble Fe(III) oxides (Childers, Ciufo et al. 2002). At the time, and for the next decade or so, the filaments were proposed to be Type IVa pili – assemblies of a single protein (PilA) that are quite common in other gram-negative microorganisms. They were found to be electrically conductive (Malvankar, Yalcin et al. 2014) and were therefore deemed nanowires, as this was a unique characteristic among Type IVa pili. Within this thesis I tell the story of how my work in the Malvankar lab, along with the work of many other lab members and collaborators, led to the discovery that these conductive nanowires are not made up of a single PilA protein, but are actually composed of cytochrome proteins OmcS or OmcZ. Inside the thesis I follow a similar nomenclature to what is found in the field: I use “filament” to refer to any protein-based extracellular assembly, but reserve the title of “nanowire” for those that have the capability to transfer electrons.

1.1 Electromicrobiology

Connecting biological systems to electronic devices once seemed a eutopia set only in the distant future and on the silver screen; the emerging field of electromicrobiology, however, is looking to bridge the gap between the future and the present by studying microorganisms with the capacity to form electrical connections to electronic devices.

Applications in this field range from harvesting electricity from the microbial breakdown of organic matter, wearable electronics, biofuel production, and living electric circuits with the capability to repair themselves (Lovley 2012). A general theme within this field, and in a broad sense this thesis as well, is to first understand the ways in which these microorganisms already use charge transfer to connect and communicate in their natural environments; understanding these *in vivo* electron transfer mechanisms and pathways can then help drive their adaptation for future technologies. Some of the most well-studied microorganisms in this field are those that evolved novel ways to export electrons outside of the cell to complete respiration and generate energy for cell growth and division.

1.2 Extracellular electron transfer to insoluble minerals and electrodes

A key step in cellular respiration comes at the end of the electron transport chain, where the excess electrons resulting from establishing the proton gradient must be eliminated by transferring them to a final electron acceptor in order for the cycle to continue. In bacterial aerobic respiration, these electrons combine with oxygen (O_2) and freely diffusing protons (H^+) in the cytoplasm to form water (H_2O). Anaerobic bacteria, however, often live in harsh environments that lack soluble electron acceptors that can be transported into the cytoplasm to complete respiration; a subset of these bacteria instead utilize redox-active minerals such as Fe(III) and Mn(IV) oxides that are highly prevalent in subsurface soils and aquatic sediments (Schroder, Johnson et al. 2003, Lovley, Holmes et al. 2004), and are thus termed dissimilatory metal reducing bacteria (DMRB). As these minerals are highly insoluble in neutral-pH environments and thus cannot pass through the outer membrane (Lovley, Holmes et al. 2004), DMRB evolved extracellular electron

transfer (EET) pathways to transport electrons outside of the cell. The mechanisms behind how these bacteria transfer electrons through the periplasm and outer membrane to electron acceptors that can be hundreds of cell-lengths away has been widely studied and hotly debated.

In addition to redox-active minerals, many of these bacteria can also exchange electrons with electrodes. This phenomenon has led to extensive studies of these microorganisms in microbial fuel cells (MFCs) – devices where the bacteria act as “biocatalysts” by converting organic compounds to current that is harvested at an electrode. In addition to being a closer match to the end goal of connecting biological systems and abiotic electronic devices to convert waste into useful commodities such as electricity or high-value chemicals, MFCs also provide a more controlled environment to systematically study how DMRB exchange electrons with external electron acceptors. Measuring the current produced by the respiring bacteria allows the determination and comparison of several performance variables such as power density and coulombic efficiency (the fraction of electrons harvested at the electrode versus the theoretical total produced by oxidation of the electron donor) (Logan, Hamelers et al. 2006). Thus, researchers have been able to optimize input variables such as temperature, electrode material, electron donor, make-up of the microbial community (mixed-species vs. pure cultures), and potential at which the electrode is poised (Nevin, Richter et al. 2008, Marsili, Sun et al. 2010). These studies have helped elucidate many inner-workings of the EET mechanisms used by DMRB; for example, work by Levar *et al.* has shown that *Geobacter sulfurreducens* uses two different pathways to transport electrons out of the inner membrane depending on whether they are grown in MFCs poised at low (≤ 0.10 V

vs. standard hydrogen electrode (SHE)) or high (> 0.10 V vs. SHE) potentials (Levar, Hoffman et al. 2017).

1.2.1 Direct vs. indirect extracellular electron transfer

The mechanisms of extracellular electron transfer (EET) are best understood in the context of two DMRB microorganisms: *Shewanella oneidensis* and *Geobacter sulfurreducens*. The pathways for how electrons are transported from the pool of quinones in the inner membrane to the cell surface is relatively well established for some model DRMB microorganisms; however, the final steps of transferring the electrons over large distances to the terminal electron acceptor has widely debated. There are several ways in which DMRB can transfer electrons to an electrode or other electron acceptor. If the cell is at the electrode surface (or in contact with a different acceptor) electrons can transfer from cytochromes imbedded in the outer membrane directly to the electrode. If the electron acceptor is not within tunneling range ($\leq \sim 2$ nm), different species have evolved divergent mechanisms that are typically grouped into “indirect” and “direct” mechanisms of long-distance electron transport.

When long-distance electron transport is required, *S. oneidensis* secretes soluble electron shuttles (flavins) into the surrounding environment to serve as mobile mediators between the cell and terminal electron acceptor (Kotloski and Gralnick 2013). This is commonly referred to as “Indirect EET.” In contrast, *G. sulfurreducens* does not produce flavin molecules or other soluble diffusing mediators (Nevin and Lovley 2000), but instead produces electrically conductive proteinaceous filaments to reach out and form a direct electrical connection (“Direct EET”) between living cells and the external electron acceptor (**Figure 1.1**) (Nevin and Lovley 2000, Reguera, McCarthy et al. 2005).

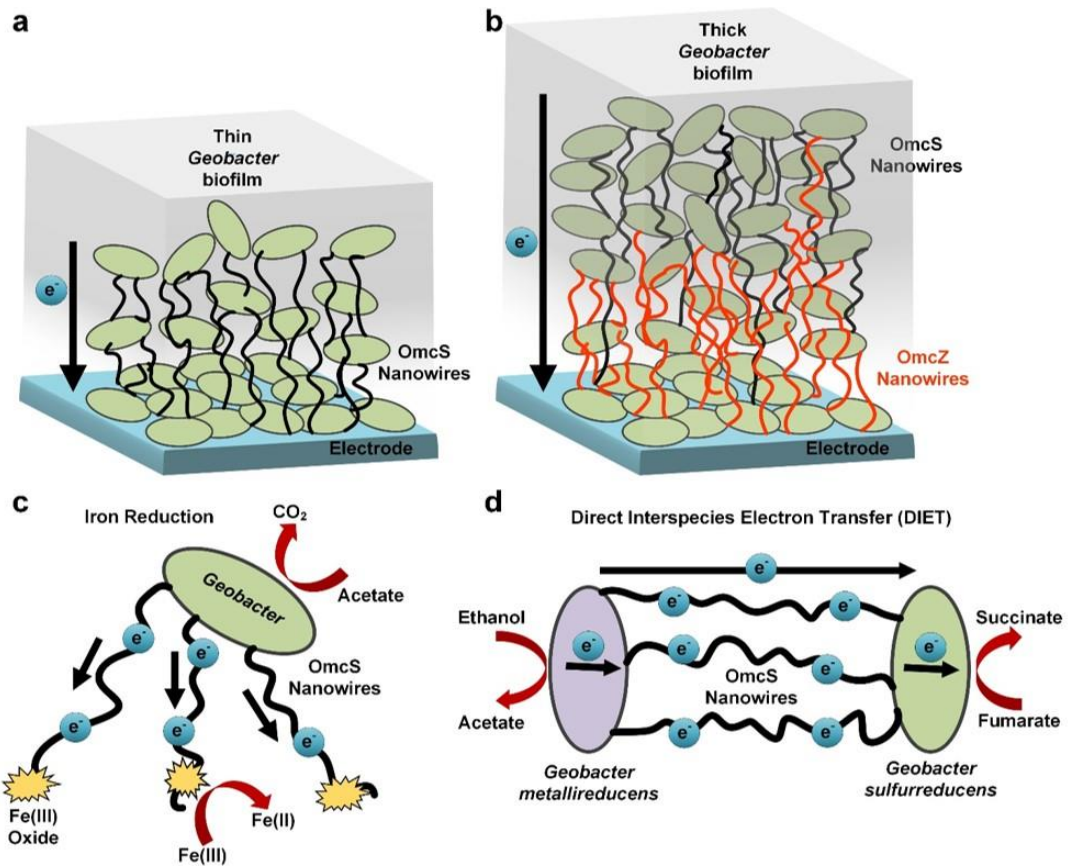


Figure 1.1 Model for physiologically distinct roles of OmcS and OmcZ nanowires

(a) OmcS nanowires are essential for electricity-producing biofilms during initial stages of growth. (b) OmcZ nanowires are essential for the formation of thick, mature biofilms capable of high current density. OmcS nanowires are also essential for (c) iron reduction and (d) direct interspecies electron transfer.

While indirect methods, like producing an electron shuttle, allow many bacteria access to an electrode's surface area, the current density is eventually limited by the diffusion of the mediator (Picioreanu, Head et al. 2007). Additionally, it can be energetically expensive to produce the shuttles, especially if the bacteria are growing in a dynamic environment where the shuttle can be swept away and the bacteria must make more to reestablish their connection to the electrode (Mahadevan, Bond et al. 2006, Ross, Brantley et al. 2009). For these reasons, and more as reviewed elsewhere (Lovley 2012), microorganisms that use direct EET mechanisms typically outperform those that use indirect mechanisms in MFCs (Torres, Marcus et al. 2010). While producing a conductive protein filament for a direct connection is also energetically expensive, the electrical network persists as a permanent power grid in the presence of fluid flow or even after cell death.

1.3 *Geobacter* biofilms in microbial fuel cells

The microbial fuel cells for *G. sulfurreducens* studies are continually sparged with inert anaerobic gas to limit oxygen intrusion and keep the electrode surface as the only terminal electron acceptor. Under these conditions, only bacteria that are electrically connected to the electrode are able to get rid of their electrons and survive. Thus, cells stack on top of each other and overexpress conductive protein filaments to form a multi-layered biofilm that can reach heights of up to ~100 μm (**Figure 1.1b**), where even the cells at the outer edges of the biofilm are viable and still contribute to the measured current (Reguera, Nevin et al. 2006, Malvankar, Tuominen et al. 2012). The conductive biofilm enables *G. sulfurreducens* to produce the highest current densities of any pure culture (Nevin, Richter et al. 2008, Malvankar, Tuominen et al. 2012). Further, elegant

experiments have shown that these biofilms can also behave as transistors (Malvankar, Vargas et al. 2011), super-capacitors (Malvankar, Mester et al. 2012) and that they display a metal-like temperature dependence of conductivity (Malvankar, Vargas et al. 2011). Identifying what protein (or proteins) are conferring these phenomenal behaviors has been a major focus of the *Geobacter* field for the last ~18 years.

1.4 Prior attempts to identify the conductive filaments in *G.s.* biofilms

Seminal work by Childers *et al.* was the first to identify the link between the presence of proteinaceous filaments and the ability of *Geobacter* cultures to complete EET and grow on insoluble Fe(III) oxides (Childers, Ciufo et al. 2002). Since then, it was believed that the conductive filaments were type IVa pili composed of PilA protein, and that the (several) cytochromes identified outside of the cell were monomeric and were performing other roles such as facilitating the transfer of electrons from the conductive pili to the final electron acceptor (Inoue, Leang et al. 2010, Leang, Qian et al. 2010).

Previous studies proposed that the conductive *Geobacter* filaments were type IV pili for a number of reasons: **1)** Electron-transferring cells showed high levels of messenger RNA for PilA (Childers, Ciufo et al. 2002). **2)** The amino acid sequence of *G. sulfurreducens* PilA is similar to the N-terminal sequence of PilA from other type IV pili-producing bacteria (Reguera, McCarthy et al. 2005). **3)** Genomic organization of *G. sulfurreducens* pilus biosynthesis genes was also similar to other type IV pili-producing bacteria (Reguera, McCarthy et al. 2005). **4)** A *pilA* deletion mutant strain lacked filaments and could not transfer electrons extracellularly (Reguera, McCarthy et al. 2005). **5)** Point mutations in *pilA* caused cells to produce filaments with different

conductivities than wild-type (WT) filaments (Vargas, Malvankar et al. 2013, Adhikari, Malvankar et al. 2016, Tan, Adhikari et al. 2016, Tan, Adhikari et al. 2017).

Despite these data, there has never been any direct evidence that the conductive *Geobacter* extracellular filaments are composed of PilA. Instead, the filament composition was inferred from indirect evidence, including the presence of PilA in biochemical analyses (Tan, Adhikari et al. 2016), or from low-resolution imaging by atomic force microscopy (AFM) and negative-staining transmission electron microscopy, which suggested filament dimensions similar to type IV pili (Reguera, McCarthy et al. 2005).

1.5 Thesis Organization

Chapter 2 introduces how to culture *Geobacter* species anaerobically in liquid cultures and in microbial fuel cells (MFCs), where fumarate and poised electrodes serve as the terminal electron acceptors, respectively. A protocol for purifying filaments from cultures grown by either method is also presented, which sets the stage for the many important discoveries and experiments in later chapters.

Chapter 3 details the discovery that the conductive filaments produced by *Geobacter sulfurreducens* are not composed of the protein PilA, but rather of either the hexaheme cytochrome OmcS or the octaheme cytochrome OmcZ. The chapter ends by revisiting the role of PilA considering these findings.

Chapter 4 dives into characterizing both nanowires as a function of pH, specifically aiming to shed light on the mechanism behind an increase in conductivity at low pH. It is shown that low pH induces a structural shift to more β -sheet-like structures in both

filaments. Further studies on the OmcS heme electronic environments provide evidence that low pH also induces a change in spin state and an increase in heme stacking.

Chapter 5 discusses how to reconcile the discovery of the OmcS nanowires into the *G. sulfurreducens* models for extracellular electron transfer. The filament redox midpoint potential is determined which helps resolve some long-standing confusion in the *Geobacter* field about the extracellular electron transfer pathway to physiologically important electron acceptors.

Chapter 6 summarizes the findings of this thesis within the context of the *Geobacter* field and details how these results can shape future work.

Chapter 7 includes the methods used for the thesis in detail

2 Culturing *Geobacter sulfurreducens* and purifying filaments

2.1 Introduction

Portions of this chapter have been adapted from previously published works:

O'Brien J.P., Malvankar, N.S. (2016) A Simple and Low-Cost Procedure for Growing *Geobacter sulfurreducens* Cell Cultures and Biofilms in Bioelectrochemical Systems
Curr. Protoc. Microbiol. 43:A.4K.1-A.4K.27

Geobacter sulfurreducens has been used as a model organism to study the mechanisms behind extracellular electron transfer (EET) for several reasons: it was the first of the *Geobacter* species to have its genome sequenced (Methe, Nelson et al. 2003) and have genetic tools developed (Coppi, Leang et al. 2001); it performs important roles in the biogeochemistry of a diversity of aquatic soils and sediments (Nevin and Lovley 2002); when grown in microbial fuel cells where long-distance electron transfer is required for completing respiration, it produces conductive protein nanowires with conductivities that rival those of synthetic metallic nanostructures (Malvankar, Vargas et al. 2011), allowing cultures to form thick biofilms that produce the highest current density of any known pure culture (Nevin, Richter et al. 2008).

This chapter will detail how *Geobacter* is cultured, noting improvements to prior protocols and technologies. Following the description of how to culture *Geobacter* strains, I will discuss the current purification protocol for purifying filaments for further studies.

2.2 Results

2.2.1 Using a gassing station to culture anaerobic bacteria in liquid cultures

All *Geobacter* species are obligate anaerobes; therefore care must be taken to ensure they are grown in an anaerobic environment. There are a variety of methods and systems available to grow anaerobic microorganisms at the bench as well as in microbial fuel cell systems (Beyenal and Babauta 2015), and many such methods have been previously reviewed in detail. For example, Reguera and colleagues (Speers, Cologgi et al. 2009) reviewed the principles and techniques used in anaerobic gassing stations. This equipment is an integral part of anaerobic research in a laboratory because it facilitates the maintenance of an anaerobic environment for the growth and transfer of cultures routinely on a bench without any need for cumbersome anaerobic glove chambers (glove boxes). In addition, gassing stations allow rapid preparation of anaerobic medium. However, many of these methods are cumbersome and expensive.

In this section, I present a simple design for constructing a gassing station that can be followed by an inexperienced investigator using items that can be purchased off the shelf for the cultivation of anaerobic microorganisms. Further, I will also describe a simplified protocol for preparing anoxic media to grow anaerobic microorganisms using this gassing station.

Many modern gassing stations are derivatives of the Hungate technique that was originally developed in 1969 by Hungate and Nottingham. Gassing stations remove O₂ by sparging (“bubbling”) inert gases (traditionally N₂ and CO₂) into the medium with a sealed cap in place (described in detail below). The continual sparging of the inert gases

removes dissolved O₂ from the medium and the headspace of the vessel. To purify the inert gases, the traditional Hungate technique requires pretreatment of a copper column with hydrogen (H₂) gas and heating the column to 350°C before the sparging process can be carried out. While many investigators use variations of the Hungate technique, gassing stations have still traditionally needed to be built manually which can be inconvenient for the inexperienced investigator. For example, in order to create an oxygen-free environment, a common approach is to use copper-filled glass columns wrapped in a heating tape, which still needs to be pre-reduced with hydrogen (Speers, Cologgi et al. 2009). Thus, a typical gassing station also requires separate gas cylinders for nitrogen, hydrogen, and carbon dioxide, making the whole assembly cumbersome. The need for manual construction is a barrier for inquiring scientists looking to incorporate anaerobic components into their investigations. Here, I describe the assembly of a gassing station with a simplified gassing manifold that we have designed and made commercially available. This manifold significantly reduces assembly complexity and resolves complications of the Hungate technique. For one, it replaces the need for H₂ pretreatment and the heating of a copper column by including an Supelco supelpure-O oxygen trap in the gas line (**Figure 2.1a,b**), thus eliminating the use of flammable gases as well as the glass columns filled with copper filings that are typically powered by bulky rheostats. The gassing station with this new design can be purchased off the shelf and readily mounted on a lab bench, and the only requirements of the researcher are attaching copper tubing from the gas tanks to the manifold itself.

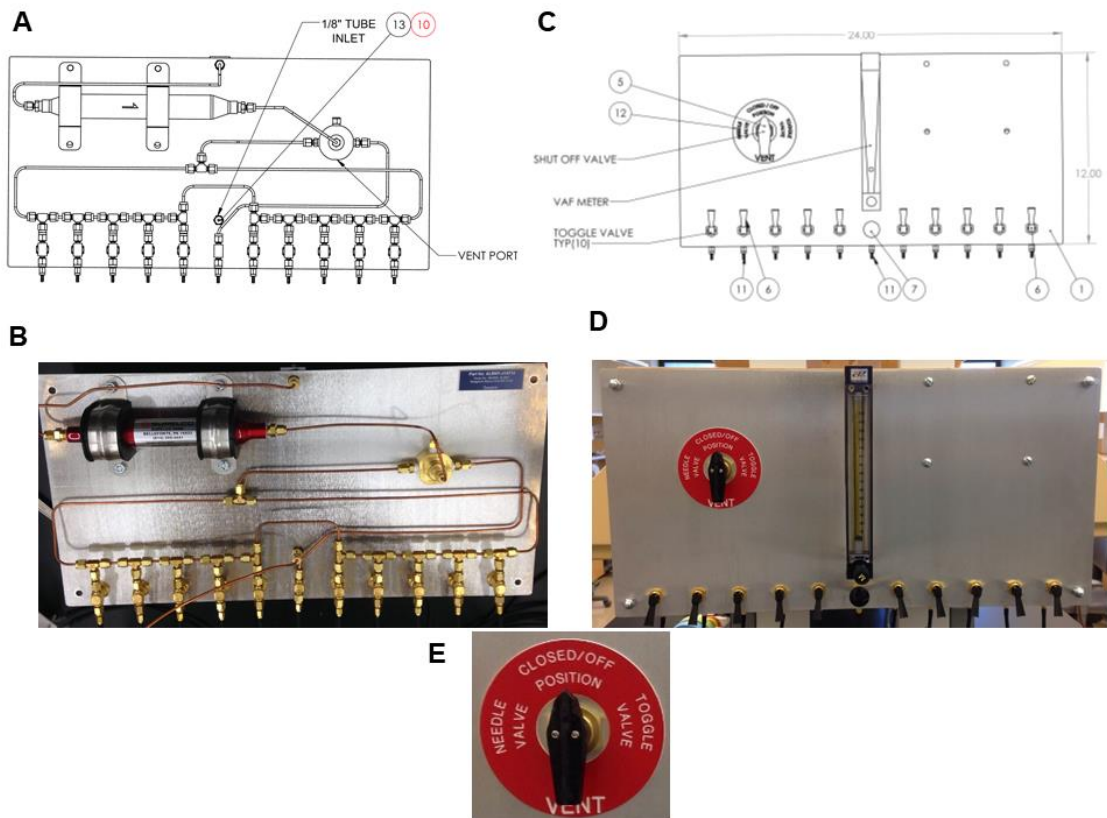


Figure 2.1 Gassing station manifold design

(a) Design and (b) picture of the back of the manifold, showing the Supelco oxygen trap in the top left of each picture. (c) Design and (d) picture of the front of the manifold. (e) zoomed picture of the control panel switch, showing the ability to use the needle valve setting for fine-tuned control of flow rate through one port, and the toggle valve setting where multiple ports (up to 10 in this design) can be used simultaneously.

The full protocol for using this gassing manifold to prepare anaerobic media is presented in (O'Brien and Malvankar 2016) but I will recapitulate the major steps here: first, the media is sparged with the cap open with the canula (for media volumes less than 1 liter) or a sparger (for media volumes greater than 1 liter) resting at the bottom of the media solution (**Figure 2.2a**). Second, the vessel is closed with a butyl rubber stopper so that O₂ flow back into the bottle is limited (**Figure 2.2b**). Third, while holding the butyl stopper in place, the canula is lifted into the headspace (air just above the media) and the headspace is sparged. Finally, the cannulas are removed and the vessels sealed with aluminum crimps to provide a tight seal for long-term storage and the media is ready to be sterilized in an autoclave.

Initially growing the bacteria in anaerobic vessels gets the cultures to mid-exponential growth phase, which greatly increases the probability of survival during the transfer into the microbial fuel cell. Furthermore, several transfers are completed between anaerobic vessels to dilute cryogenic agents present in freezer stocks (dimethyl sulfoxide (DMSO) is commonly used for *Geobacter* cultures). This approach can also be adapted for culturing large volumes (~10 liters) of mutant *Geobacter* strains that can produce filaments when grown using fumarate as the electron acceptor (described below).

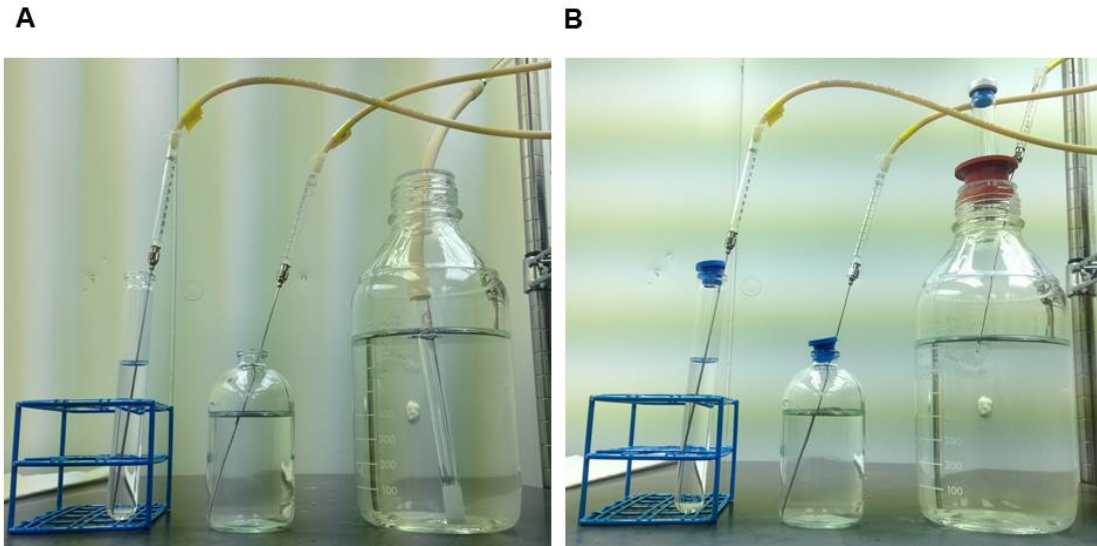


Figure 2.2 Preparation of anaerobic media using the gassing station
Sparging of media with **a**, the vessel open and **b**, the vessel sealed by a butyl stopper. From left to right, the examples include a 10 mL pressure tube, a 125 mL serum bottle, and a 1-liter bottle.

2.2.2 Principles of microbial fuel cell architecture and growth principles

Microbial fuel cells have gained considerable interest in the past few years due to their ability to harness the catalytic activity of anaerobic microorganisms for the production of commodity chemicals, bioenergy, and biofuels (Logan and Rabaey 2012, Lovley and Nevin 2013). In this section I present the low-cost assembly of a microbial fuel cell and outline a simplified procedure for cultivating and analyzing bacterial cell cultures and biofilms that produce electric current. The methods provided here can be readily expanded to other anaerobic microorganisms and to MFCs with different configurations.

A typical two-chambered microbial fuel cell (**Figure 2.3**) uses microorganisms to catalyze an oxidation and reduction reaction at an anodic and cathodic electrode, respectively (Logan, Hamelers et al. 2006, Beyenal and Babauta 2015). The two electrodes are separated by a proton-exchange membrane for the selective passage of protons generated at the anode chamber. Alternatively, both electrodes can be placed in a single chamber; however, the protons accumulated in the chamber as well as other reactive species present in the medium can undermine MFC performance by affecting microbial growth or introducing other limitations (Logan, Hamelers et al. 2006, Beyenal and Babauta 2015).

Current generation at the anode relies upon oxidation of organic and/or inorganic electron donors such as sodium acetate, waste organics, and sulfides. At the cathode, an electron acceptor such as oxygen, nitrate, or potassium ferricyanide is reduced (Beyenal and Babauta 2015). In an MFC the anode and the cathode are connected through an electrical circuit, and can be run under conditions where electrical energy is generated

from the circuit or under conditions where electrical energy is supplied to the electrodes to change the potentials of the anode or cathode.

To generate electricity in an MFC, the anode and cathode need to maintain appropriate electrical potentials that are thermodynamically favorable for electron transfer from the anode to cathode. If a power supply is not holding the potential difference constant, this depends on the choice of catholyte in the cathode chamber. Oxygen is commonly used because it is inexpensive and has a high theoretical reduction potential ($E^{\circ} = 0.805$ V vs. SHE), but it has low solubility in water and requires a continuous supply through the liquid in the cathode chamber. Potassium ferricyanide ($E^{\circ} = 0.361$ V versus SHE) is an alternate electron acceptor, but it also needs to be replaced regularly and is not sustainable for long-term growth. On the other hand, the potential of the anode and cathode can be maintained by applying voltage using an external power supply such as a potentiostat. For more accurate control of applied potential, traditionally a three-electrode set-up is used with a reference electrode (typically Ag/AgCl), and the anode serving as the working electrode and the cathode serving as the counter electrode. In addition to the measurements of electrical current in chronoamperometry mode, the potentiostat can be used to perform several electrochemical experiments such as cyclic, square wave, and differential pulse voltammetry, as well as AC impedance spectroscopy. For these reasons, we use the potentiostat method for growing *Geobacter* cultures in MFCs.

2.2.3 Culturing *Geobacter sulfurreducens* in microbial fuel cells

The growth of *Geobacter* cultures in MFCs can be described by three phases: in the first phase, bacteria are transferred into the MFC and cultured in media that contains both

an electron donor (acetate) and a soluble electron acceptor (fumarate). Thus, the bacteria can grow planktonically using fumarate as the electron acceptor or can colonize the electrode surface and use the anode as the electron acceptor. This enables higher probability of bacterial attachment to the electrode and success in the following phases. In the second phase, biofilm growth on the electrode is promoted by removing the spent media and replacing it with fresh media that no longer has fumarate so that the only remaining electron acceptor is the poised anode. During this phase, growth is monitored via the current harvested at the electrode. The bacteria remain in this phase until they utilize all the acetate in the media, which can be indicated by a drop in current. For WT *G. sulfurreducens* strain PCA this can occur at approximately ~1 mA. The MFCs are then switched to flow-through phase, where a peristaltic pump is used to pump in fresh media with electron donor and to remove planktonic cells. Flow-through mode is critical for the growth of multilayer biofilms that can be hundreds of micrometers thick and produce high electric current. The maximum current observed in *G. sulfurreducens* strain PCA is ~12 mA with the MFC setup described in (O'Brien and Malvankar 2016).

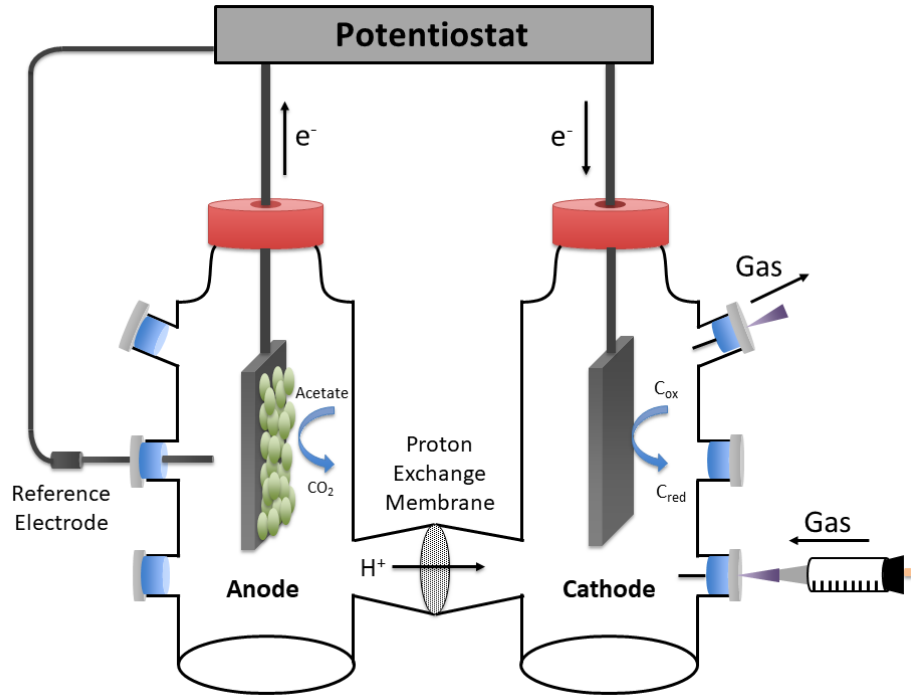


Figure 2.3 MFC Schematic

In the cathode chamber, C_{ox} and C_{red} refer to the oxidized and reduced forms, respectively, of the particular catholyte being used in the experiment. The green ovals represent the cells in the actively respiring biofilm.

2.2.4 Evaluating MFC-grown biofilms

Once the biofilm is grown and is producing stable current, the MFC can be disassembled and the anode removed and placed in a petri dish for further analysis. To analyze an intact biofilm, biofilms grown on electrodes can be imaged either with Scanning Electron Microscopy (Malvankar, Tuominen et al. 2012) or Laser Confocal Scanning Microscopy (LCSM) (Malvankar, Vargas et al. 2011, Malvankar, Lau et al. 2012). Both methods can provide information about parameters such as biofilm thickness, electrode coverage area, and inhomogeneity in the biofilm growth. LCSM requires staining the bacterial cells with fluorescent live-dead stains (*e.g.*, BacLight viability kit by Invitrogen). For the measurement of intrinsic biofilm parameters such as electrical conductivity, a slightly modified design of MFC is used and the protocol is described in detail elsewhere (Beyenal and Babauta 2015). To analyze total biomass (Malvankar, Vargas et al. 2011) or extraction of pili (Tan, Adhikari et al. 2016) and cytochrome proteins (Malvankar, Mester et al. 2012, Malvankar, Tuominen et al. 2012) from the electrode-grown biofilm, the biofilm is scraped off the electrode gently using a cell scraper and isotonic wash buffer. Determining the electrical properties of biofilms such as electrical conductivity, charge transfer resistance, capacitance, and electron transport rate, is also possible, and a detailed protocol for the experimental design, instrumentation and data analysis is presented elsewhere (Beyenal and Babauta 2015).

2.2.5 Extracting the OmcS and OmcZ nanowires

Prior studies on *Geobacter sulfurreducens* filaments were completed at the nanoscale level where other protein contaminants were not a concern for interfering with data collection or interpretation. However, with the discovery that *G. sulfurreducens* can

produce several types of filaments, and with many of the experiments for this thesis and future work involving bulk studies where other contaminants significantly muddle interpretation, I aimed to optimize our protocols to obtain purified nanowire samples.

I first examined the already existing protocols that purified filaments with a series of ultracentrifugation spins and saturated ammonium sulfate precipitations. I optimized the concentration of SAS to yield the most filaments and fewest impurities, which resulted in samples that predominantly contained OmcS nanowires, as seen in SDS-PAGE gels (**Figure 2.4a**) and solution mass-spectroscopy (**Figure 2.4c**), where the most dominant protein and only heme-containing protein was OmcS. However, to increase the purity further I utilized a series of detergent extractions (details in methods) to remove further impurities as is evident in SDS-PAGE gels (**Figure 2.4b**) and in TEM grids (**comparing Figure 2.4d and Figure 2.4e**).

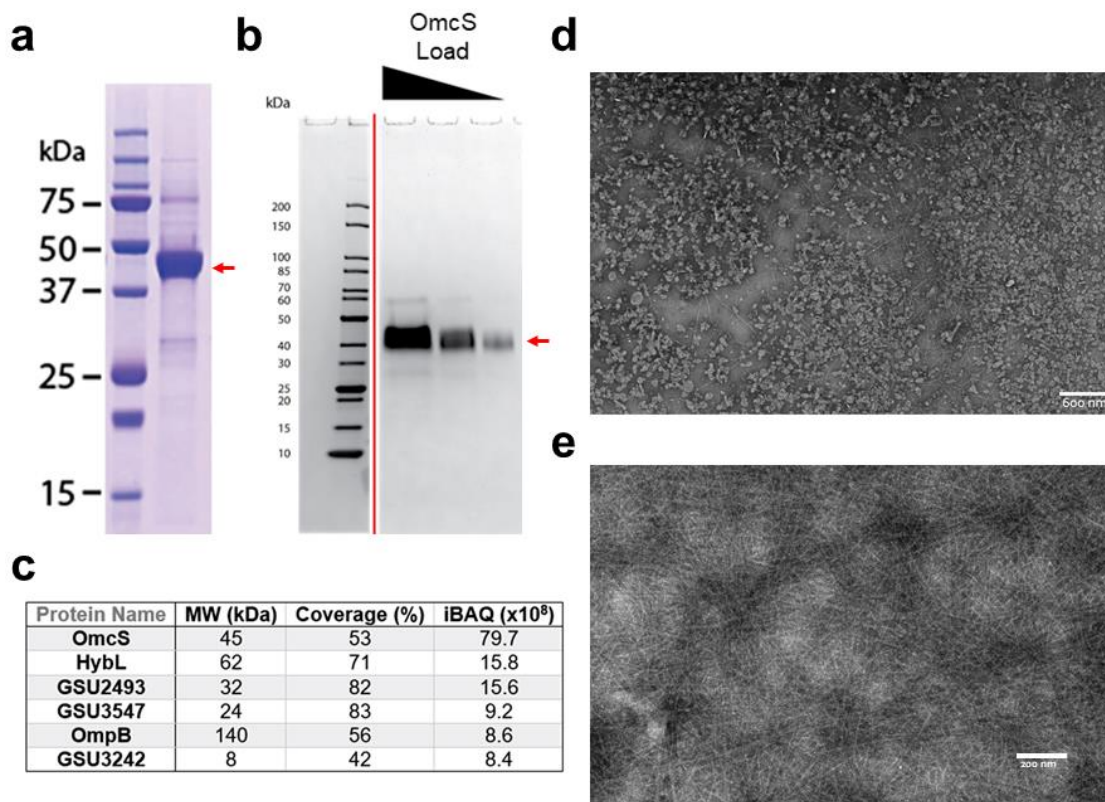


Figure 2.4 Improvement of Filament Purification Purity after Optimizing Purification Protocol

a) SDS-PAGE gel of filament sample from previous purification protocol compared to **(b)** SDS-PAGE gel of optimized purification protocol. **(c)** proteins identified from solution mass-spectrometry of sample used in **(a)**. **(d and e)** are TEM images from the previous protocol **(d)** and the optimized protocol **(e)** showing the successful removal of debris from the sample.

While wild-type (WT) *Geobacter sulfurreducens* can be cultured in liquid media with fumarate acting as a soluble terminal electron acceptor, under these conditions it unfortunately does not produce high amounts of conductive filaments. Therefore in the early stages of my thesis work, culturing *Geobacter* strains under conditions where extracellular electron transfer was required for survival, such as in the microbial fuel cells described earlier in this chapter, was the only way to produce high amounts of filaments. However, there were concerns with the ability to scale up this growth condition as it can take up to one month to get a sample and the overall yield is low (one fuel cell produces ~1 mL of ~0.1-0.5 µg/mL). To remedy this, we investigated several mutant *Geobacter* strains for their ability to produce OmcS and/or OmcZ nanowires when grown in liquid culture.

As wild-type *Geobacter sulfurreducens* can produce both OmcS and OmcZ we evaluated several strains that selectively express either OmcS or OmcZ. Using a $\Delta omcZ$ strain we were able to successfully produce purified samples with OmcS nanowires (**Figure 2.5a**). We also utilized a *G. sulfurreducens* mutant strain (KN400 $\Delta pilT$) that selectively produced OmcZ nanowires when grown in a microbial fuel cell with a poised graphite electrode serving as the terminal electron acceptor (**Figure 2.5b**). Several members in the lab now are working to scale up OmcZ production by developing a strain that selectively produces OmcZ nanowires from liquid culture, and that surely will be key for studying the OmcZ nanowires in more detail.

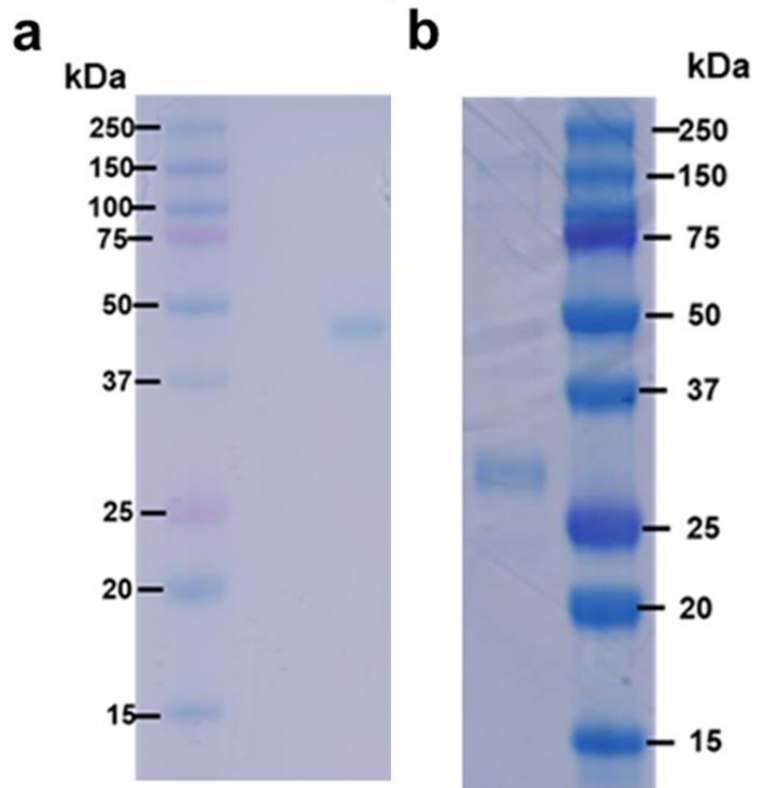


Figure 2.5 SDS-PAGE Gels Show Purified OmcS and OmcZ from Filament Purification Studies

SDS-PAGE gels of filament preparations showing a single band corresponding to (a) OmcS purified from $\Delta omcZ$ strain and (b) OmcZ from the KN400 strain grown in a microbial fuel cell.

2.3 Discussion

Microbial fuel cells are at the heart of *Geobacter* research as they bridge the physiological relevance of their extracellular electron transfer capabilities to the future in their bioelectronics. The work in this chapter is key for both realms, as I hope it **1)** lowers the barrier of entry to the field, **2)** provides a clear and standardized way to reproducibly culture *Geobacter* or other anaerobic microorganisms that can transfer electrons to an external electrode, and **3)** provides a way to purify these nanowires so that their properties can be detailed and the field can advance.

3 Discovering the OmcS and OmcZ nanowires

3.1 Author Contributions

Portions of this chapter have adapted from previously published works:

Wang, F.*, Gu, Y.*, **O'Brien, J.P.**, Yi, S.M., Yalcin, S.E., Srikanth, V., Shen, C., Vu, D., Ing, N.L., Hochbaum, A.I., Egelman, E.H., Malvankar, N.S. (2019) Structure of Microbial Nanowires Reveals Stacked Hemes that Transport Electrons over Micrometers *Cell* **177**, 361-369

O'Brien, J.P.*, Yalcin, S.E.*, Gu, Y., Reiss, K., Yi, S.M., Jain, R., Srikanth, V., Dahl, P.J., Huynh, W., Vu, D., Acharya, A., Chaudhuri, S., Varga, T., Batista, V.S., and Malvankar, S.M., (2020) Electric Field Stimulates Production of Highly Conductive Microbial OmcZ Nanowires *Nature Chemical Biology* **16** 1136-1142

I cultured the *Geobacter* strains in microbial fuel cells and purified the filaments for the work completed in this chapter. I worked with Sophia Yi and Ruchi Jain to complete the biochemical characterization of the filaments. Yangqi Gu prepared and optimized cryo-EM grids, collected the data used to build the atomic model, and carried out AFM imaging and conductivity measurements on wild-type filaments. Fengbin Wang, under the guidance of Ed Egelman, helped refine the OmcS cryo-EM atomic model. Sibel Yalcin built the IR *s*-SNOM setup, collected the data, and completed the analysis. Vishok Srikanth and Yangqi Gu completed the immunogold transmission electron microscopy, and Sibel Yalcin completed the immunogold AFM labeling. Krystle Reiss built the

OmcZ model and performed simulations with help from Peter Dahl under the guidance of Victor Batista. Sibel Yalcin and Tamas Varga performed XRD measurements and analyzed data with Yangqi Gu. I, along with all authors, helped write the manuscripts this chapter was based upon.

3.2 Introduction

As discussed in the introduction (in Section 1.4), for the last ~18 years the *Geobacter* field has believed that the conductive filaments required for growth on extracellular electron acceptors were composed of type IVa pili protein PilA; the initial goals of the work in this chapter, in fact, were to solve the structure of a PilA nanowire. With the breakthroughs in producing high quantities of filaments discussed in the previous chapter we were able to get high-resolution structural data and we were able to put together the pieces to support the alternative hypothesis that PilA is important, but that different proteins comprise the filament.

3.3 Results

3.3.1 *G. sulfurreducens* uses OmcS nanowires for critical iron reduction in its native environment

I initially set out to obtain an atomic-level structure of the conductive *G. sulfurreducens* nanowire(s), a project that would require pure samples with many filaments. Therefore, I grew wild-type (WT) cultures using the anodes of microbial fuel cells as the sole electron acceptors (O'Brien and Malvankar 2016). These growth conditions promote production of conductive biofilms and filaments as well as overexpression of PilA in comparison with growth on soluble electron acceptors such as

fumarate (Malvankar, Vargas et al. 2011). Consistent with previous studies (Tan, Adhikari et al. 2016), I confirmed the presence of both PilA and OmcS with expected molecular weights of ~6.5 kDa and ~45 kDa, respectively, in the filament preparations using polyacrylamide gel electrophoresis (SDS-PAGE), peptide mass spectrometry, and western immunoblotting (**Figure 3.1 and Methods section**).

Cryo-EM images of filaments purified from the WT strain showed a sinusoidal morphology with a period of ~200 Å (**Figure 3.1a**). Averaged power spectra from cryo-EM projections revealed that multiple filaments show a meridional layer line at $\sim 1/(47 \text{ \AA})$, establishing that there are ~4.3 subunits per turn of a ~200 Å pitch 1-start helix (**Figure 3.2b**). Using the iterative helical real space reconstruction (IHRSR) approach (Egelman 2000), we were able to reach a resolution where the handedness of the helices was clearly visible. The 1-start filament helix was left-handed, with a rise per subunit of 46.7 Å and a rotation of -83.1° (**Figure 3.2b**), substantially different than type IV pili that typically show a rise of ~10 Å and a right-handed helix (Wang, Coureuil et al. 2017). The tracing of the C α backbone of the protein subunit at this resolution, 3.7 Å, revealed that the asymmetric unit contained at least 380 residues, which contrasts with the 61 residues present in PilA (Reguera, McCarthy et al. 2005, Reardon and Mueller 2013). Further, there was no apparent internal symmetry that would be expected to arise in the asymmetric unit if it contained multiple copies of identical chains. The NMR structure of PilA (Reardon and Mueller 2013) also failed to fit into the observed EM density map. Surprisingly, we found that there were six hemes per asymmetric unit, with the highest densities in the volume at the centers of these hemes, suggesting the presence of metal atoms.

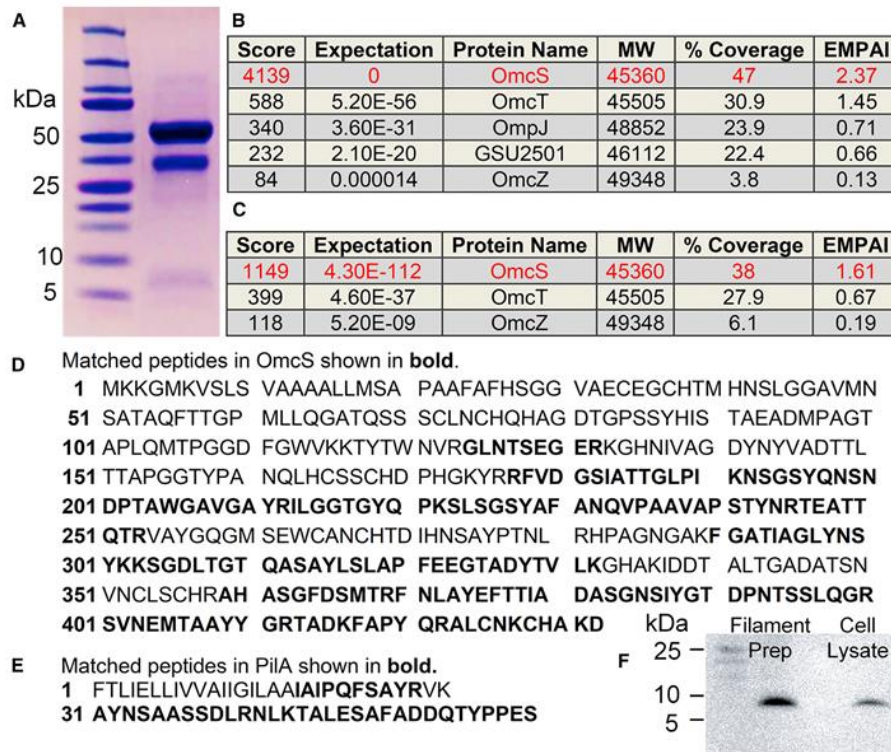


Figure 3.1 Biochemical Characterizations of Filaments show PilA and OmcS Proteins

(a) SDS-PAGE gel of filaments showing OmcS and PilA at expected molecular weights of ~45 kDa and ~6.5 kDa. LC-MS/MS analysis of metalloproteins in purified *G. sulfurreducens* filaments from (b) the ~45 kDa band and (c) the ~30 kDa band. EMPAI: Exponentially modified protein abundance index. LC-MS/MS analysis showing matched peptides in (d) OmcS in ~45 kDa band and (e) PilA in the ~6.5 kDa band. (f) Western immunoblotting using anti-PilA antibody showing PilA in purified filament preparations (left) and cell lysate (right).

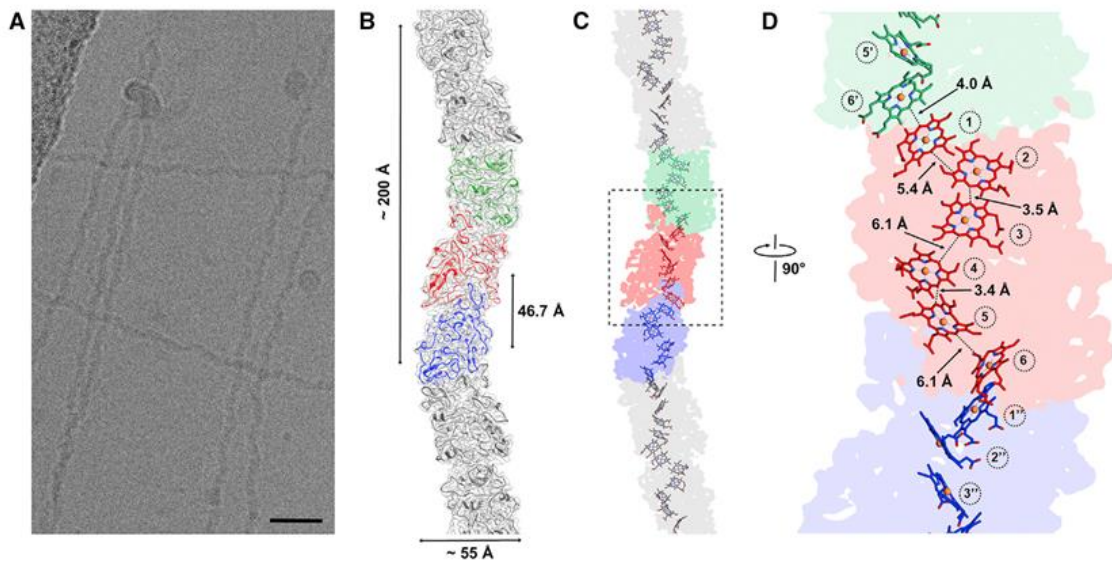


Figure 3.2 Structure of Microbial Nanowires Reveals Closely Stacked Hemes in an OmcS Filament.

(a) Cryo-EM image of the purified wild-type electrically-conductive filaments showing a sinusoidal undulation with a pitch of ~ 200 Å. Scale bar, 200 Å. (b) The surface of the reconstruction (transparent gray) with superimposed ribbon models of the OmcS subunits with three subunits in the center in three different colors. (c) Each subunit contains six hemes closely stacked over the micrometer-lengths of the filaments. (d) A zoomed region of the box shown in (c) with the minimum observed edge-to-edge distances indicated between hemes numbered in circles. The distance between two hemes in adjacent subunits (heme 1 and heme 6') is comparable to the distances between parallel stacked hemes within a subunit (heme 2:heme 3 and heme 4:heme 5).

Given that the protein contains at least 380 residues and would therefore have a likely molecular weight between 40 and 50 kDa, we used SDS-PAGE and cut out the strongest band in the gel, which was at ~45 kDa (**Figure 3.1a**), and analyzed this band by mass spectrometry. Five proteins were identified, four of which had heme-binding motifs (CXXCH) and had masses between 45 and 49 kDa (**Figure 3.1b**). Three of these proteins (OmcS, OmcT, and GSU2501) had a very similar pattern of heme-binding motifs that approximately matched the initial C_α trace (**Figure 3.3b**), and their sequences could be easily aligned (**Figure 3.3a**). These three proteins had between 45% and 63% sequence identity with each other. Another protein found in mass spectrometry, OmcZ (Inoue, Qian et al. 2010), contained ~30 additional residues compared to the other three, and thus its sequence could not be aligned to the others, and furthermore, the pattern of eight heme-binding motifs in OmcZ did not match that found in the map. The remaining protein, OmpJ, contains no heme (Afkar, Reguera et al. 2005). Of the three possible candidates, only the OmcS sequence could be threaded through the map without any conflicts (**Figure 3.3c,d**). There are nine regions of OmcT, GSU2501, or both that prevented their sequences from being fit into the map (**Figure 3.3a, highlighted in blue**). In addition, the pattern of bulky amino acids clearly established that only the OmcS sequence was consistent with the map. For example, the elongated density from arginine (R) 256 is clearly seen in the map (**Figure 3.3d**). But in the sequences of OmcT and GSU2501, this residue would be a valine (**Figure 3.3a, highlighted in purple**) that is not able to explain the map density. These studies show that the only cytochrome found in our filament preparations identified by mass spectrometry that is consistent with the cryo-EM map is OmcS.

While it has been known for more than half a century that cytochromes can polymerize in ethanolic solutions (Margoliash and Lustgarten 1962) and structures have been determined for aggregates of up to tetramers (Hirota, Hattori et al. 2010), natural polymerization of the type we observe here has not been previously described to my knowledge. Stacking arrangements of aromatic rings generally prefer parallel (offset face-to-face) or perpendicular (T-shaped) conformations (Janiak 2000). The parallel stacking yields the highest electronic coupling, which maximizes electron transfer (Jiang, Futera et al. 2017), whereas the T-shape enhances structural stability (Janiak 2000). Hemes in the OmcS nanowires form parallel-stacked pairs, with each pair perpendicular to the next, forming a continuous chain over the entire length of the filament (**Figure 3.2d**). The minimum edge-to-edge distances are 3.4–4.1 Å between the parallel hemes and 5.4–6.1 Å between the perpendicular stacked pairs (**Figure 3.2d**). For all hemes in OmcS nanowires, two histidine residues axially coordinate iron at the center of each heme, and the vinyl groups of each heme form covalent thioether bonds with cysteines (**Figure 3.4, below**). The bis-histidine axial ligation of the heme iron atoms is consistent with the coordination found in other multi-heme *c*-type cytochromes (Clarke, Edwards et al. 2011), and the cysteine linkages are consistent with the *c*-type hemes reported to occupy six heme-binding motifs of OmcS (Qian, Mester et al. 2011).

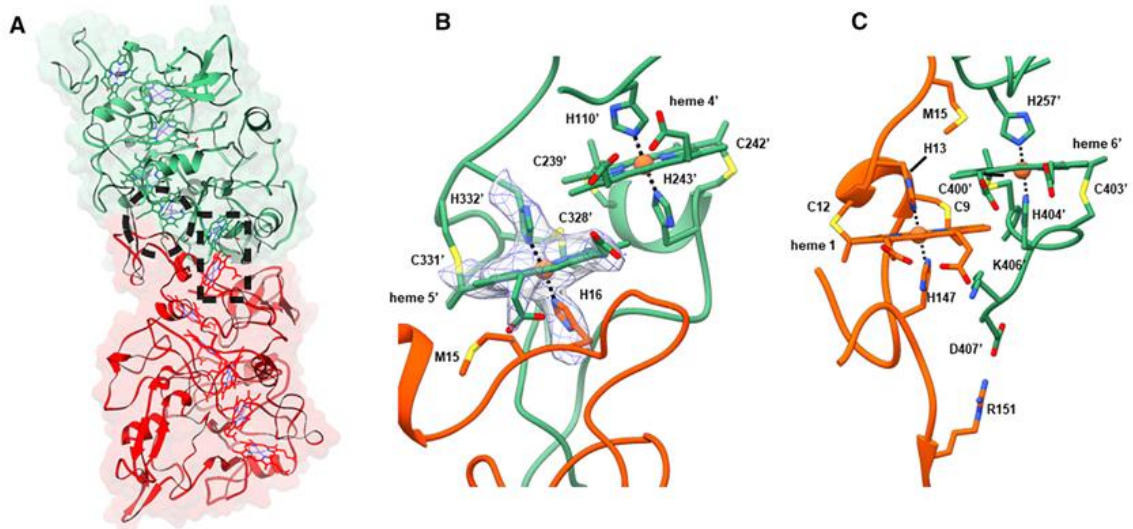


Figure 3.4 Subunit Interface Interactions within OmcS Filament

(a) The large interface in the filament ($\sim 2,600 \text{ \AA}^2$ per subunit) is due to the complementarity between the top of one subunit (green) and the bottom of an adjacent subunit (red). Residues in one subunit strongly interact via hemes shown in the dashed circle and rectangle (orange) and corresponding zoomed images in **b** and **c** respectively. (b) Histidine 16 of the bottom subunit is coordinating the iron atom in heme 5' of the top subunit. The cryo-EM densities corresponding to Histidine 16, Histidine 332', and heme 5' are shown in a mesh. (c) The stacking of heme 6' from a top subunit on heme 1 from the subunit below.

The OmcS filament model has a low percentage of α and 3_{10} helices (~13%) as well as β strands (~6%), leaving ~81% of the model as turns and coil, which is consistent with previous secondary-structure studies of OmcS (Qian, Mester et al. 2011). We compared the OmcS protomer within the filament with a group of three crystallographic structures of other multi-heme c-type cytochromes (PDB: 1OFW, 3UCP, and 3OV0). These structures showed 45%, 49%, and 60% turns and coils, respectively, with uniformly hydrophobic cores surrounding the hemes and heme-binding residues. Cores in our model of OmcS also included buried charges (arginine at locations 333, 344, and 375) that lack proximal compensating charges, as well as buried sidechain hydroxyls (tyrosine at locations 186, 231, and 385). In addition, our model of OmcS has a salt bridge between protein chains, aspartate 407 to arginine 151, which along with cysteines in heme binding motifs, are highly conserved amino acids in OmcS (Ashkenazy, Abadi et al. 2016). The lack of structural homology seen with these other c-type cytochromes is consistent with the observation that there is no conserved fold for this family of proteins (Bertini, Cavallaro et al. 2006).

The model shows that each OmcS subunit contacts only one subunit on either side, so that all connectivity in the filament is along the left-handed 1-start helix (**Figure 3.2b**). The interface between adjacent subunits is extensive, with ~2,600 Å² of surface area buried per subunit (**Figure 3.4a**). In addition to the buried surface area, interactions between adjacent subunits incorporate additional stabilizing elements unique to the filament structure. Histidine 16 in each subunit coordinates the iron in heme 5 of an adjacent subunit (**Figure 3.4b**). Furthermore, heme pairs at the interface are parallel rather than T-shaped, with ~4 Å edge-to-edge distance (**Figure 3.2d, Figure 3.4b,c**). This

parallel stacking and inter-subunit coordination of heme may contribute substantially to the stability of the protein-protein interface. In addition, the presence of parallel-stacked hemes at the interface suggests facile transport of electrons between monomers.

This finding that WT *G. sulfurreducens* nanowires are OmcS filaments is consistent with previous physiological studies. These studies highlight the importance of OmcS in extracellular electron transfer (Mehta, Coppi et al. 2005, Holmes, Chaudhuri et al. 2006, Leang, Qian et al. 2010, Summers, Fogarty et al. 2010, Leang, Malvankar et al. 2013). OmcS is one of the most abundant cytochromes found in the proteome for electricity-producing *G. sulfurreducens* and is required only during extracellular electron transfer to insoluble electron acceptors such as Fe(III) oxide (Mehta, Coppi et al. 2005, Holmes, Chaudhuri et al. 2006). It is also critical for direct interspecies electron transfer between syntrophic *Geobacter* co-cultures as evolved co-cultures overexpressed OmcS and deletion of the *omcS* gene inhibited bacterial ability to exchange electrons (Summers, Fogarty et al. 2010).

OmcS also plays a critical role in electron transport to electrodes in current-producing biofilms. Both microarray and quantitative reverse transcription polymerase chain reaction (qRT-PCR) analyses have demonstrated that cells show greatest increase in transcript levels for OmcS during the early stages of growth on electrodes (Holmes, Chaudhuri et al. 2006). Furthermore, immunogold localization has shown that OmcS is distributed throughout conductive *G. sulfurreducens* biofilms (Leang, Malvankar et al. 2013) and that deletion of the *omcS* gene inhibits their production of electricity under some conditions (Holmes, Chaudhuri et al. 2006). However, the role of OmcS in

conductivity of nanowires was overlooked because *ΔomcS* biofilms were conductive and produced high current densities (Malvankar, Vargas et al. 2011).

Using immunogold localization, previous studies found that OmcS is associated with filaments (Leang, Qian et al. 2010, Summers, Fogarty et al. 2010, Leang, Malvankar et al. 2013). As cytochromes were not known to form filaments before our work, AFM images of filaments (Malvankar, Tuominen et al. 2012) as well as these antibody-labeling results (Leang, Qian et al. 2010, Summers, Fogarty et al. 2010, Leang, Malvankar et al. 2013) were interpreted as showing isolated OmcS monomers binding to the surfaces of the PilA filaments rather than showing antibodies directly binding to OmcS filaments. Considering the result presented here, a reinterpretation of these previous studies suggests that the antibodies may have been directly binding to the subunits of the OmcS filaments.

In summary, these findings show that the conductive *G. sulfurreducens* filaments are polymerized chains of OmcS. The filament structure has hemes closely stacked along the micrometer length of the filament, establishing the molecular basis for electronic conductivity. The structure presented here provides insights into supramolecular protein nanowires, explaining the remarkable capacity of soil bacteria to transport electrons to extracellular electron acceptors for respiration (Malvankar, Vargas et al. 2011) and for sharing of energy and nutrients with syntrophic partners (Summers, Fogarty et al. 2010) that are hundreds of micrometers away. The advances in understanding of the structural basis for conductivity in microbial nanowires presented here can provide design principles for development of future bioelectronic interfaces between living cells and devices.

3.3.2 *G. sulfurreducens* uses OmcZ nanowires when grown in engineered biofilm environments where long-range electron transfer is required for survival

The discovery of the conductive OmcS nanowires answered many longstanding questions in the *Geobacter* field, but it also raised fresh queries. The presence of OmcS nanowires explains bacterial electron transfer to Fe(III) oxide, one of the most abundant minerals in natural soil and sediment environments (Mehta, Coppi et al. 2005), but in addition to this short-range (~1-2 μm) electron transfer *G. sulfurreducens* can also generate high current density by forming 100- μm -thick conductive biofilms on electrodes under the influence of an electric field in microbial fuel cells; importantly, *G. sulfurreducens* can form these highly-conductive and thick biofilms even in mutant strains where *omcS* is deleted (Inoue, Leang et al. 2010). Thus, the mechanism for this long-range (~100 μm) electron transport in current-producing biofilms grown under an electric field remained unknown. In addition to OmcS, we also identified a second, thinner filament in our preparations from current-producing biofilms (**Figure 3.5c**). Thus, I hypothesized that this second filament could be responsible for conferring the conductivity to current-producing biofilms when the OmcS gene is deleted and therefore sought to identify the protein that assembled into this filament. The averaged power spectrum from the cryo-EM projections of these filaments showed similar layer lines to the OmcS filament but with a slightly different axial rise of ~57 \AA and rotation of ~160°, suggesting that this thinner filament is also not a type IV pilus and could potentially be another cytochrome filament. Due to lower abundance of this filament in our cryo-EM images, it was not possible to build an atomic model in order to determine its composition.

Previous studies found that another *Geobacter* cytochrome, octaheme *c*-type cytochrome OmcZ, is not involved in electron transfer to Fe(III) oxides (Inoue, Qian et al. 2010) but is the only cytochrome that is essential for biofilms generating high current density in microbial fuel cells (Nevin, Kim et al. 2009). However, immunogold labeling did not show homogenous levels of OmcZ throughout these biofilms, but rather showed an accumulation of OmcZ near the electrode surface (Inoue, Leang et al. 2010). As the cytochromes were considered monomeric (Wang, Gu et al. 2019), previous studies (Nevin, Kim et al. 2009, Inoue, Leang et al. 2010, Malvankar, Tuominen et al. 2012) presumed that cells may use isolated OmcZ monomers for short-range electron transfer at the biofilm–electrode interface.

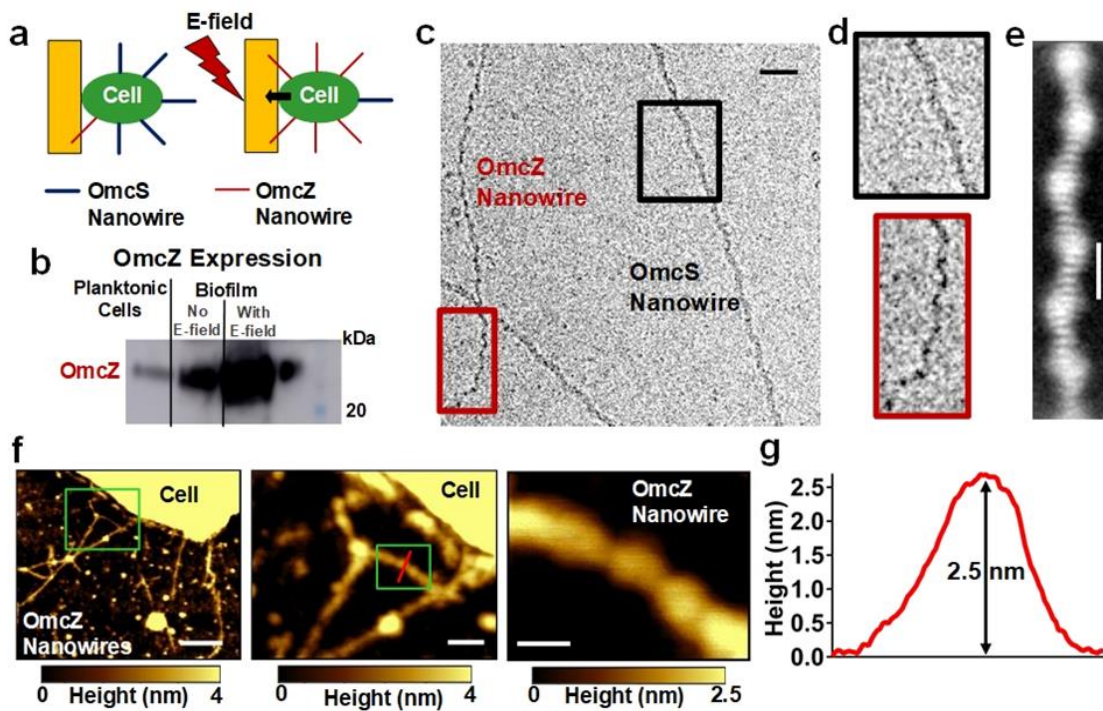


Figure 3.5 Electric Field Stimulates Production of OmcZ Filaments

(a) Schematics of microbial fuel cell for biofilm growth. Detailed setup is shown in **Figure 3.6a,b**. (b) Immunoblotting showing comparison of OmcZ abundance in filament preparations of WT cells under three different growth conditions. (c) Cryo-EM images of OmcS (black square) and OmcZ nanowires (red square). (d) Zoomed images of OmcS and OmcZ nanowires at locations show in c. (e) Cryo-EM projection (2D average) of OmcZ nanowire. (f) AFM image of WT bacterial cell grown under an electric field showing OmcZ nanowires with corresponding zoomed images of OmcZ nanowires at locations shown in green squares. Scale bars, **c**, 20 nm, **e**, 5 nm, **f**, 200 nm, 50 nm, and 20 nm.

To assess the effect of the electric field on the formation of OmcZ nanowires, we grew wild-type (WT) *G. sulfurreducens* on graphite anodes serving as an electron acceptor in a microbial fuel cell (O'Brien and Malvankar 2016), with a continuous supply of fumarate as an alternative, soluble electron acceptor (**Figure 3.5a and Figure 3.6a,b**). In one case, an electric field was supplied by connecting the anode to the cathode whereas in a control case, the anode was disconnected from the cathode to grow the biofilm at the open circuit potential in the absence of an external electric field. In comparison to planktonic cells, or biofilms grown in the absence of an electric field, biofilms grown in the presence of the electric field showed higher abundance of OmcZ in filament preparations as revealed by both peptide mass spectrometry and immunoblotting (**Figure 3.5b and Figure 3.6c-f**). Furthermore, cryo-EM showed the presence of ~2.5-nm diameter filaments in these samples in addition to the 3.5-nm-diameter OmcS nanowires (**Figure 3.5c,d**). Image analysis of these thinner filaments showed substantially different helical parameters (an axial rise of 57 Å and a rotation of 160°) compared to the OmcS nanowires (an axial rise of 46.7 Å and a rotation of -83.1°)(Wang, Gu et al. 2019). By analyzing these helical parameters we estimated a molecular weight of ~30 kDa for the protomer in these filaments (see Methods). This molecular weight is consistent with extracellular OmcZ, whereas intracellular OmcZ is 50 kDa (Inoue, Qian et al. 2010). These results show that the electric field applied to biofilms induces overexpression of OmcZ and suggests that the ~2.5-nm-diameter filaments observed in cryo-EM images could be made up of OmcZ.

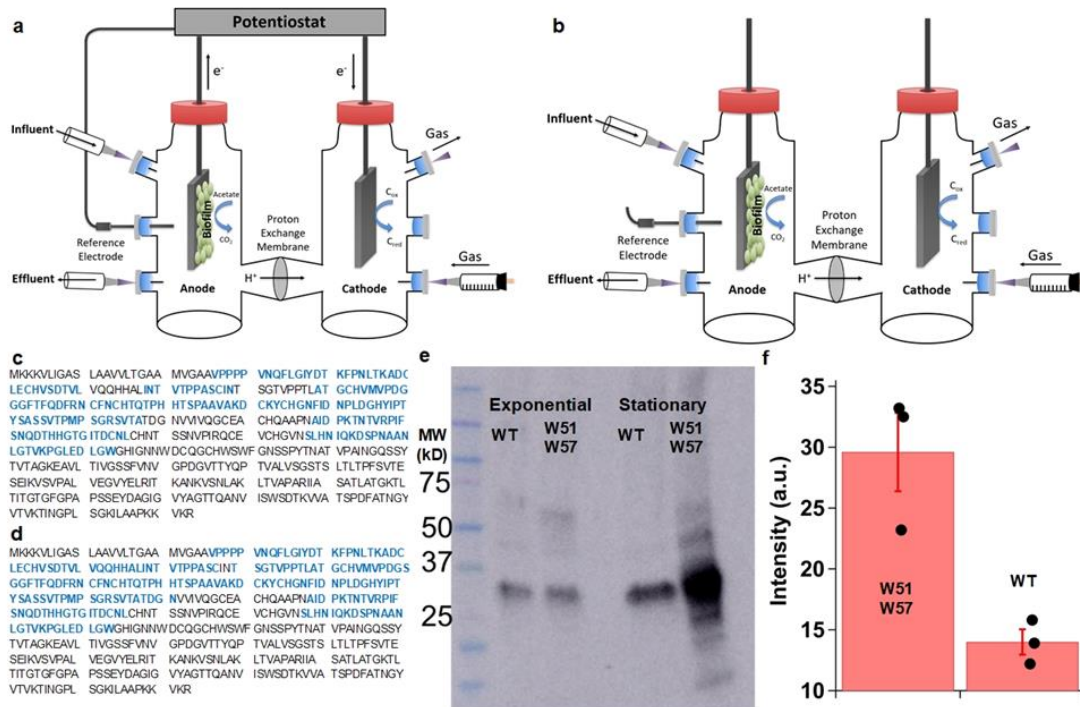


Figure 3.6 Mass Spectrometry and Immunoblotting of Filament Preparations Confirm Current-producing Biofilms Induce Overexpression of OmcZ. (a-b), Strategy to evaluate the effect of an electric field on OmcZ nanowire production. Wild-type *G. sulfurreducens* cells were grown with a continuous supply of fumarate on graphite electrodes as anodes in a microbial fuel cell. (a) An electric field was supplied during the growth of current-producing biofilms by connecting anode to cathode via a potentiostat. (b) The electric-field was absent after disconnecting the anodes from the cathodes. OmcZ peptide coverage (blue) in filament preparations of (c) Wild-type (WT) and (d) the W51W57 strain confirming the presence of an extracellular (30 kDa) form of OmcZ. Comparison of OmcZ abundance in filament preparations of WT and W51W57 strains using (e) immunoblotting and (f) mass spectrometry showing higher level of OmcZ in W51W57 strain than WT. Data represent mean \pm standard deviation (n= 3 biologically independent samples overlaid as black circles)

AFM images of WT cells grown under an electric field (**Figure 3.5f,g**), and a *ΔomcS* strain (**Figure 3.7**) grown under conditions that overexpress OmcZ (Inoue, Qian et al. 2010) showed filaments of ~2.5 nm in diameter on their surface with height and morphology similar to those of the cryo-EM images (**Figure 3.5c-e**). We further analyzed these 2.5-nm-diameter filaments from multiple strains by performing immunogold labeling with anti-OmcZ antibodies, using both AFM (**Figure 3.8a,b**) and negative-stain transmission electron microscopy (TEM) (**Figure 3.8c-f**). Only the 2.5 nm diameter filaments showed the labeling, whereas no labeling was found for filaments of the *ΔomcZ* strain or in the absence of the anti-OmcZ antibody (**Figure 3.8c,e**). These studies confirmed that the labeling was specific to the 2.5-nm-diameter filaments and revealed that these filaments were made of OmcZ.

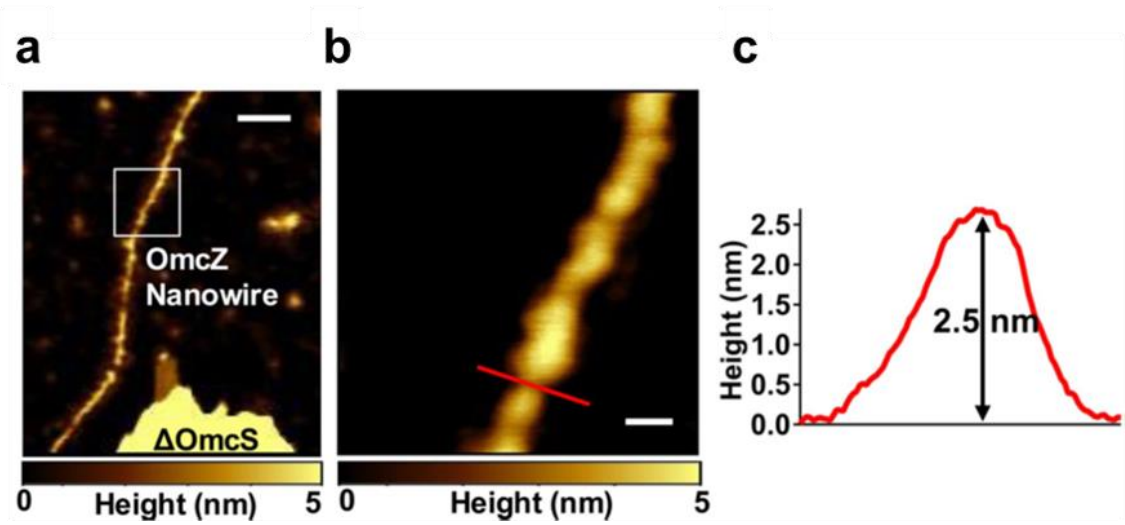


Figure 3.7 AFM Imaging of Nanowires produced by $\Delta omcS$ Strain

(a) AFM image of OmcZ nanowires produced by $\Delta omcS$ strain grown under conditions that overexpress OmcZ. (b) Zoomed image of OmcZ nanowire shown in white square in (a). (c) AFM height profile of the OmcZ nanowire taken at the location shown by a red line in (b). Scale bars: a, 100 nm c, 20 nm.

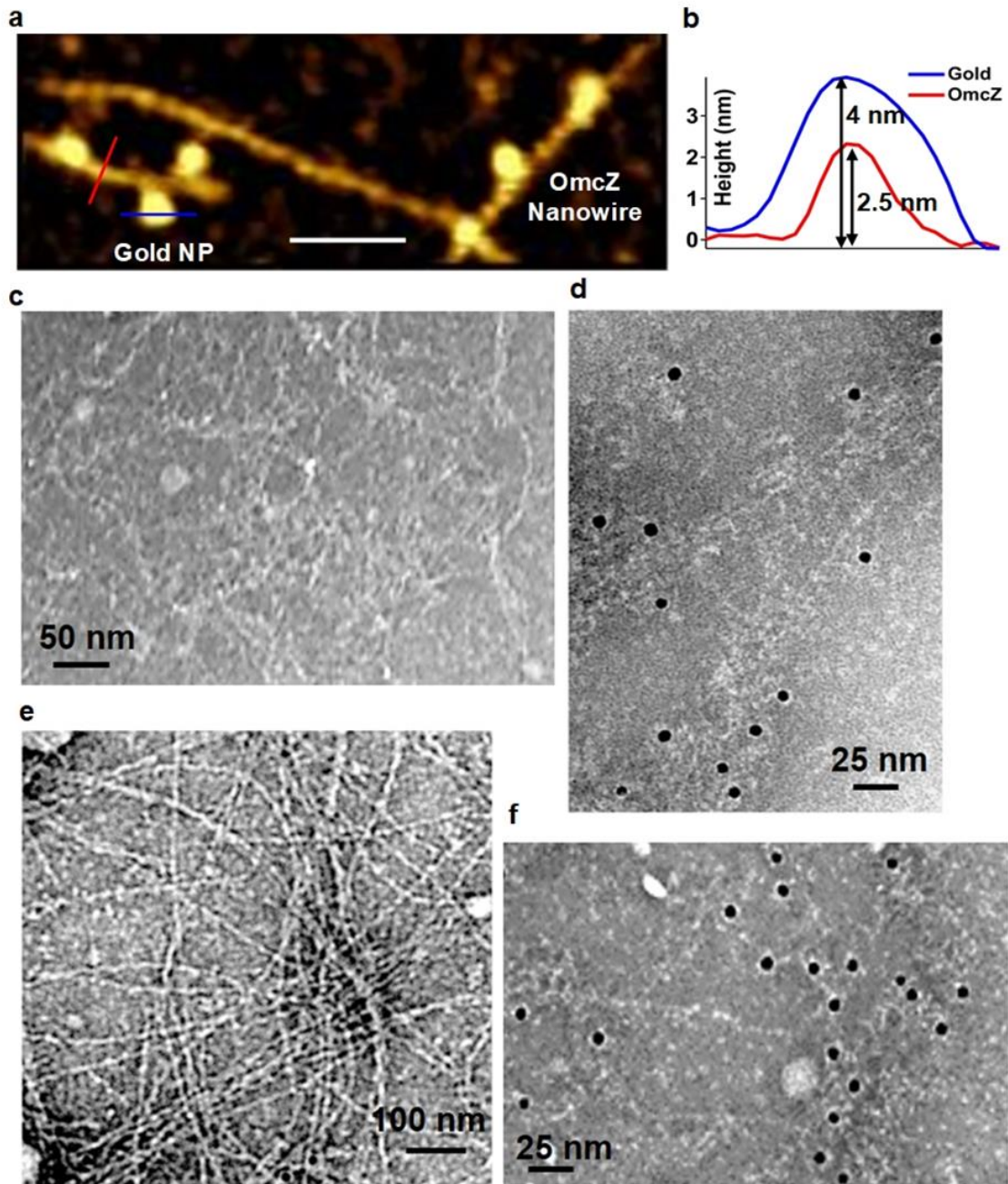


Figure 3.8 Immunogold Labelling Shows Presence of OmcZ Nanowires

(a) AFM image of immunogold-labelled OmcZ nanowire. (b) heights of nanowire (red) and gold nanoparticle (blue) at locations shown in a. (c-f) TEM images of OmcZ nanowires of ZKI strain in the (c) absence of OmcZ antibody and (d) in the presence of OmcZ antibody. Secondary antibody with gold nanoparticles was used in both c and d. (e) No OmcZ labelling was found for filaments of $\Delta omcZ$ strain (f) Labelling for OmcZ nanowires of W51W57 strain. Scale bars, a, 100 nm, c, 50 nm, d, 25 nm, e, 100 nm, f, 25 nm.

We also analyzed the 2.5-nm-diameter filaments of a ‘W51W57’ mutant *Geobacter sulfurreducens* strain where tryptophan (W) residues replaced a phenylalanine and tyrosine at locations 51 and 57, respectively, in the PilA protein (Tan, Adhikari et al. 2016). These filaments also showed labeling with anti-OmcZ antibodies, and immunoblotting and mass-spectrometry analysis of filament preparations revealed that the W51W57 strain produced more OmcZ than WT (**Figure 3.6c-f**). Our finding that the strain W51W57 produces more OmcZ is also consistent with previous studies (Richter, Sandler et al. 2012, Liu, Zhuo et al. 2018) that mutations in *pilA* affect the extracellular expression of both OmcS and OmcZ.

To further determine the composition of individual nanowires, we visualized their protein secondary structure by imaging the characteristic variations in the line shape of the IR-active amide I vibrational mode (primarily C=O stretch, 1,600–1,700 cm^{-1}) (Barth 2007). Using IR *s*-SNOM-based chemical imaging, we have directly visualized water molecules as they bind to individual minerals (Yalcin, Legg et al. 2020). IR *s*-SNOM provides quantitative information on the secondary structure for comparisons of proteins in various environments, although the measured amount of each secondary structure can differ from the amounts of secondary structure in cryo-EM structures or CD data analysis due to SNOM sensitivity toward C=O versus N–H stretch (Amenabar, Poly et al. 2013).

To evaluate the reliability and accuracy of our imaging platform for protein structure determination, we first performed IR *s*-SNOM imaging and spectroscopy of two proteins with well-known structures: bacteriorhodopsin (Amenabar, Poly et al. 2013, Berweger, Nguyen et al. 2013) and lysozyme (Barth 2007) as well as on individual OmcS

nanowires at pH 10.5 (conditions used to solve their atomic structure (Wang, Gu et al. 2019)), **Figure 3.9 and Figure 3.10**). As expected, the bacteriorhodopsin exhibited a purely α -helical spectra, indicated by a single peak at $1,663\text{ cm}^{-1}$ (**Figure 3.9e**) while lysozyme showed not only the α -helical peak but also two additional peaks at $1,618\text{ cm}^{-1}$ and $1,678\text{ cm}^{-1}$ indicative of β -sheets (Barth 2007) (**Figure 3.10a,b**). Notably, for lysozyme, the relative numbers of α -helices versus β -sheets measured by IR *s*-SNOM were comparable to those obtained by bulk FTIR and were in good agreement with literature values (Yang, Yang et al. 2015). At pH 10.5, the pH used to solve the cryo-EM structure of OmcS (Wang, Gu et al. 2019), the IR *s*-SNOM images and spectra of OmcS nanowires showed an α -helical component with the remainder being loop regions showing coils and turns (**Figure 3.10c,d**). These results were in agreement with the cryo-EM structure of OmcS (Protein Data Bank (PDB) ID 6EF8) that showed largely turns and coils with only 12% helices and 6% β strands. Together, these studies validated our nanoscale imaging approach for visualization and quantification of protein secondary structure.

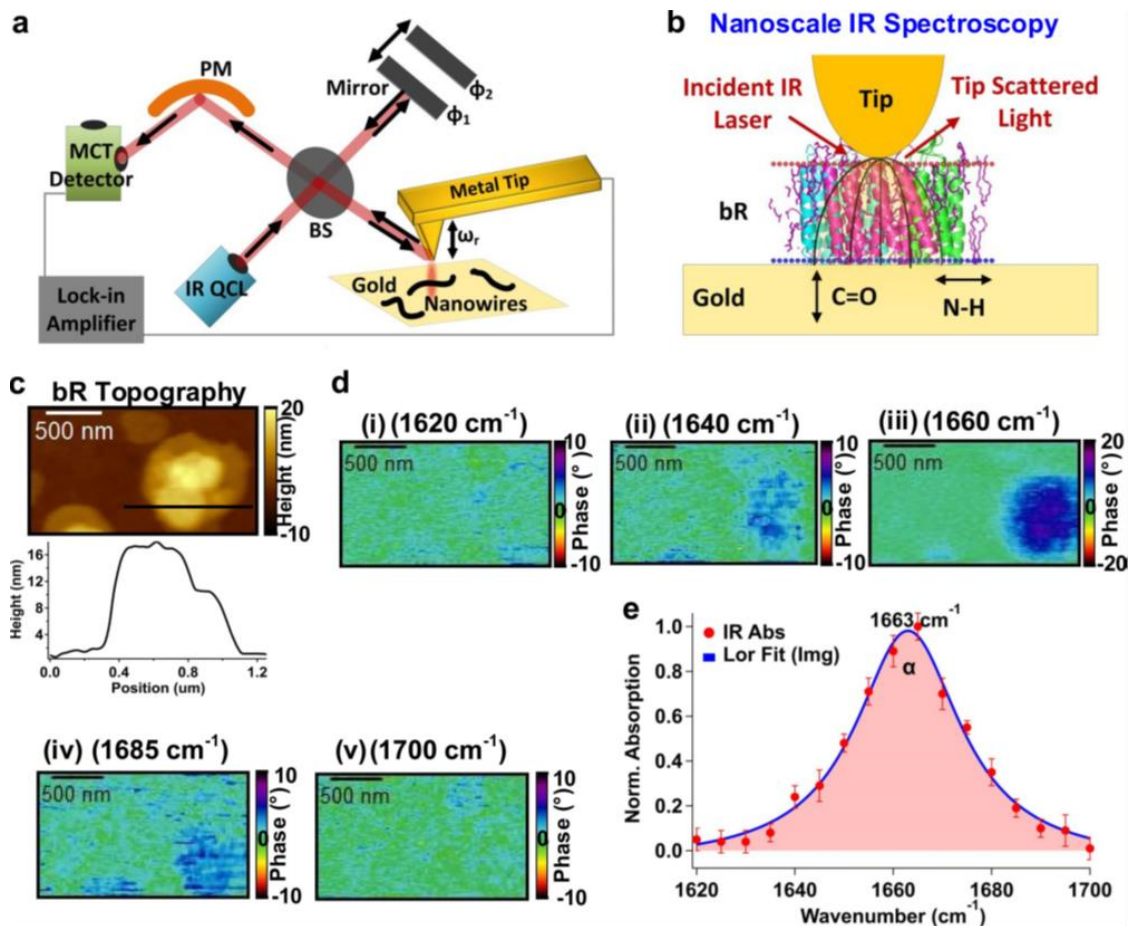


Figure 3.9 IR s-SNOM Imaging of Bacteriorhodopsin (bR) confirms α -helical Structure

(a, b) Schematic of IR s-SNOM. (a) The interferometer is comprised of a tunable quantum cascade laser (QCL) for tip illumination, a beam splitter (BS), a detector (Mercury Cadmium Telluride, MCT), a parabolic mirror (PM), and a reference mirror. (b) Schematic of the IR s-SNOM setup used for bR imaging (PDB ID: 1m0l). All helices are parallel to electric field lines that enhance the amide I signal. (c) AFM topography and corresponding height profile for bR taken at a location shown by a black line. (d) IR s-SNOM near-field phase (absorption) images for bR at various IR excitations. At 1660 cm^{-1} (iii, on-resonant IR), the amide I absorption is enhanced in the near-field phase data. However, when changed to other frequencies (i-ii & iv-v, off-resonance), the phase signal decreases and drops to zero. (e) Spatiospectral analysis of near-field amplitude and phase data for the amide I mode of bacteriorhodopsin. The blue line corresponds to a fit of the imaginary part of a Lorentzian (Lor) with peak at 1663 cm^{-1} and line width of 25 cm^{-1} . Data represent mean \pm standard deviation for individual bR proteins ($n = 3$ biologically independent samples).

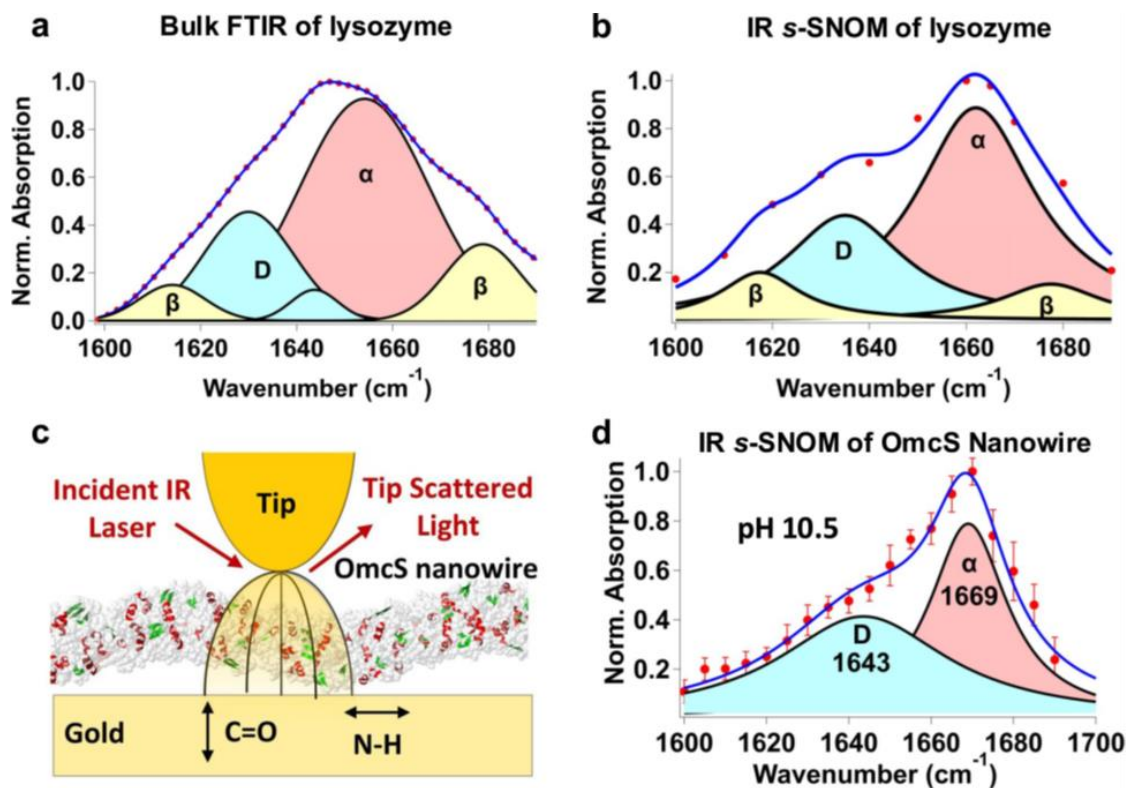


Figure 3.10 Bulk FTIR and IR s-SNOM Confirm Lysozyme Structure and IR s-SNOM Spectroscopy of OmcS Nanowires Agrees with Cryo-EM Structure
 Multi-peak fitting function was used to fit the data using (a) Gaussian profile for bulk FTIR and (b) a Lorentzian profile for IR s-SNOM data. α -helix corresponds to 1662 cm^{-1} , β -sheet corresponds to 1618 cm^{-1} and 1678 cm^{-1} , and the loop (D) region corresponds to 1635 cm^{-1} . (c) Schematic of the IR s-SNOM setup for nanowire imaging. Secondary structure of the OmcS nanowire at pH 10.5 is shown in (a) (PDB ID: 6EF8) with α -helices in red, 3_{10} helices in pink and beta strands in green. (d) At pH 10.5 used to solve the structure of OmcS nanowires, spatiospectral analysis of near-field phase data of the amide I mode of OmcS nanowire. The blue line corresponds to a fit of imaginary parts of a Lorentzian, with peak positions at 1669 cm^{-1} and 1643 cm^{-1} corresponding to α -helical and loop regions respectively. Data represent mean \pm standard deviation for individual OmcS nanowires ($n = 3$ biologically independent samples).

At pH 7, by IR *s*-SNOM, OmcS nanowires exhibited an α -helical component and coil/turns (**Figure 3.11a,b**), in agreement with previous studies of the secondary structure of purified OmcS monomers (Qian, Mester et al. 2011). In contrast, the OmcZ nanowires showed a substantial number of β -sheets and little coils/turns (**Figure 3.11c**), consistent with previous secondary structure studies of purified OmcZ monomers (Inoue, Qian et al. 2010).

Taken together, the IR *s*-SNOM studies, combined with cryo-EM, mass spectrometry, immunoblotting and immunogold labeling show that the electric field applied to *Geobacter sulfurreducens* biofilms stimulates the production of OmcZ nanowires. As the electric field is strongest near the electrode interface and decreases away from the electrode, OmcZ expression is expected to be at a maximum at the biofilm–electrode interface. This could explain previous experiments that found that cells show maximum accumulation of OmcZ (Inoue, Leang et al. 2010) and highest metabolic activity (Chadwick, Jimenez Otero et al. 2019) near the biofilm–electrode interface.

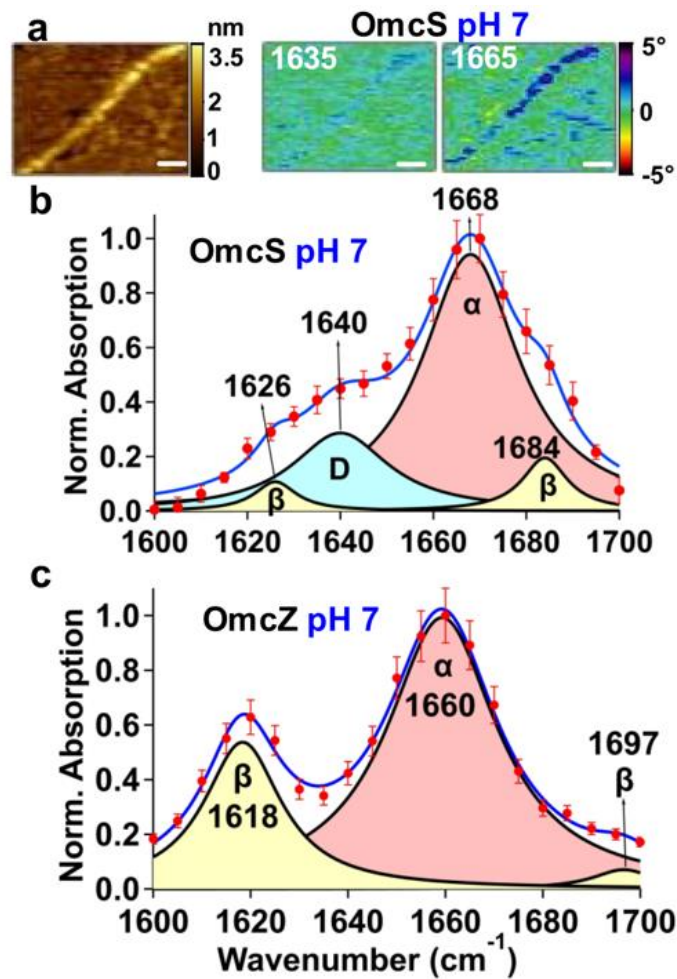


Figure 3.11 IR Nanospectroscopy Confirms OmcZ Nanowires in Biofilms Grown Under Electric Field

(a) Representative AFM height and corresponding IR s-SNOM images with laser excitation at 1,635 and 1,665 cm⁻¹ for OmcS nanowires at pH 7. Scale bar, 1 0.5 μm. (b, c) IR nanospectroscopy of amide I at pH 7 for OmcS nanowires (b) and OmcZ nanowires (c). Blue curves, amide I band-decomposition fits to the data (red markers). α, α-helices; β, β-sheets; D, loop regions showing coils and/or turns. For b, c, data represent mean ± s.d. for individual nanowires (n = 3 biologically independent samples).

3.3.3 The OmcZ nanowires are 1,000-fold more conductive than OmcS nanowires

We compared the conductivity of OmcS and OmcZ nanowires using a conducting-probe AFM approach. To determine the electronic conductivity along individual nanowires, we placed nanowires across a gold–silicon dioxide (SiO₂) interface with the AFM tip being held in contact with an isolated nanowire at various distances away from the gold electrode (**Figure 3.12a**). The current along the nanowire was measured as a function of the DC bias applied between the tip and the gold electrode as a function of nanowire length to determine the contact-free, intrinsic electrical resistance and hence conductance (**Figure 3.12b**). Control measurements by touching the tip directly to gold or insulating SiO₂ surface yielded expected results, demonstrating the validity of our approach. The resistance of OmcZ nanowires increased linearly with nanowire length, indicative of a wire-like behavior (Ho Choi, Kim et al. 2008) (**Figure 3.12c**). The OmcZ nanowires showed 1,000-fold higher conductivity than OmcS at pH 7 (**Figure 3.12d**), which could explain the ability of cells to transport electrons over 100 μm in biofilms (Malvankar, Vargas et al. 2011).

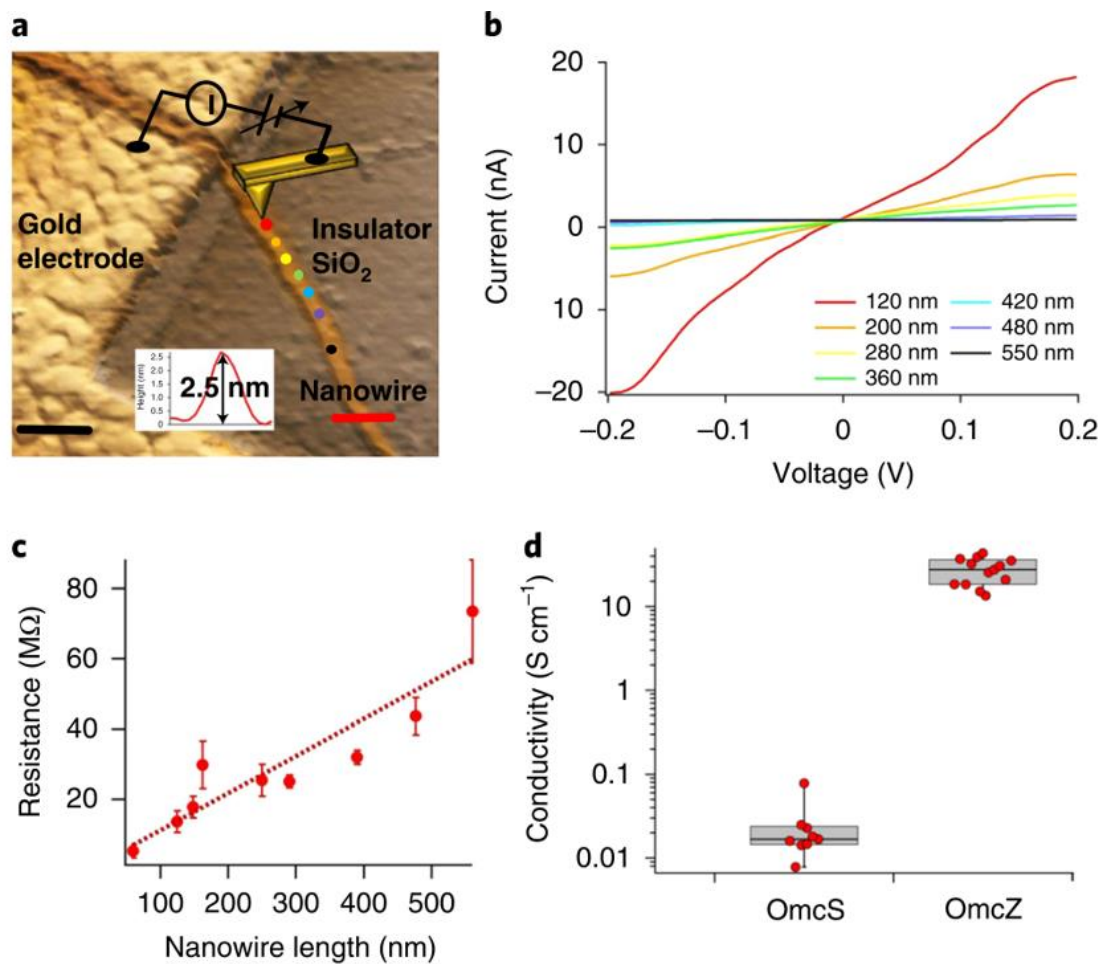


Figure 3.12 OmcZ nanowires show 1,000-fold higher conductivity than OmcS
(a) Schematic of CP-AFM with AFM topography image of OmcZ nanowire across the gold-SiO₂ interface. Scale bar, 100 nm. Inset, height profile of the nanowire at the red line. **(b)** Representative current-voltage (I-V) curves measured at locations on OmcZ nanowire shown in **a**. **(c)** Resistance of OmcZ nanowire as a function of distance away from gold electrode. Dotted line is a linear fit. Data represent mean \pm s.d. ($n = 8$ measurements for each nanowire length over three biologically independent samples). **(d)** Comparison of conductivity of OmcZ versus OmcS nanowires measured using CP-AFM at pH 7. Data represented as a box plot (biologically independent nanowires, $n = 13$ for OmcZ and $n = 9$ for OmcS). The box for the plot was defined as 25 and 75% with center line as median and the whiskers as 10 and 90%.

Grazing-incidence micro-XRD (GI μ XRD) patterns of OmcZ nanowires showed a more intense peak than OmcS nanowires with d spacing of 3.6 Å (**Figure 3.13a,b**). This d spacing likely corresponds to the face-to-face π -stacking distance between parallel-stacked hemes, as suggested by the structure of OmcS nanowires (**Figure 3.13a, inset**) (Wang, Gu et al. 2019). Improved π -stacking increases the effective conjugation length, yielding a longer mean free path for electrons that enhances conductivity (Lee, Cho et al. 2006). Therefore, our structural analysis indicated that the enhanced conductivity of OmcZ nanowires results from increased crystallinity and reduced disorder within the nanowires (**Figure 3.13b**).

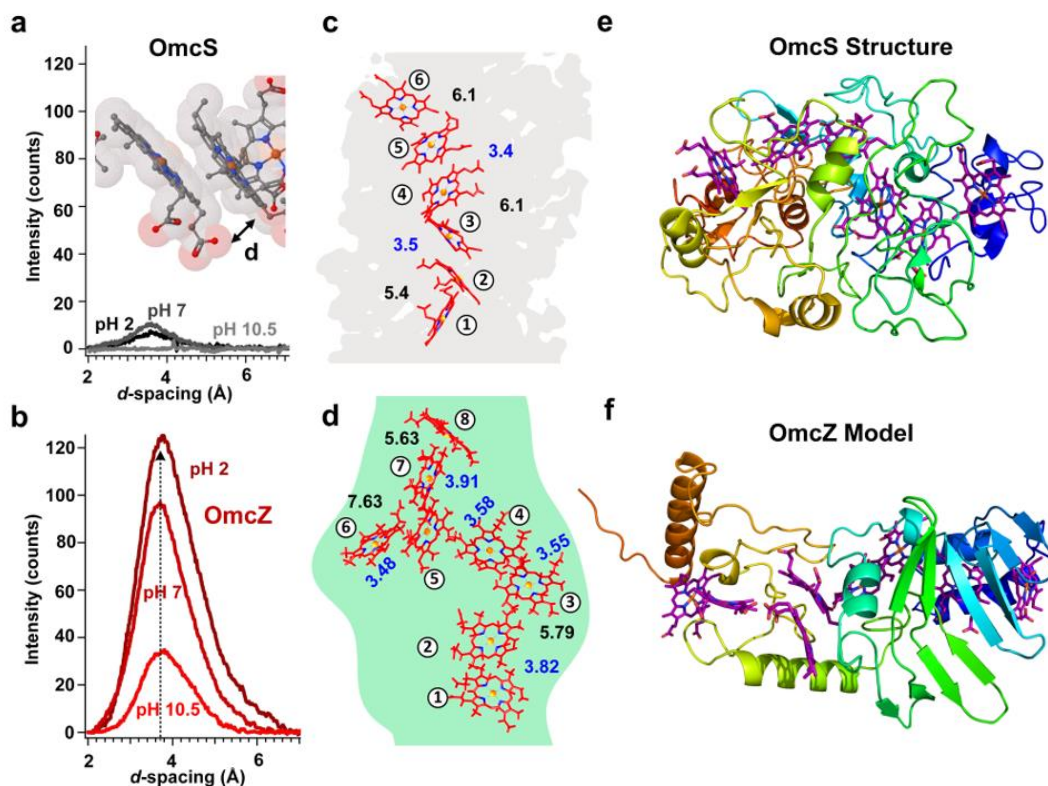


Figure 3.13 OmcZ Nanowires Show Improved π -stacking between Hemes Versus OmcS and Protonation Enhances π -stacking

(a, b) GI μ XRD of OmcS nanowire-containing (a) and OmcZ nanowire-containing (b) samples revealed increased intensity for a peak at a d spacing of 3.6 Å (pH 10.5 \rightarrow pH 2) suggesting improved π -stacking between hemes that correlated with enhanced conductivity. All measurements were repeated multiple times and yielded similar results. Inset for a, cryo-EM structure of OmcS nanowire with hemes as stick models colored by chemical elements (gray carbon, blue nitrogen, red oxygen, orange iron), with van der Waals radii translucent. (c, d) Arrangement of hemes (red) in OmcS (c) and eight-heme proteins (d). Cryo-EM density is in gray and green for OmcS and OmcZ, respectively. Edge-to-edge distances in Å between heme pairs in OmcS and eight-heme proteins are in blue. (e) Cryo-EM structure of OmcS. (f) Computational model of OmcZ monomer. Structures in e and f are colored by residue number, blue (N terminus) to red (C terminus).

We built a computational model of the OmcZ structure to understand the molecular mechanism underlying the increased stacking of hemes in OmcZ as compared to OmcS (**Figure 3.13**). Based on the finding that many heme proteins show similar stacking arrangements of hemes (Valasatava, Andreini et al. 2015), we used this arrangement of eight hemes as a template for the OmcZ model, which agreed well with the cryo-EM density map for OmcZ nanowires (**Figure 3.13d**). These eight-heme protein structures revealed a dense packing and a substantially different arrangement of hemes when compared to OmcS nanowires (**Figure 3.13c**). This dense packing of hemes is consistent with eight hemes packed in the 30-kDa OmcZ protomer versus six hemes packed in the 45-kDa OmcS protomer. Comparison of edge-to-edge heme–heme distances showed that OmcS has only two heme pairs within π -stacking distance (3.5–4 Å) (Janiak 2000) whereas the eight-heme protein structures showed five heme pairs within π -stacking distance (**Figure 3.13c,d**). These eight-heme protein structures are thus consistent with the XRD data and further indicate that the increased conductivity of OmcZ nanowires is due to a more compact molecular structure with a higher density of heme groups compared to the OmcS nanowires. The polymerization of the OmcZ monomers could further reduce the distance between hemes for closer stacking of hemes in OmcZ nanowires than that found in the OmcS nanowires. In contrast to the OmcS nanowire structure, the OmcZ model showed a β -sheet-rich structure (**Figure 3.13e,f**), in agreement with IR s-SNOM studies (**Figure 3.11**). To further evaluate the validity of the OmcZ model, we compared the heme ligation by two consecutive histidines in OmcZ to three different structures of cytochrome c_3 (PDB 1GYO, 2BQ4 and 2E84). The amino acid sequence of c_3 contains a CXXCHH motif with one proximal and one distal histidine

in the heme pairs, while OmcZ contains two distal histidines. All four structures showed consecutive histidines causing tight heme T junctions with similar heme–heme distances.

These results propose several testable hypotheses for future work to determine the difference in conductivity between the OmcS and OmcZ nanowires, which might provide further design principles for designing nanowires with even greater conductivity.

3.4 Discussion: revisiting the role of PilA

The discovery of the OmcS and OmcZ nanowires at first seems contradictory to over a decade's worth of work in the *Geobacter* field, which all pointed to PilA forming the conductive nanowires. However, while PilA's role was misunderstood its importance was certainly not overstated. While no evidence of PilA was found in the structure of any of the purified filaments, non-filamentous PilA was present in our samples in low abundance, consistent with prior studies (Tan, Adhikari et al. 2016). Multiple studies have shown that PilA is required for secretion of OmcS and OmcZ to the extracellular environment, as pilA deletion eliminated the presence of OmcS in outer-surface preparations (Richter, Sandler et al. 2012, Liu, Zhuo et al. 2018). Overexpression of PilA is also accompanied by overproduction of OmcS, OmcZ and filaments (Summers, Fogarty et al. 2010, Leang, Malvankar et al. 2013), further suggesting that PilA is involved in secretion of OmcS filaments that may explain previous correlations found between PilA and biofilm conductivity (Malvankar, Vargas et al. 2011). The requirement of PilA for the synthesis of OmcS and OmcZ filaments thus also explains the inability of *ΔpilA* cells to grow on insoluble electron acceptors such as Fe(III) oxides (Reguera, McCarthy et al. 2005) and electrodes (Reguera, Nevin et al. 2006). A number of other bacteria have also been shown to require non-filamentous type IV pilins for the secretion

of extracellular proteins (Hager, Bolton et al. 2006). One possibility is that PilA is acting as a pseudopilin as a part of a type 2 secretion system (T2SS) (Nivaskumar and Francetic 2014) and that OmcS and OmcZ are exported by this T2SS. Previous studies have shown that T2SS pseudopili can be secreted outside the cell (Vignon, Kohler et al. 2003, Nivaskumar and Francetic 2014). A similar mechanism could explain the presence of non-filamentous PilA in our crude filament preparations.

This potential ability of PilA to regulate the secretion and assembly of the OmcS and OmcZ nanowires (Richter, Sandler et al. 2012, Liu, Zhuo et al. 2018) could explain how point mutations in *pilA* caused *Geobacter* cells to produce filaments with different conductivities than WT filaments. Filaments produced by cells with point mutations in *pilA* showed very different morphology than WT filaments (Tan, Adhikari et al. 2016). For example, substitution of two residues in PilA with tryptophan yielded mutant cells with filaments that surprisingly had half the diameter of WT filaments (Tan, Adhikari et al. 2016). Elucidating the true role of PilA is a vital next step for the *Geobacter* field and will be essential for determining how to express these conductive nanowires in other bacteria.

4 Determining the mechanism of pH-induced increase in nanowire conductivity

4.1 Author Contributions

Portions of this chapter have adapted from previously published works:

O'Brien, J.P.*, Yalcin, S.E.*, Gu, Y., Reiss, K., Yi, S.M., Jain, R., Srikanth, V., Dahl, P.J., Huynh, W., Vu, D., Acharya, A., Chaudhuri, S., Varga, T., Batista, V.S., and Malvankar, S.M., (2020) Electric Field Stimulates Production of Highly Conductive Microbial OmcZ Nanowires *Nature Chemical Biology* **16** 1136-1142

Yi, S.M., Guberman-Pfeffer, M.*, **O'Brien, J.P.***, Dahl, P.J., Frenkel, A.I., Yalcin, S.E., Batista, V.S., Brudvig, G.W., and Malvankar, N.S. (Submitted) Hundred-fold Conductivity Increase in Microbial Nanowires Due to pH-driven Conformational Change Causing J-aggregate-like haem stacking

I grew the *Geobacter* cultures and purified the filaments used for all studies in this chapter. Sibel Yalcin built the IR *s*-SNOM setup, collected the data, and completed the analysis along with Winston Huynh. I completed the bulk CD, FTIR, UV-vis, THT fluorescence and THT fluorescence microscopy experiments. Sophia Yi collected and analyzed the Raman spectroscopy data. I worked with Sibel Yalcin and Winston Huynh to compare the secondary structure components from nano-FTIR, CD, bulk FTIR, and Raman experiments. Stiffness measurements were completed by Yangqi Gu and Sophia Yi. Matthew Guberman-Pfeffer completed the computational studies on excitonic

coupling and UV-vis spectral shifts to compare with my UV-vis data under the guidance of Victor Batista. Sophia Yi collected the EPR data under the guidance of Gary Brudvig. Anatoly Frenkel completed the XAF experiments and helped with data analysis.

4.2 Introduction

Previous work has found that the conductivity of *G. sulfurreducens* nanowires increases at lower pH (Malvankar, Vargas et al. 2011, Malvankar, Vargas et al. 2015, Adhikari, Malvankar et al. 2016, Tan, Adhikari et al. 2016), but the underlying mechanism behind this increase has remained unknown (Malvankar, Vargas et al. 2015). Herein, I examine the role of protein and electronic structure in conferring this increase in nanowire performance.

To determine the composition, structure, electrical and mechanical properties of individual OmcS and OmcZ nanowires, purified from wild-type and W51W57 cells, respectively, I worked with a post-doctoral researcher in our group to combine four complementary nanoscopic tools in a multimodal imaging platform: **(1)** high-resolution atomic force microscopy (AFM) to identify protein composition and morphology; **(2)** infrared (IR) nanospectroscopy using scattering-type scanning near-field optical microscopy (*s*-SNOM) (Amenabar, Poly et al. 2013) to identify biomolecules through their characteristic IR vibrational signatures; **(3)** conducting-probe-AFM (CP-AFM) to measure electron transport along the nanowire length and **(4)** nanomechanical AFM to determine nanowire stiffness. To further investigate the structural features in nanowires that enhance conductivity, we complemented these nanoscale studies with protein modeling and molecular dynamics simulations, cryo-electron microscopy (cryo-EM), as

well as bulk measurements using X-ray diffraction, Fourier-transform IR spectroscopy (FTIR), circular dichroism (CD), Raman and fluorescence spectroscopy.

4.3 Results

4.3.1 Lowering pH induces an increase in conductivity, shrinking of diameter, and increase in stiffness for both OmcS and OmcZ nanowires

Here, I found evidence of pH-induced structural changes that correlate with the increased conductivity. AFM imaging revealed that the nanowire diameter decreased from 3.6 nm to 2.4 nm for OmcS and from 2.5 to 1.5 nm for OmcZ (**Figure 4.1a**). This reduction in nanowire diameter upon lowering the pH helps to explain the increased π -stacking of hemes (**Figure 3.13a,b**). Thus, OmcS and OmcZ nanowires undergo very large conformational changes (due to the decrease in diameter by 12 Å and 10 Å, respectively) that significantly enhance the conductivity (by 10- and 100-fold respectively, **Figure 4.1b**) and the stiffness (by 2.5- and 1.5-fold respectively, **Figure 4.1a**). Conformational changes that affected conductivity in other synthetic molecules were previously found to remain local and < 2 Å, thus yielding at most a tenfold change in conductivity (Donhauser, Mantooth et al. 2001, Su, Li et al. 2015, Li, Wang et al. 2017). In contrast, OmcZ nanowires show a 10 Å conformational change and 100-fold increase in conductivity. We anticipate that such large-scale conformational changes, responsible for stereoelectronic effects, could find applications such as switches in memory and logic devices (Donhauser, Mantooth et al. 2001, Su, Li et al. 2015, Li, Wang et al. 2017).

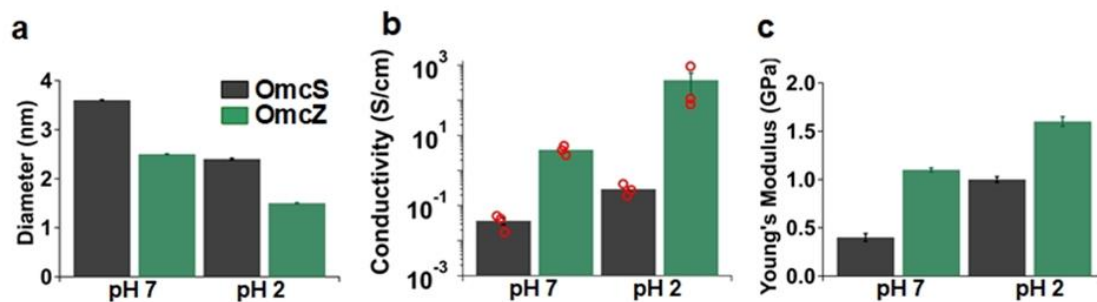


Figure 4.1 The OmcS and OmcZ nanowires show reduction in diameter, increase in conductivity, and increase in stiffness as pH is lowered
(a) Relative heights and pH-induced reduction in nanowire diameter, **(b)** height-corrected electronic conductivity, and **(c)** stiffness of OmcS and OmcZ nanowires. Data represent mean \pm standard deviation (s. d.), $n = 100$ nanowire measurements over three biological replicates for **a** and **c** and mean \pm standard error of the mean (s. e. m.), $n = 3$ biological replicates for **b** overlaid as red circles.

4.3.2 Spectroscopic insights into pH induced changes in OmcS and OmcZ protein structure

To further delineate the mechanism underlying the pH-induced conformational changes, we located nanowires via AFM and compared their corresponding IR *s*-SNOM images at pH 7 and pH 2 (**Figure 4.2**). IR *s*-SNOM of the OmcS nanowires at pH 7 showed prominent absorption at 1665 cm^{-1} , corresponding to α -helices (**Figure 4.2a**). The analysis of the amide I band showed 70% α -helical, 10% β -sheet, and 20% coil/turn (**Table 1**). Upon lowering the pH to 2, the absorption at 1625 cm^{-1} , which is assigned to β -sheets (Barth 2007), increased 7-fold (**Figure 4.2b**). Further, the peak at 1640 cm^{-1} corresponding to coil/turn loops disappeared along with a 3-fold decrease in the α -helix peak. Therefore, much of the α -helical and coil/turn structures in the OmcS nanowires converted to β -sheets at low pH. Consequently, the stiffness of OmcS nanowires increased 2.5-fold to 1 GPa at pH 2, likely due to an increased number of intermolecular hydrogen bonds in the newly formed β -sheets (**Figure 4.1c, above**) (Simone, Jozef et al. 2015). Furthermore, the conductivity increased 10-fold to 0.3 S/cm at pH 2 (**Figure 4.1b**). Therefore, the increase in β -sheet structure can account for the reduction in diameter of OmcS nanowires at pH 2 and their increased conductivity as well as stiffness.

Table 1: Composition of the secondary structure of OmcS (WT) and OmcZ (W51W57) nanowires at pH 7 and pH 2 from IR *s*-SNOM measurements

Secondary Structure	OmcS pH 7 (%)	OmcS pH 2 (%)
Alpha-Helix	69.1	26.3
Beta-Sheet	10.1	73.7
Loop	20.8	—
Secondary Structure	OmcZ pH 7 (%)	OmcZ pH 2 (%)
Alpha-Helix	70.4	29.2
Beta-Sheet	29.6	70.8
Loop	—	—

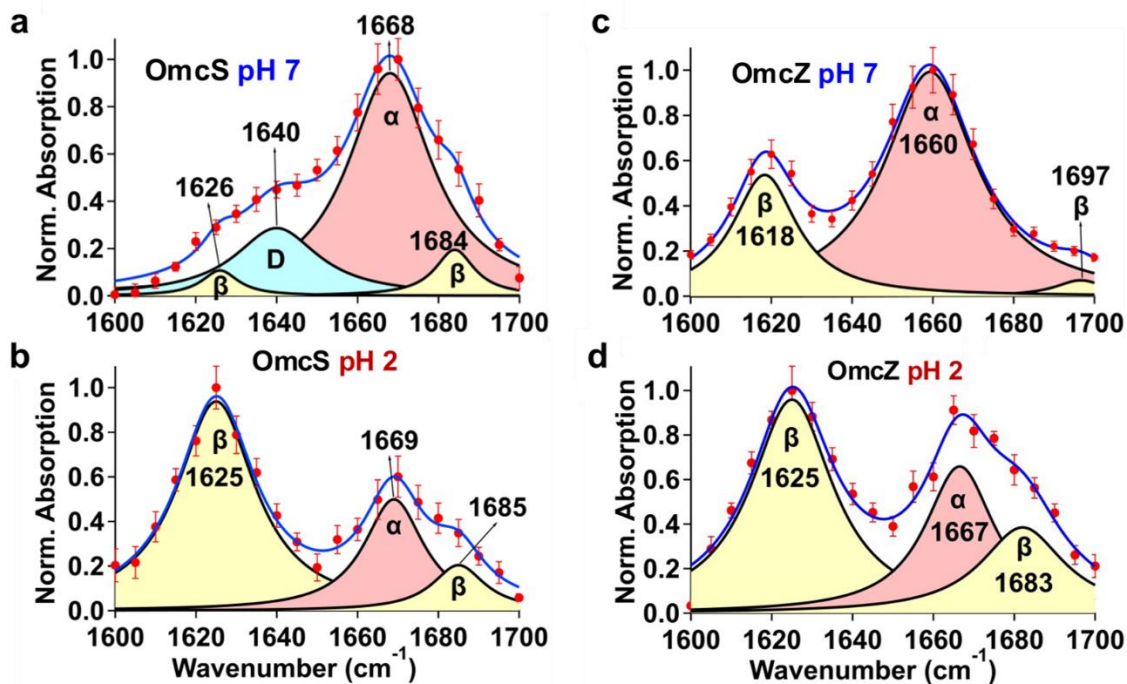


Figure 4.2 Nanoscale IR Spectroscopy Establishes pH-induced Structural Transition in OmcS and OmcZ Nanowires

(a, b) IR nanospectroscopy of OmcS nanowires at (a) pH 7 and (b) pH 2. (c, d) IR nanospectroscopy of OmcZ nanowires at (c) pH 7 and (d) pH 2. Blue curves, amid I band-decomposition fits to the data (red markers). α , α -helices; β , β -sheets; \mathbf{d} , loop regions showing coil/turns. Data represent mean \pm s.d. for individual nanowires ($n = 3$ biologically independent samples).

Upon lowering the pH from 7 to 2, the OmcZ nanowires exhibited a net 10,000-fold higher conductivity (400 S/cm) and 4-fold higher stiffness (1.6 GPa) when compared to OmcS nanowires at pH 7. IR *s*-SNOM revealed that at pH 7, OmcZ nanowires displayed a 7-fold increase in β -sheets over OmcS nanowires (**Figure 4.2a,c**). At pH 2, the β -sheet content in OmcZ nanowires further increased 3-fold compared to pH 7 (**Figure 4.2d**). These results suggest that OmcZ nanowires have highly ordered β -sheets that enhance their conductivity and stiffness as well as confer a more compact structure than the OmcS nanowires.

AFM and IR *s*-SNOM measurements were performed under ambient conditions (Freund, Halbritter et al. 1999) to maintain the native protein conformation. The measured heights of OmcS and OmcZ nanowires using AFM are consistent with those obtained from cryo-EM, validating the comparative analysis.

To further quantify the conformational changes, we used four additional and complementary methods: FTIR, Raman, fluorescence emission spectroscopy and circular dichroism (CD) (**Figure 4.3**). FTIR revealed formation of β -sheets induced upon lowering the pH for both OmcS and OmcZ nanowires as evidenced by a red shift in the amide-I peak (**Figure 4.4a-c**). However, the frequency shift was lower than that probed by IR *s*-SNOM, due to the diffraction-limited resolution of bulk FTIR (Barth 2007, Amenabar, Poly et al. 2013).

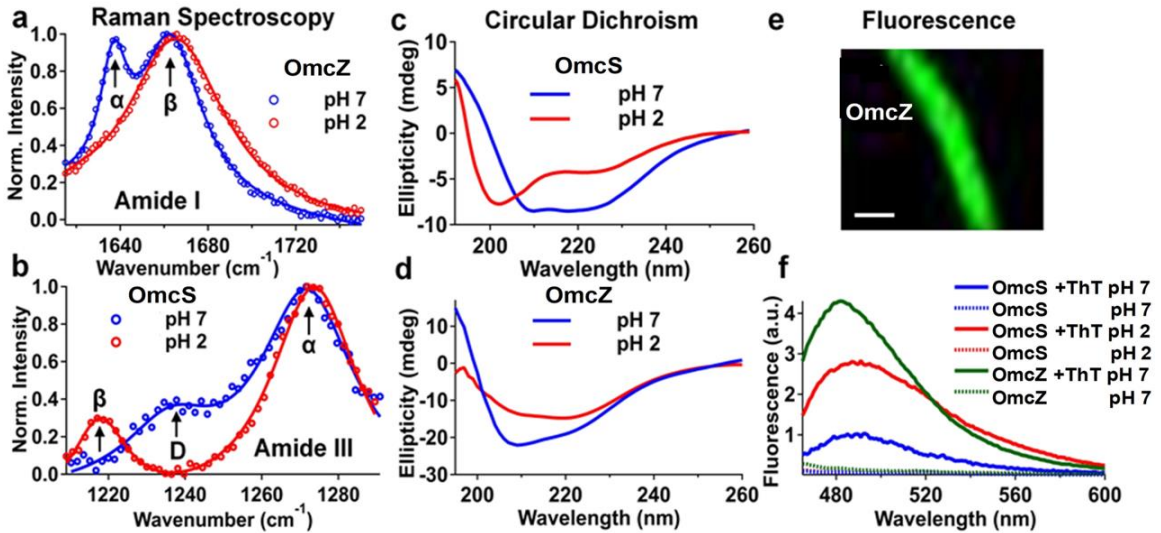


Figure 4.3 Raman, CD, and Fluorescence Spectroscopy Further Demonstrates pH-induced Structural Transition in OmcS and OmcZ Nanowire Containing WT and W51W57 Samples, Respectively

Raman spectra at pH 7 and pH 2 for (a) OmcZ nanowires (amide I) and (b) OmcS nanowires (amide III) showing transition to β sheets. (c) CD spectra of OmcS indicating that the predominantly α -helical structure at pH 7 (blue curve) transforms into β -sheets at pH 2 (red curve). (d) CD spectra of OmcZ reveal a β -sheet at both pH 7 and pH 2. (e) Fluorescence microscopy of thioflavin T (ThT)-stained OmcZ nanowires at pH 7. Scale bar: 500 nm. (f) Fluorescence emission of OmcZ increases 3-fold at pH 2 with ThT, which binds β -sheets and yields fluorescence enhancement around 485 nm upon excitation with a 440-nm laser. All data were background-subtracted and were repeated multiple times, yielding similar results.

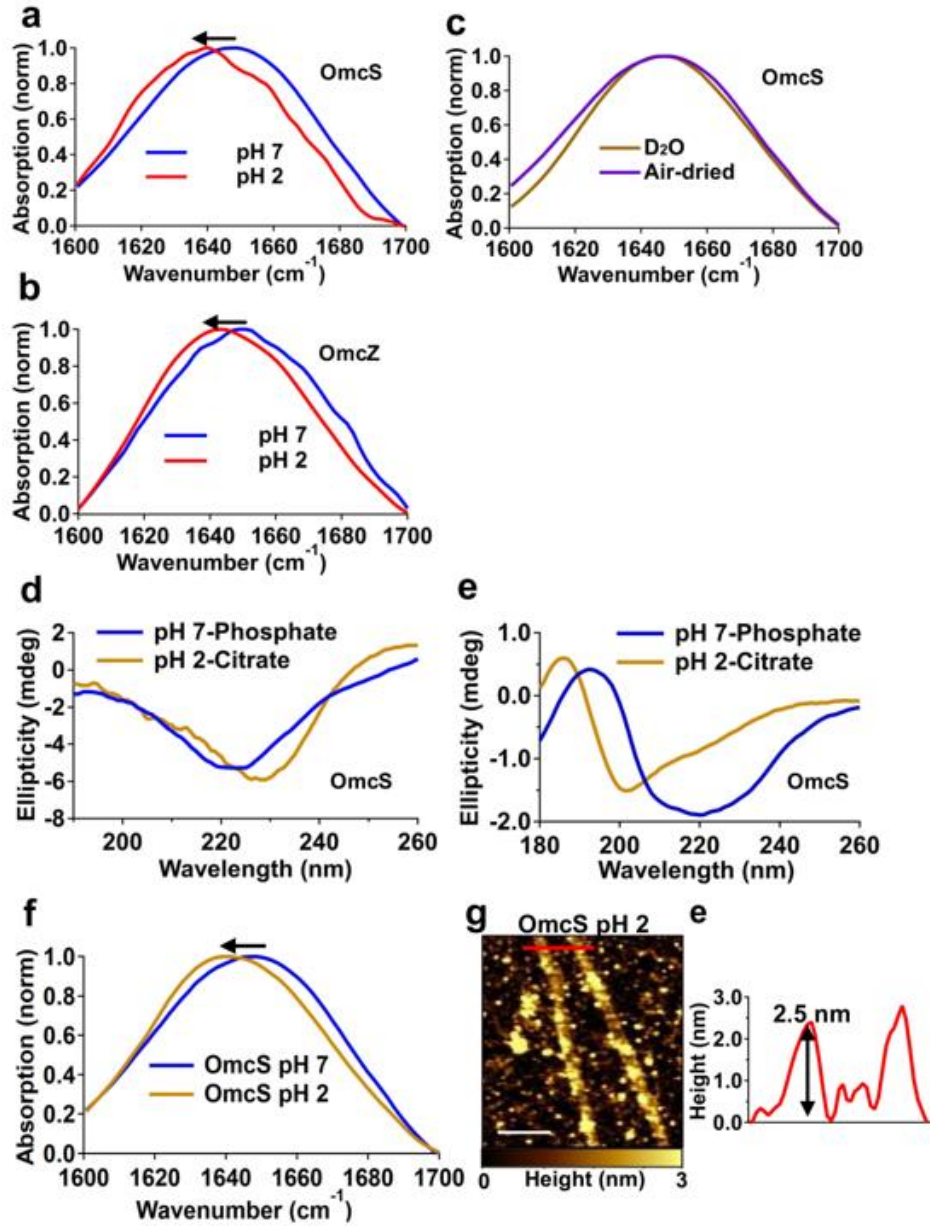


Figure 4.4 Bulk FTIR Spectra of OmcS and OmcZ Nanowires Show Transition to β -sheets at pH 2 and Conformation Change is Independent of Buffers

FTIR spectra at pH 7 and pH 2 for (a) OmcS nanowires and (b) OmcZ nanowires showing a red shift, consistent with transition to β -sheets. (c) Water does not contribute to the amide I spectra because OmcS nanowires at pH 7 under air-dried and D₂O conditions display similar spectra. (d, e) OmcS nanowires at pH 7 and pH 2 in 10 mM Potassium Phosphate and 20 mM Citrate buffer characterized by (d) Solution CD spectra and (e) Solid-state CD spectra. (f) FTIR spectra for OmcS nanowires in Citrate buffer at pH 2 showing a red shift, consistent with transition to β -sheets. (g) Representative AFM image and (h) corresponding height profile at a location shown by a red line in g for OmcS nanowires in citrate buffer at pH 2 under air-dried conditions. Scale bar, 200 nm.

Raman spectroscopy of nanowires of the W51W57 strain in the amide I mode showed that α -helical regions (Rygula, Majzner K. et al. 2013) (1637 cm^{-1}) at pH 7 transform into β -sheets (Rygula, Majzner K. et al. 2013) (1665 cm^{-1}) at pH 2 (**Figure 4.3a**), consistent with IR *s*-SNOM studies on individual OmcZ nanowires. The amide III mode was also sensitive to conformational changes. For nanowires of the WT strain, the coil/turn loop region (1240 cm^{-1}) and part of the α -helical region ($\sim 1270\text{ cm}^{-1}$) transformed into β -sheets (Rygula, Majzner K. et al. 2013) (1218 cm^{-1}) at pH 2 (**Figure 4.3b**), consistent with IR *s*-SNOM studies on individual OmcS nanowires.

In addition, the CD spectra of WT nanowires at pH 7 displayed the characteristic α -helical structure with minima near 208 nm and 222 nm (**Figure 4.3c**) in agreement with OmcS nanowire structure (Wang, Gu et al. 2019). At pH 2, the intensity at both absorption minima decreased, indicating lower α -helical content. Importantly, a new absorption minimum appeared at 204 nm (**Figure 4.3c**), consistent with a higher β -sheet content. In contrast, nanowires of the W51W57 strain had high content of β -sheets at both pH 7 and 2 (**Figure 4.3d**), in agreement with our IR *s*-SNOM studies on individual OmcZ nanowires. The amounts of α -helix and β -sheet quantified with CD Pro (CDSSTR method) (Sreerama and Woody 2000, Greenfield 2006) were consistent with the IR *s*-SNOM results.

We also measured the fluorescence emission of thioflavin T, a fluorescent dye that emits strongly near 485 nm upon binding to β -sheets (Guterman, Kornreich et al. 2016), in the presence of nanowires. Thioflavin T binding was homogenous and specific to nanowires (**Figure 4.3e**). Fluorescence emission of nanowire-bound thioflavin T

increased ~3 fold as the pH was reduced from 7 to 2 (**Figure 4.3f**), consistent with the pH-induced β -sheet formation in OmcS nanowires. Nanowires of the W1W57 strain showed a high β -sheet content, as evidenced by substantial thioflavin T fluorescence at pH 7 (**Figure 4.3f**), in agreement with studies on OmcZ nanowires (**Figure 4.2c**). These four complementary methods further show the pH-induced structural transition to β -sheets in OmcS and OmcZ nanowires as identified by IR *s*-SNOM.

4.3.3 Low pH induces change in histidine coordination in OmcS nanowires

I hypothesized that the protein conformational changes would also affect the electronic environment of the hemes and sought to examine these changes. Specifically, I worked with other members of the Malvankar lab and collaborators to utilize electron paramagnetic resonance (EPR), UV-Vis, and X-ray absorption spectroscopy and other methods to examine changes to the heme moieties in OmcS nanowires at pH 2.

At pH 2, an axial EPR signal ($g_z \neq g_y = g_x$) was observed near $g = 6$ from a high-spin ferric (HS) with $S=5/2$ (**Figure 4.5a,b**). This resonance indicates a tetragonal symmetry of the high-spin heme due to the 4-fold symmetry of the porphyrin-ring around the magnetic *z*-axis (Blumberg and Peisach 1971, Peisach, Blumberg et al. 1971) and is indicative of loss of an axial histidine ligand. Low-spin (LS) heme features were also present at pH 2 (**Figure 4.5b**) that were similar to the identified LS1 and LS3 species observed at higher pH. The LS3 signal observed at pH 10.5 is similar to the spectra of hemes with a hydroxide ligand (Blumberg and Peisach 1971, Andersson, Lipscomb et al. 1986). However, the LS3 signals observed at pH 2 and 7 are unlikely to be from

hydroxide-coordinated hemes because a hydroxide ligand should be protonated at low pH. Instead, the LS3 signal could signify a feature pertaining specifically to hemes arranged in a filament. HALS heme signatures, previously assigned to heme 3 and 6 in higher pH's, were absent in the pH 2 spectrum. Hence, our results indicate that these hemes have histidine displaced at one of the axial positions. This loss of axial histidines is likely due to a higher energy configuration of *d*-orbitals in near-perpendicularly oriented axial imidazole-rings of a HALS heme compared to a LS heme 22,(Yatsunyk, Dawson et al. 2006). By integrating the spectra, we also quantified the relative amount of high-spin versus low-spin heme species and found an approximate 1:1 ratio, suggesting that ~50% of the hemes have lost one of the axial histidine ligands at pH 2. Our results are similar to *c*-554, which shows 75% HS hemes at pH 2 (Andersson, Lipscomb et al. 1986), haemoglobin (Akiyama, Fukuda et al. 1994) and horse as well as yeast cytochrome *c* that also show the loss of axial coordination at lower pH. In myoglobin, a distal histidine coordinating to the heme stabilizes a water molecule within the heme pocket by accepting a hydrogen bond (Esquerra, Jensen et al. 2008). The protonation causes histidine to swing out of the heme pocket (Esquerra, Jensen et al. 2008). A similar mechanism could explain the loss of histidine coordination in OmcS nanowires at lower pH.

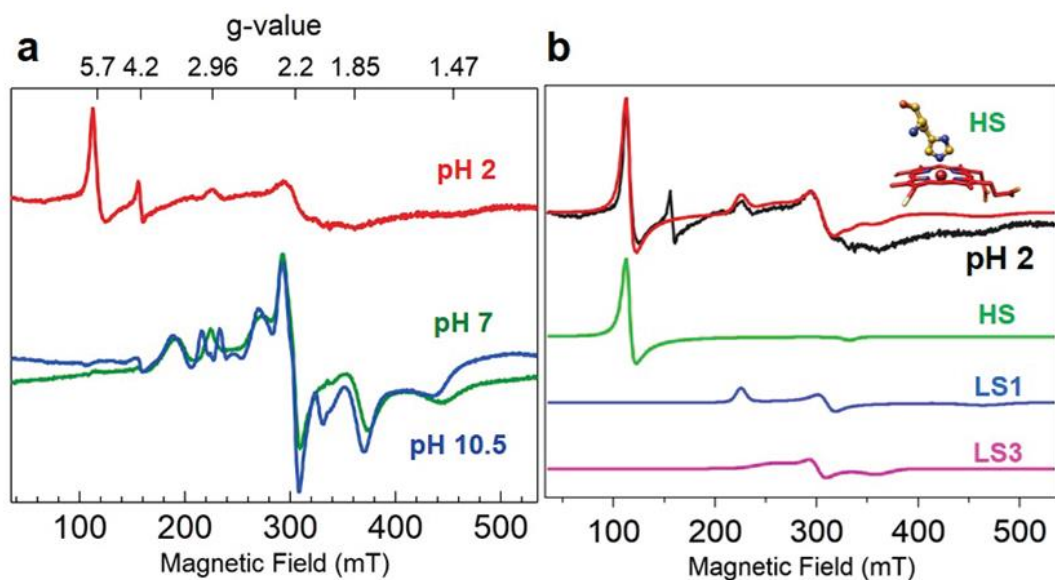


Figure 4.5 Loss of Axial Histidine Ligand to Heme at pH 2 in OmcS Nanowires
(a) Overlay of spectra at pH 2, 7, and 10.5. **(b)** Deconvolution of the pH 2 spectrum. The experimental spectrum (black) is overlaid with the sum of the simulation of heme components (red). Simulations of individual high-spin (HS) and low-spin (LS) hemes. **Inset:** Representative structure for simulated high-spin heme.

X-ray absorption spectroscopy (XAS) is another powerful method to probe the role of ligand binding on heme conformation (Kleinfeld, Frenkel et al. 2003, Dai and Boon 2011). The XAS spectrum of a metalloprotein informs metal oxidation state, metal spin state, the number and type of ligands bound to the metal, and metal-ligand bond lengths. The maximum of the first derivative of the X-ray absorption coefficient at the K-edge energy of iron corresponds to the excitation energy of the core shell electron. The X-ray absorption edge is directly related to the oxidation state of the iron in the protein and can be used to probe the flow of electron density between the metal center and surrounding ligand. For higher oxidation states, the X-ray absorption edge shifts to higher energies due to an increase in the core shell electron binding energy (Kleinfeld, Frenkel et al. 2003, Dai and Boon 2011).

We found the rising-edge energy positions of heme irons in OmcS nanowires at 7118.8 eV and 7120.6 eV for pH 10.5 and pH 2, respectively, at the 1st inflection point (**Figure 4.6a,b**). Thus, our work shows that the high-spin heme irons in OmcS nanowires at pH 2 are shifted ~ 1.8 eV higher in energy compared to the low-spin heme irons at pH 10.5 in a manner similar to hydroxy-myoglobin that also shows comparable edge-shift (~4 eV) due to spin-state change (Della Longa, Pin et al. 1998).

Extended X-ray Absorption Fine Structure (EXAFS) spectra for OmcS nanowires at pH 10.5 displayed a first peak which corresponds to an Fe-N distance (Korshin, Frenkel et al. 1998, D'Angelo, Lapi et al. 2008) of 1.88 Å (**Figure 4.6c,d**). The limited spatial resolution in EXAFS spectra does not allow us to discriminate between the contributions of the four porphyrin-ring nitrogens vs. the two axial nitrogens of imidazole-rings that are expected to have different bonding distances from iron (Korshin,

Frenkel et al. 1998, D'Angelo, Lapi et al. 2008). The ligand coordination number, averaged over all heme iron ions determined from EXAFS was 3.4 ± 0.7 for OmcS nanowires at pH 10.5. Given that four porphyrin-ring nitrogens and two imidazole-rings axial nitrogens contribute to the EXAFS spectrum (**Figure 4.6a inset**), this result indicates that axial Fe-N bonds are much weaker than those of the porphyrin ring nitrogens and, consequently, have much larger bond length disorder compared to the equatorial ones, preventing their detection by EXAFS (Korshin, Frenkel et al. 1998, D'Angelo, Lapi et al. 2008). In contrast, EXAFS at pH 2 showed 5.3 ± 1.0 ligands, indicating that, in addition to the 4 equatorial ligands from porphyrin ring, a contribution from an axial ligand (from an imidazole ring) was also detectable. This finding of both a strong contribution of one axial ligand partner for heme irons in OmcS nanowires at pH 2 and weak contribution of two axial ligands for heme irons at pH 10.5 explains the more intense 1st peak in EXAFS at pH 2 than at pH 10.5 (**Figure 4.6c,d**). These EXAFS results, combined with the EPR studies showing the loss of axial histidine ligand, suggest a higher degree of structural ordering of hemes in OmcS nanowires at pH 2 that could explain the observed 100-fold increase in conductivity (**Figure 4.1c, above**).

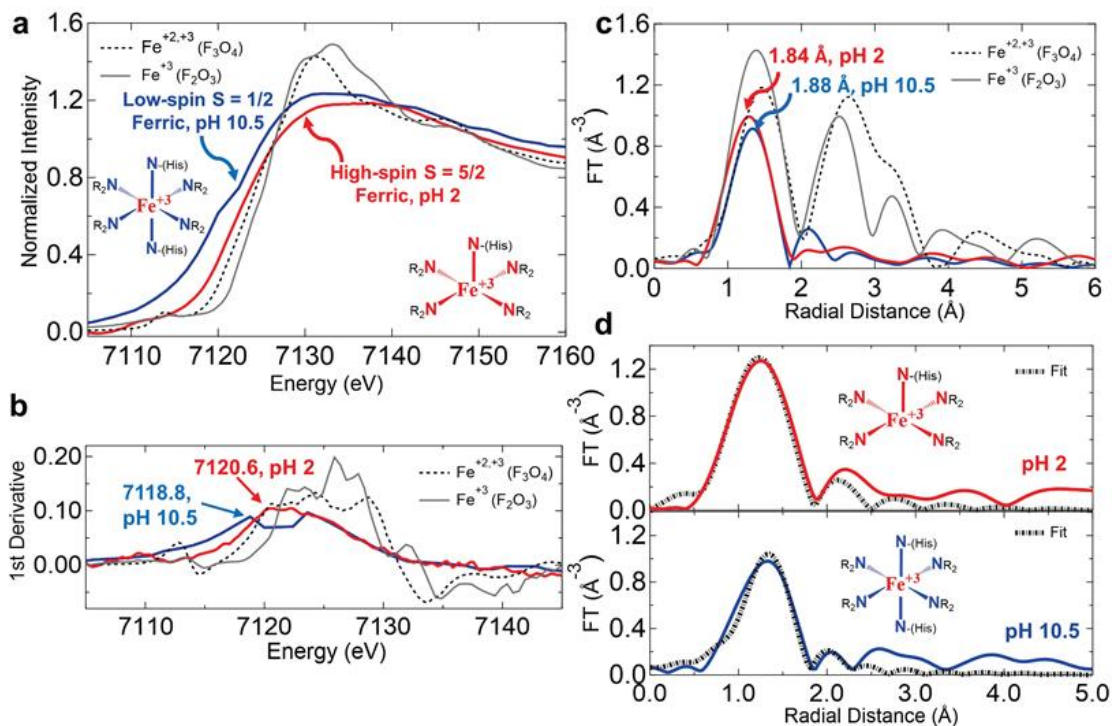


Figure 4.6 X-Ray Absorption Spectroscopy Revealed a Loss of Axial Coordination by Histidine in OmcS Nanowires at pH 2

(a) Fe K-edge XAS data for ferric OmcS in pH 10.5 (blue) and pH 2 (red) and ferric (Fe^{3+}) iron standard (grey), and mixed ferrous and ferric (Fe^{2+} , Fe^{3+}) iron standard (black dotted line). (b) The Fe K-edge first-derivative spectra with first inflection-point energies. (c) Fourier transform magnitudes (FT) of the k^2 -weighted Fe K-edge EXAFS spectra for OmcS nanowires and iron standards. An increased intensity in pH 2 for a larger Fe-N coordination. (d) FTs of the EXAFS data and fits for OmcS nanowires at pH 2 and 10.5.

UV-vis spectroscopy of OmcS nanowires at pH 7 showed characteristic features of oxidized *c*-type cytochromes with low-spin hemes, with a strong Soret absorption at 410 nm and broad Q-bands at ~530 nm and ~565 nm (Ikezaki and Nakamura 2002) (**Figure 4.7a,b**). As expected, reducing the nanowires shifted the Soret absorption to 420 nm with accompanying sharpening of the Q-bands at ~524 nm and ~553 nm (**Figure 4.7a**). At pH 2, the Soret band showed a 30-nm blue shift to 380 nm (**Figure 4.7c**), which is indicative of the high-spin hemes (Ikezaki and Nakamura 2002). At pH 2, a new band appeared at 634 nm (**Figure 4.7b**), which is likely the porphyrin → Fe(III) charge transfer band observed in high spin hemes (Vickery, Nozawa et al. 1976, Andersson, Lipscomb et al. 1986). Thus, UV-vis spectroscopy confirmed the formation of high-spin hemes at pH 2.

To directly evaluate whether the blue shift is due to loss of histidine coordination, I worked with collaborators to perform time-dependent density functional theory (TD-DFT) calculations to simulate the absorption spectra of low-spin bis- and high-spin mono-imidazole or aqua-imidazole-ligated hemes (**Figure 4.7d**). The simulations showed that the mono-imidazole-ligated heme population should show a 30-nm blue shift relative to that of the bis-imidazole-ligated species, in quantitative agreement with the experimental data. We also found a similar 22-nm blue shift if a water molecule fills the vacant axial site of the mono-imidazole species, confirming that the observed blue shift is due to loss of axial histidine coordination.

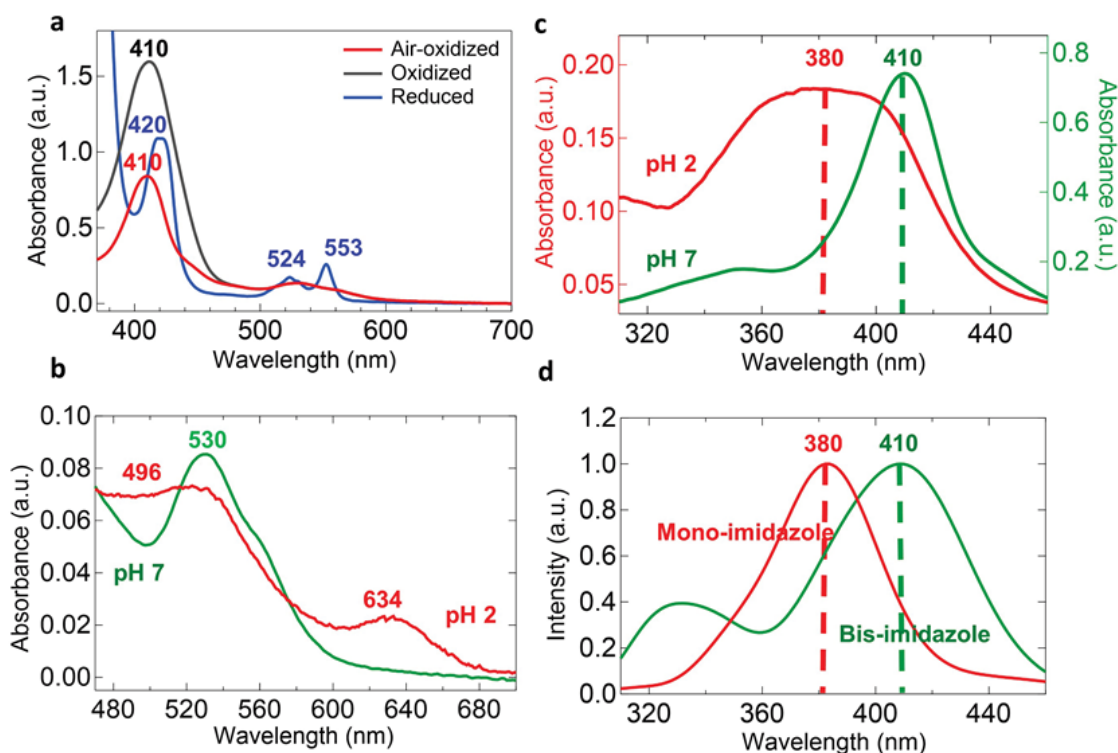


Figure 4.7 Experimental and Computed UV-Vis Spectra of Nanowires Confirm the Loss of Axial Histidine Coordination at pH 2.

(a) Experimental UV-vis spectra of OmcS nanowires at pH 7 under oxidized and reduced conditions (b) Zoomed-in spectra showing the diminished Q-bands at pH 2 and appearance of the charge-transfer band. (c), Experimental UV-vis spectra of OmcS nanowires showing the 30-nm blue shift at pH 2 vs. pH 7 for the Soret region. (d), Computed UV-vis spectra showing the 30-nm blue shift for mono- vs. bis-imidazole heme.

4.3.4 Evidence of excitonic coupling in OmcS nanowires at low pH

Upon equilibration at pH 2, the UV-vis spectra of the OmcS nanowires showed a splitting of the Soret band at 380 nm into components at 370 nm and 400 nm, as confirmed by the band decomposition analysis (**Figure 4.8a**). The appearance of a red-shifted band at ~400 nm is the hallmark of J-aggregate formation (Villari, Mineo et al. 2012, Fry, Wood et al. 2017, Wang, Zhong et al. 2017). This red-shift is indicative of extended slipped π - π stacking that confers intermolecular electron delocalization which enhances conductivity (Villari, Mineo et al. 2012, Fry, Wood et al. 2017, Wang, Zhong et al. 2017). In addition, the new bands covered a broader region of the spectrum which indicated extensive electron delocalization due to the conjugated porphyrin networks from the extensive self-reorganization (Wang, Zhong et al. 2017). The Q-bands and the appearance of a 634 nm peak (**Figure 4.8b**) are particularly indicative of excitonic coupling which is advantageous to exciton transport (Wang, Zhong et al. 2017).

I evaluated the possibility of excitonic coupling in OmcS nanowires due to the formation of J-aggregates by working with collaborators again to simulate the absorption spectra for hemes at several inter-heme geometries (**Figure 4.8b insets**). Of the examined geometries, we found that the absorption spectrum for OmcS at pH 2 can be reproduced by a face-to-face “sandwich” configuration of penta-coordinated heme models that are sufficiently close together (**Figure 4.8b**). Therefore, the simulations suggest that excitonic coupling could explain the splitting of Soret band observed at pH 2.

To further evaluate the possibility of excitonic coupling in OmcS nanowires, I performed circular dichroism (CD) spectroscopy in the visible region of the electromagnetic spectrum (**Figure 4.8c**). The CD spectra of OmcS nanowires at both pH

7 and pH 2 showed large bisignate Cotton effects, indicating exciton-coupled hemes held in a chiral environment (Sanders, Kale et al. 2017, Oohora, Fujimaki et al. 2018). The CD spectra exhibited a 30-nm blue shift at pH 2 (**Figure 4.8c**), in agreement with UV-vis studies (**Figure 4.7a**). The presence of the Cotton effect suggests the transition dipoles of the hemes in OmcS nanowires interact with the chiral environment created by the filamentous assembly of the protein in a manner similar to synthetic peptide assemblies (Sanders, Kale et al. 2017).

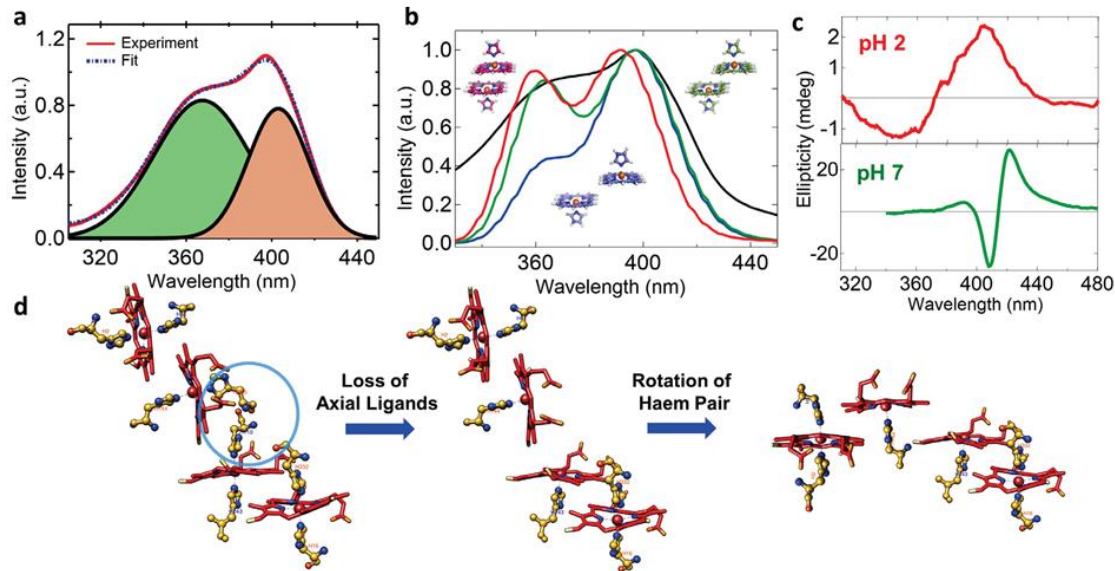


Figure 4.8 Evidence for Excitonic Coupling in OmcS Nanowires

(a) Splitting of the 380-nm Soret peak at pH 2 into two peaks centered at 370 nm and 400 nm. (b) Comparison of the experimental spectrum for OmcS at pH 2 (black) and simulated spectra for dimer models of penta-coordinated Fe(III) porphyrins with inter-iron distances of 5.8 Å. (red), 8.1 Å. (green), and 11.4 Å (blue). (c) Circular dichroism spectra of OmcS nanowires at pH 2 (red) and pH 7 (green). (d) Model for the formation of J-aggregate like structure in OmcS nanowires upon loss of heme axial ligands shown in the circle.

4.4 Discussion

Recent studies have emphasized the need for understanding the mechanism of environmentally-triggered conformational changes in proteins for the design of protein-based functional materials (Boyken, Benhaim et al. 2019). Our finding that coil/turns transform into β -sheets in microbial nanowires provides a mechanism for pH-induced conformational changes that reduce their diameter and enhance stiffness and conductivity. Lowering the pH can induce the formation of β -sheets in synthetic peptides (Cerpa, Cohen et al. 1996, Koga, Taguchi et al. 2003, Cote, Fu et al. 2014) and the interaction of cytochrome *c* with SDS causes a transition to β sheets (Haldar, Sil et al. 2015). A similar effect could explain the pH-induced formation of β -sheets that reduces the diameter of microbial nanowires.

Another mechanism that could account for the pH-induced reduction of nanowire diameter is a dehydration effect that causes proteins and other polymers to adopt a more compact structure at lower pH (Durchschlag and Zipper 2004, Esquerra, Jensen et al. 2008, Wang, Ye et al. 2015). In particular, distal histidine coordinating to heme can stabilize the water molecule within the heme pocket by accepting a hydrogen bond (Esquerra, Jensen et al. 2008). At low pH, the histidine is protonated and swings out of the heme pocket, thus destabilizing the water occupancy and leading to dehydration (Esquerra, Jensen et al. 2008). Additional structural studies will help evaluate these possibilities.

Our findings that microbial nanowires contain β -sheets contrast with prior studies that have assumed that nanowires of both *G. sulfurreducens* WT and W51W57 strains are made up of PilA with a purely α -helical structure (Malvankar, Vargas et al. 2015). Solution NMR studies of the PilA monomer have indicated helical structure even at pH 5 (Malvankar, Vargas et al. 2015). Therefore, combined with the studies discussed in Chapter 3, our structural and functional studies further support the conclusion that the highly conductive microbial nanowires are composed of *c*-type cytochromes and not PilA.

The conformational change and loss of histidine coordination in OmcS nanowire hemes at low pH that leads to higher structural ordering and excitonic coupling suggests the hemes assemble into a J-aggregate-like structure similar to other bacterial hemes (Mattle, Zeltina et al. 2010) and synthetic porphyrin nanowires (Villari, Mineo et al. 2012, Fry, Wood et al. 2017, Wang, Zhong et al. 2017). For example, a brickwork-type J-aggregate (Xu, Liao et al. 2012) can be formed in OmcS nanowires by rotation of the pair of heme 4 and 5 relative to the pair of hemes 2 and 3 (**Figure 4.8d**). Additional structural studies will help test these possibilities. In addition to this conformational change, the redox potential of hemes can change upon the loss of axial coordination (Liu, Chakraborty et al. 2014). Furthermore, the reorganization energy for electron transfer is also likely to change for the reoriented hemes (Seyedi, Waskasi et al. 2017). Both effects could also contribute to the increased nanowire conductivity in addition to the increased excitonic coupling observed in the OmcS nanowires.

In summary, we have demonstrated the feasibility of manipulating the production and structure of protein nanowires to control their conductivity and stiffness. These

studies demonstrated the capabilities of multimodal nanospectroscopic approaches for visualizing and quantifying the large-scale conformational changes in biomolecules. Precise control of electronic and mechanical properties of nanowires can be achieved via targeted environmental changes such as changing the pH which alters heme stacking or applying an electric-field. Previous studies have shown that an electric field can activate a synthetic gene circuit by creating an oxidizing environment (Tschirhart, Kim et al. 2017). Additional studies are required to evaluate if a similar mechanism plays a role in these natural systems. Our quantitative method to visualize conformation-induced functional changes is likely applicable to a variety of molecular systems. With the OmcZ nanowires displaying a million-fold higher conductivity than synthetic biodegradable materials (Someya, Bao et al. 2016), we anticipate these new materials will introduce several new features urgently needed for the next generation of bioelectronics, including low cost, ease of synthesis, lack of toxicity, mechanical flexibility, as well as scalable and facile processing with controlled biological properties (Someya, Bao et al. 2016).

By homogenizing the heme environment at physiological pH, our results explain how soil bacteria use protein nanowires to transport electrons for respiration and energy sharing to electron acceptors (Malvankar, Vargas et al. 2011) and syntrophic partners (Summers, Fogarty et al. 2010) that are hundreds of micrometers away. Our studies suggest that microbial nanowires are a new class of metalloproteins with highly tunable electronic properties that can transport both electrons and excitons at rates and distances unprecedented in biomolecular systems via unique micrometer-long seamless stacking of hemes. These nanowires thus represent a nanoscale laboratory for fine-tuning of catalytic and electron transfer rates by rationally engineering the cofactors and amino acid

residues. Non-natural amino acid ligands serving as histidine analogs (Xiao, Peters et al. 2014) change the catalytic properties of metalloenzymes (Xiao, Peters et al. 2014, Hayashi, Tinzl et al. 2018). Therefore, similar to monomeric metalloproteins (Moore and Fasan 2019), our studies provide the foundation for either targeted removal or substitution of ligands as a promising strategy to systematically fine-tune the reactivity and conductivity of microbial nanowires. This rational design can achieve different regimes of electron and exciton transport for a new field of metalloprotein-based self-replicating and highly resilient electronic materials for a wide range of applications, including artificial photosynthesis, catalysis, bioelectronics as well as environmental and pH sensing.

5 Identifying the pathway for electrons in *Geobacter*

extracellular electron transfer and implications in the field

5.1 Introduction

Geobacter species perform key roles in their native soil and sediment environments. They aid in bioremediation by reducing and solubilizing soil contaminants such as uranium and chromium. In a process termed Direct Interspecies Electron Transfer (DIET) *Geobacter* use their conductive nanowires as conduits to transfer electrons to other bacteria that lack other electron donors for their own metabolism (Summers, Fogarty et al. 2010). These processes, as well as the reduction of Fe(III) and Mn(IV) oxides, rely upon OmcS and cannot be complemented by OmcZ in $\Delta omcS$ mutant strains. Many prior studies have focused on identifying the proteins required for transferring electrons from the inner membrane to OmcS and finally to the electron acceptor. A key step in determining the order of who passes electrons to whom is characterization of reduction potential. Specifically, for electron transfer to be thermodynamically favorable, the transfer needs to occur from a donor with a lower reduction potential to an acceptor with a more positive reduction potential. Earlier attempts at characterizing the conduits faced quite the quandary: the last step in the process – OmcS – was previously characterized as having an apparent midpoint reduction potential (E_{app}) of -212 mV vs. SHE, a more substantially negative value than the periplasmic cytochromes (~ -150 mV) that come before it in the pathway, suggesting a large thermodynamic barrier for electron

transfer. These studies were completed on a detergent- and heat-treated OmcS sample, therefore I sought to characterize the native OmcS nanowires.

5.2 Results

5.2.1 The OmcS nanowires have a midpoint reduction potential comparable to periplasmic cytochromes for efficient electron transfer

I determined the reduction potential of the OmcS nanowires with a spectroelectrochemistry approach, where a potentiostat controls the potential of a solution containing the OmcS nanowires and a soup of soluble redox mediators that help the solution potential reach equilibrium quickly. Tracking changes in the OmcS UV-vis spectra as the potential of the solution is changed and OmcS transitions from fully oxidized to fully reduced (and back the opposite direction) allows for a determination of the potentials over which OmcS is redox active and an evaluation of the apparent midpoint reduction potential (E_{app}). Specifically, monitoring the changes in absorbance allows for the calculation of a reduced fraction at each potential. I collected data in both the oxidative and reductive directions to evaluate hysteresis (**Figure 5.1a**). The results obtained showed that both curves are essentially superimposable, indicating that the oxidation and reduction of the nanowire is fully reversible and that no major permanent conformational changes were detectable in the vicinity of the heme groups. The redox curve covers a significant range of potentials (- 340 and 0 mV) correlating with a distinct redox behavior of the heme groups.

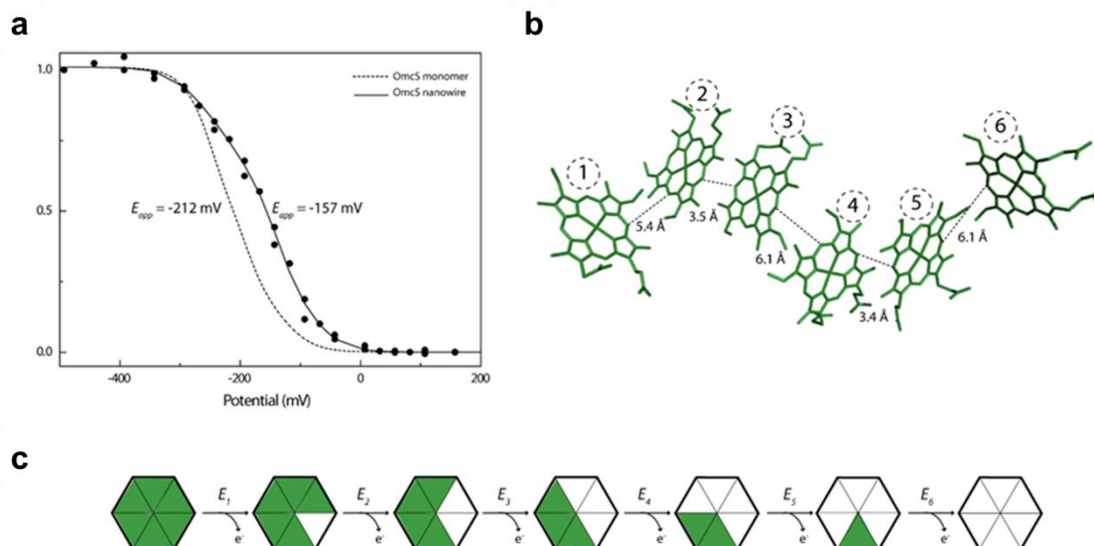


Figure 5.1 Redox Characterization of OmcS Nanowires

(a) Spectroelectrochemical titration of OmcS nanowires (circles). The solid line indicates the result of the fitting to the experimental points. The fitting for the OmcS monomer is represented by the dotted line for comparison. (b) Heme core of the OmcS nanowires subunit (PDB code 6EF8). The numbers inside a circle indicate the heme numbering. Distances between heme edges are also given. (c) Representation of the sequential model with the six single-electron redox steps connecting the macroscopic redox stages. In this scheme each triangle represents a heme group, which can be either reduced (green) or oxidized (white). E_x ($x = 1$ to 6) represents the macroscopic reduction potential associated with each oxidation redox step.

The cryo-electron microscopy (cryo-EM) structure of the OmcS nanowire showed that the six hemes are closely stacked and their chemical environment is different (Wang, Gu et al. 2019). The minimum observed edge-to-edge distances are within 3.4 - 6.1 Å and the Fe-Fe distances within 8.7 - 12.5 Å, providing a continuous path for electron flow (**Figure 5.1b**). Thus, the heme irons in the OmcS nanowire are sufficiently close to each other to mutually modulate their redox properties during the redox cycle of the protein (Fonseca, Paquete et al. 2012).

From a simple electrostatic view of the heme iron charge, the loss of a negative charge caused by the oxidation of one heme is expected to stabilize the reduced form of its neighbor and, concomitantly, increase its redox potential value. The shape of the redox titration curve (**Figure 5.1a**) indicates that the oxidation profile of each heme group is affected by the oxidation state of its neighbor (redox interactions), in accordance with the expectation since the hemes are in close proximity with each other. Consequently, a model that considers six independent redox centers is conceptually inappropriate to fit the redox curve and to determine the reduction potential values for the OmcS nanowire (Wang, Stankovich et al. 1991). For this reason, the redox titration data were fitted to a sequential model that considers six single-electron redox steps connecting the six possible macroscopic redox stages for a hexaheme cytochrome (**Figure 5.1c**); however, further experiments such as redox titrations monitored by nuclear magnetic resonance spectroscopy need to be completed to fit the data with a model that takes into account the coupling between hemes to determine the precise reduction potentials of the individual hemes. The apparent mid-point reduction potential (E_{app}) and the macroscopic reduction potentials (E_{1-6}) for the different oxidation steps are listed in **Table 2**.

Table 2 Apparent midpoint and macroscopic reduction potential values for OmcS nanowires and monomer at pH 7. The apparent midpoint reduction potentials (E_{app}) correspond to the point at which the oxidized and reduced fractions are equal. The macroscopic reduction potentials for each oxidation step (E_1 to E_6) are also indicated.

Reduction potentials (mV versus SHE)							
	E_{app}	E_1	E_2	E_3	E_4	E_5	E_6
OmcS nanowire	-157	-281	-220	-168	-138	-121	-70
OmcS monomer	-212	-275	-249	-239	-190	-180	-120

The analysis of **Table 2** shows that the six macroscopic reduction potential values are negative and different from each other. Such variation illustrates the versatility of multiheme versus monoheme cytochromes. In fact, the presence of spatially close redox centers makes possible their modulation by redox interactions and thus expanding the protein's range of redox activity. On the other hand, in a monoheme cytochrome the functional range of redox activity is narrower and more limited by the very steep Nernst curve.

The E_{app} value (i.e., the point at which the oxidized and reduced fractions are equal) determined for the OmcS nanowire is – 157 mV vs. SHE. This matches values determined by another member of the Malvankar group, Catharine Shippis, using direct electrochemistry techniques such as cyclic and differential pulse voltammetry. Further, this also matches the reduction potential of $\Delta omcZ$ biofilms, where OmcS is the most prevalent redox-active protein. This value is significantly higher than the E_{app} value determined for the detergent- and heat-treated OmcS monomer (– 212 mV) using the same methodology (Qian, Mester et al. 2011) (**Table 2**). The observed differences are most likely correlated to the different solvent exposure of the heme groups in the

monomer and nanowire: in fact, hemes 1 and 6 are considerably more exposed to the solvent in the monomer than in the nanowire, which correlates well with the monomer's smaller E_{app} value (Dolla, Blanchard et al. 1994).

5.3 Discussion

While OmcS is known to be essential for several native extracellular electron transfer steps in *Geobacter* species, its prior characterization as a monomeric cytochrome with a midpoint reduction potential of -212 mV vs. SHE has confused the field towards its exact role, as this potential is more negative than the periplasmic cytochromes and therefore transfer to OmcS would have been thermodynamically unfavorable.

With this updated spectroelectrochemical characterization I provide two important updates: first, the more positive midpoint reduction potential helps explain why it would be thermodynamically favorable for OmcS to be the final step in the electron transfer chain. Second, is the wide range of potentials over which OmcS is redox-active (a range of over ~ 350 mV). While at first this appears to be a surprising finding, it could serve as an evolutionary adaptation that allows *Geobacter* to use the same machinery to transfer electrons to a wide range of electron acceptors in their environment.

6 Conclusions & Next Steps

6.1 Conclusions

In this thesis, I have presented several significant updates for the *Geobacter* field, including an updated method for preparing anaerobic cultures and assembling microbial fuel cells, which will help lower the barrier of entry for new investigators. I also described an updated purification protocol that produces purer filament samples. Using these methods will allow more rigorous study of both the physiology of *Geobacter* and other electrode-respiring bacteria as well as the characterization of the conductive nanowires themselves.

I have shown that *G. sulfurreducens* assembles OmcS nanowires to complete respiration in its native environment when short-range extracellular electron transport is required for survival, and further that it forms nanowires of OmcZ when grown in engineered biofilms where long-distance electron transport is needed. One of the reasons that cytochromes were not seriously considered as candidates for the nanowire-forming protein in prior studies was that one single cytochrome was not essential for explaining *Geobacter* physiology: it was easier to assume that one protein (PilA) formed the nanowires and that the changes in conductivity observed were a simply a result of conformational changes; however, the finding that *G. sulfurreducens* can form two different nanowires depending on growth condition more sufficiently explains the *Geobacter* extracellular electron transfer phenomena.

Developing the multimodal nanospectroscopic technique not only helped us identify the OmcZ nanowires, but also led to the insight regarding the conformational change to β -sheet-rich structures at low pH that increase conductivity, reduce diameter, and increase stiffness in both the OmcS and OmcZ nanowires. Further studies on OmcS illustrate that these work in conjunction with a change in heme coordination to stack hemes better for higher conductivity. Finally, by characterizing the midpoint reduction potential of the native OmcS nanowires I have shown that it can serve as the terminal *Geobacter* component in the electron transport chain to environmentally important redox partners such as minerals, soil contaminants, and other bacteria.

6.2 Future Directions

There are many lessons to be gained from the work in this thesis; however, one that immediately jumps forward is the need for high resolution structures. I have used many techniques to characterize the conductive OmcS and OmcZ nanowires, but the next step for validating these models and hypotheses is to obtain cryo-EM reconstructions of both nanowires at pH 2 and the OmcZ nanowires at pH 7. These data will provide further insight into the mechanisms of their conductivity and might help unlock ways in which we can build conductive nanowires from other filaments in other microorganisms. A significant obstacle is in preparing the cryo-EM grids, as the nanowires tend to aggregate into bundles at low pH which limits the ability to obtain high resolution reconstructions. Optimizing cryo-EM grid preparation conditions such as the buffer, blotting time, and sample concentration are thus critical for completing this project. A reconstruction of the OmcZ nanowire structure will allow us to compare if the interesting features in the OmcS nanowires, such as the coordination to one heme with histidines from two adjacent

monomer subunits, is a common feature or one unique to OmcS. The structures at pH 2 will allow us directly to observe the features that are changing and enhancing conductivity, and will further allow computational studies to build models for how this enhanced electron transfer occurs.

There are several experiments in this thesis that were completed on OmcS nanowires but have yet to be completed on the OmcZ nanowires. With new purification protocols these experiments can be completed which will provide further information on what drives the conductivity in the OmcZ nanowires.

A significant body of work exists on the wild-type *Geobacter sulfurreducens* physiological relevance in its native environment and in electrode-grown biofilms. With the revelations that OmcS and OmcZ can form filaments, further experiments on mutant strains with the genes for OmcS and OmcZ deleted can provide insight into how the nanowires might work synergistically to produce conductive biofilms.

This work focused on *Geobacter sulfurreducens*; however, there are other *Geobacter* strains that have the capability of conducting extracellular electron transfer; therefore, future work can investigate these other strains to see if they also form OmcS and OmcZ nanowires. Further, by investigating if other bacteria outside of *Geobacter* have OmcS and OmcZ homologs we can search for other microorganisms that can form conductive filaments.

The type II secretion system machinery requires 20+ proteins to work together to assemble a type IV pilus. It is still unclear whether *G. sulfurreducens* is using these components to assemble its cytochrome filaments or if it is using other assembly

machinery altogether. Genetic knock-out studies and pull-down assays will allow future researchers to determine what proteins are required to assemble these conductive filaments, which then might enable researchers to use a chassis system in a bacterium such as *E. coli* to produce the filaments *en masse*. The future is very bright for *Geobacter*, conductive protein nanowires, and electromicrobiology. While this thesis was *A Tale of Two Nanowires*, the full story is only just beginning.

7 Methods

7.1 SDS-PAGE

For polyacrylamide gel electrophoretic separation (SDS-PAGE), filament samples were prepared as per manufacturer's instructions using 2.5 % sodium-dodecyl sulphate (SDS) to disassemble filaments into their constituent monomers. The samples were boiled in SDS sample buffer that included β -mercaptoethanol for 12 min. The samples were run on a 16% Tricine protein gel (ThermoFisher Scientific, Carlsbad, CA) initially at constant voltage of 30 V for 18 minutes before changing to 190 V for 12 minutes. Precision Plus Protein Prestained molecular weight standards (BioRad, Hercules, CA) and Low Range Protein Ladder (Thermo Scientific) were used to compare the molecular weight of cytochromes in the filament preparations. Gels were immediately washed at least 3 times with ultra-pure deionized water over a 1-hour period, stained with Coomassie R-250 stain (Thermo Scientific, Rockford, IL), and destained overnight.

7.2 Immunoblotting

Custom polyclonal anti-OmcZ antibody was synthesized by LifeTein (New Jersey) by immunizing two rabbits with synthetic peptide sequence (DSPNAANLGTVPKGL) containing targeted epitope on the native protein, OmcZ, and then affinity purifying the serum against that peptide sequence. The antibody was used at a dilution of 1:5000 for immunoblotting. Filament preps were normalized to the initial cell mass of the starting material.

7.3 Mass spectrometry

For LC-MS/MS analysis of filament preparations, the OmcZ band (~ 30 kDa) was excised from the gel and treated with chymotrypsin to digest the protein. Proteomic analysis of the cleaved peptides from filaments was performed by the Keck Facilities at Yale University. Unique amino acid sequence matches with the OmcZ were found. For quantification of OmcZ in filament preparations, the “top three” method (Silva, Gorenstein et al. 2006, Grossmann, Roschitzki et al. 2010) was employed by quantitating the three peptides with highest intensity (Krey, Wilmarth et al. 2013). Previous study has confirmed that OmcZ contains 8 hemes through intact mass spectrometry and pyridine hemochrome assay (Inoue, Qian et al. 2010).

7.4 Bacterial strains and growth conditions

Geobacter sulfurreducens wild-type (WT) strain PCA (designated DL-1) (ATCC 51573, DSMZ 12127)(Wang, Gu et al. 2019), the *omcS* knock-out mutant strain (Mehta, Coppi et al. 2005) (designated $\Delta omcS$), the *omcZ* knock-out mutant strain (Nevin, Kim et al. 2009) (designated $\Delta omcZ$), the OmcZ knock-in strain that overexpresses OmcZ (Park and Kim 2011) (designated ZKI), strain W51W57 (Tan, Adhikari et al. 2016) and strain Aro5 (Vargas, Malvankar et al. 2013) were obtained from our laboratory culture collection. The cultures were maintained at 30 °C or at 25 °C under strictly anaerobic conditions in growth medium supplemented with acetate (10 mM) as the electron donor and fumarate (40 mM) as the electron acceptor. These strains were grown under electron acceptor-limiting conditions that increases OmcZ expression (O'Brien and Malvankar 2016). We found that *G. sulfurreducens* WT (DL1) strain primarily makes OmcS

nanowires whereas strain W51W57 overexpresses OmcZ and shows abundance of OmcZ nanowires. Therefore, unless otherwise noted, WT strain was used to focus on studies of OmcS nanowires whereas W51W57 strain was used to focus on studies of OmcZ nanowires. As described previously (Wang, Gu et al. 2019), the cells were grown in sterilized and degassed NBAF medium (O'Brien and Malvankar 2016), and 1 L NBAF medium contained the following: 0.04 g/L calcium chloride dihydrate, 0.1 g/L, magnesium sulphate heptahydrate, 1.8 g/L sodium bicarbonate, 0.5 g/L sodium carbonate, 0.42 g/L potassium phosphate monobasic, 0.22 g/L potassium phosphate dibasic, 0.2 g/L ammonium chloride, 0.38 g/L potassium chloride, 0.36 g/L sodium chloride, vitamins and minerals as listed in (O'Brien and Malvankar 2016). Resazurin was omitted and 1 mM cysteine was added as an electron scavenger. The cells were grown on electrodes under electron acceptor-limiting conditions to induce the expression of OmcZ nanowires (O'Brien and Malvankar 2016).

7.5 AFM sample preparation

Prior to all measurements, nanowires were imaged with AFM and height measurements were performed to confirm the presence of individual nanowires and to confirm their identity. IR *s*-SNOM measurements were also performed on bundles of OmcS nanowires under high pH conditions ($\text{pH} \geq 7$). These nanowires did not show any β -sheets and the results were similar to individual OmcS nanowires showing primarily α -helix as secondary structure, confirming that low pH conditions are necessary to induce the formation of β -sheets in OmcS nanowires.

For imaging with AFM or combined AFM and IR *s*-SNOM or conducting-probe AFM, 20 μL buffer containing nanowires was drop casted onto appropriate substrates.

Freshly cleaved mica (Muscovite Grade V1, SPI supplies) was used for topography imaging only whereas template-stripped gold surface (Platypus, AU.1000.SWTSG) was used for IR s-SNOM and nanoelectrode gold array was used for conducting-probe AFM. Except mica, all substrates were plasma cleaned for 10 minutes under medium plasma exposure and washed with DI water. For bulk FTIR, Raman, circular dichroism (CD), XRD and fluorescence emission spectroscopy, nanowires were directly measured in their native buffer environment. Conformation change at pH 2 in the films of OmcS nanowires in Citrate buffer was similar to Phosphate buffer. Therefore, the Citrate buffer was used for height analysis of OmcS nanowires.

Immunogold labelling of OmcZ nanowires

Transmission electron microscopy-based immunogold labelling was performed as described previously (Inoue, Leang et al. 2010). In brief, samples of purified extracellular filaments were adsorbed to plasma-cleaned carbon film-coated copper grids (400 mesh, Electron Microscopy Sciences) and incubated for 5-10 min. Samples were subsequently treated with 0.1% glutaraldehyde (supplied as 2.5% Glutaraldehyde in 0.1 M Sorensen's Sodium-Potassium Phosphate Buffer, Electron Microscopy Sciences, and diluted in a 0.2 M solution of the same buffer) followed by rinsing with a Sorensen's buffer solution (0.2 M, pH 7.2, Electron Microscopy Sciences). The grids were then treated for 15 minutes with 3% bovine serum albumin (BSA) dissolved in Sorensen's buffer, followed by 30 to 2 min incubation with either the monospecific anti-OmcZ antibodies developed for this study (Pacific Immunology) or the previously described peptide-based rabbit-derived polyclonal antibodies against OmcZ (Inoue, Qian et al. 2010); for these primary antibody incubations the antibodies were diluted 1:50 in Sorensen's buffer containing 0.3% BSA.

Grids were then rinsed three times in Sorensen's buffer solution and incubated for 30 min to 1 hour with goat-derived polyclonal secondary antibodies conjugated to gold nanoparticles (6 or 12 nm Colloidal Gold AffiniPure Goat Anti-Rabbit IgG (H+L) (EM Grade), Jackson ImmunoResearch Laboratories, Inc.). Grids were then rinsed three times in Sorensen's buffer solution and negatively stained with 1% phosphotungstic acid (pH 6.8) for 15 to 30 s and subsequently air-dried. Finally, grids were examined using a JEOL JEM-1400 Plus transmission electron microscope operated at 80 kV. Immunogold samples imaged via AFM were prepared as above, except that samples were adsorbed to a mica substrate rather than TEM grids, and no negative staining solution was applied.

Bacteriorhodopsin (bR) preparation

bR from *Halobacterium salinarum* (Sigma Aldrich B0184, native sequence, lyophilized powder) was diluted to a stock concentration of ~ 150 µg/mL in 0.01% sodium azide (NaN₃). Adsorption buffer (20 µL, 150 mM KCl + 10 mM Tris/HCl at pH 7.4) was drop casted onto the gold surface and 20 µL of stock bR were added to the droplet. After ~ 30 minutes, the sample was rinsed with deionized water.

Lysozyme preparation

Lysozyme was purified from chicken egg white (Sigma Aldrich L7651) and dissolved in 10 mM potassium phosphate (KH₂PO₄) buffer at pH 7 (final concentration ~ 200 µg/mL). The lysozyme sample was prepared similar to the procedure described above for bR.

AFM of nanowires and other proteins

AFM experiments for height measurements were performed using soft cantilevers (AC240TSA-R3, Oxford Instrument Co.) with a nominal force constant of 2 N/m and resonance frequencies of 70 kHz. The free-air amplitude of the tip was calibrated with the Asylum Research software and the spring constant was captured by the thermal vibration method. Samples were imaged with a Cypher ES scanner using intermittent tapping (AC-air topography) mode. All nanowires height analyses and statistics were performed using Gwyddion and IGOR Pro software (WaveMetrics Inc.). To check protein quality for infrared nanospectroscopy, AFM was performed using cantilevers (Arrow-NCR, Nano Worlds) with a nominal force constant of 42 N/m and a resonance frequency of 285 kHz. Samples were imaged with an Icon AFM (Bruker) using intermittent tapping (AC-air topography) mode. Liquid AFM was performed using bio-lever mini tips (BL-AC40TS, Olympus) with resonance frequency of 25 kHz in liquid and nominal force of 0.1 N/m. AFM images were processed using the Gwyddion package.

7.6 Nanoelectrode design and fabrication

Electrodes made of gold separated by a non-conductive gap were designed using electron beam lithography. Interdigitated electrode devices were designed in Layout Editor, a computer-aided design program. The electrodes were patterned by electron-beam lithography on a sacrificial electron beam resist layer spin coated onto a 300 nm layer of insulating silicon dioxide (SiO_2) grown on a silicon wafer. The wafer was then developed in a solution of cooled isopropyl alcohol to remove the resist layer where the pattern was printed. A 30-nm-thick gold film was evaporated after a 5-nm-thick titanium adhesion layer on lithographically patterned wafer using an electron-beam evaporator (Denton Infinity 22). The electron beam resist was removed with N-Methyl-2-

pyrrolidone by incubating for 15-20 min at 80 °C until the lift-off was complete. The device was then rinsed sequentially with acetone, methanol, and isopropanol before being dried with nitrogen, resulting in gold nanoelectrodes with a non-conductive gap. All device fabrication was performed in a class 1000 cleanroom to avoid contamination. The devices were further inspected with optical and scanning electron microscopy to ensure that the electrodes are well separated by a non-conductive gap, and resistance measurements were used to confirm that the electrodes are well insulated from each other ($R_{\text{gap}} > 1 \text{ T}\Omega$). Before usage, the device was washed with distilled water and then rinsed with isopropanol to remove contaminants on the surface. The device was further cleaned for 1 min with oxygen plasma and dried with nitrogen flow.

7.7 IR *s*-SNOM on individual proteins

As described previously (Yalcin, Legg et al. 2020), we used IR radiation from a wavelength-tunable quantum cascade laser (Daylight Solutions MIRcat Amide QCL tunable from 1450-1700 cm^{-1} with a bandwidth $< 1 \text{ cm}^{-1}$ and spectral resolution of 0.25 cm^{-1}) to illuminate a conductive AFM tip with $< 20 \text{ nm}$ spatial resolution. We incorporated this IR-coupled AFM to one arm of a Michelson interferometer and focused the IR laser to the AFM tip apex with a parabolic mirror (Numerical Aperture=0.25 and Power $< 10 \text{ mW}$). We used conductive PtSi (PtSi-NCH, Nanosensors) with a tip radius of $\sim 20 \text{ nm}$ operating in tapping mode (resonance frequency $\omega_t \sim 330 \text{ kHz}$). We operated the interferometer in 2-phase homodyne mode for IR *s*-SNOM (Berweger, Nguyen et al. 2013) to isolate and amplify the near-field, tip-scattered signal from the far-field background. We tuned the laser from 1600 cm^{-1} to 1700 cm^{-1} in 5 cm^{-1} steps and recorded images at each wavenumber to obtain the amide I spectra using IR *s*-SNOM. IR *s*-SNOM

phases describe absorption properties. For background subtraction, we obtained the phases from the sequential images from the empty region on the gold substrate (Berweger, Nguyen et al. 2013).

The tip-scattered IR radiation was recombined with the reference field for 2-phase (Φ_1 and Φ_2 in **Figure 3.9a**) homodyne amplification and detection with a HgCdTe detector (Kolmar Technologies). Far-field background was suppressed by demodulating the detected signal with lock-in amplifier (Zurich Instruments, HF2LI) at third harmonic of the cantilever oscillation frequency ($3\omega_r$) except for bR that used $3\omega_r + \Omega_r$ where Ω_r is the frequency of the chopper used in the reference arm (Berweger, Nguyen et al. 2013). This modulation scheme isolated the near-field signal and provided the background-free near-field amplitude $|A|$ and phase ϕ , which related to the complex-valued dielectric function of the amide I resonance. Extracted near-field phase and amplitude signals were used to access the absorptive properties of imaged proteins. Raster scanned s-SNOM images were acquired with a lock-in time constant of 10 ms/pixel that yielded good near-field signal contrast and avoided sample drift. The signal from the gold was at least 10 times lower than intrinsic protein signal, ensuring a high signal-to-noise ratio to extract the protein structure. All IR s-SNOM analyses and statistics were performed using Gwyddion software.

To extract near-field phase (absorption) properties of proteins, we used a two-phase homodyne detection technique by changing the reference arm between two orthogonal known phase components such as $\Phi_1 = \Phi_2 + \pi/2$ and extracted near-field amplitude and phase signal using following relations (Berweger, Nguyen et al. 2013):

$$I_1 = A \cos (\Phi - \Phi_1), \text{ using } \Phi_1 = \Phi_2 + \pi/2$$

$$I_2 = A \cos (\Phi - \Phi_2) = A \sin (\Phi - \Phi_1)$$

$$\text{Near-Field Phase: } \Phi_{\text{NF}} = \arctan (I_1/I_2)$$

$$\text{Near-Field Amplitude: } A_{\text{NF}} = (I_1^2 + I_2^2)^{1/2}$$

Nanoscale infrared spectroscopy studies have demonstrated sensitivity to detect beta sheets in a wide range of proteins such as insulin (Amenabar, Poly et al. 2013), tobacco mosaic virus (Amenabar, Poly et al. 2013), silk (Qin, Zhang et al. 2016), β_2 -microglobulin (Paulite, Fakhraai et al. 2011), diphenylalanine (Ramer, Ruggeri et al. 2018), Josephin domain of ataxin-3 amyloid (Ruggeri, Longo et al. 2015) and Huntingtin protein (Ruggeri, Vieweg et al. 2016).

7.7.1 Deconvolution and peak fitting of amide I spectra for IR *s*-SNOM and bulk FTIR

Band decomposition analysis was performed using a multi-peak fitting analysis program (IGOR Pro, Wavemetrics Inc.). IR *s*-SNOM spectra were evaluated with Lorentzian line shapes (Berweger, Nguyen et al. 2013) and bulk FTIR spectra were evaluated with Gaussian line shapes (Yang, Yang et al. 2015). For IR *s*-SNOM of nanowires, bR, and lysozyme, data are represented with red markers. Fitting results (blue curves) were obtained by applying band-decomposition analysis to the data, which yielded good agreement ($\chi^2 < 0.02$). Areas under the curve were integrated to estimate the percentages of α -helix, β -sheet, and coil components. In amide I mode, α -helices give rise to main absorption band located at 1660 cm^{-1} . β -sheets show a stronger band at 1625 cm^{-1} and a weaker band near 1685 cm^{-1} , $\sim 60 \text{ cm}^{-1}$ away from the stronger band (Barth 2007). This observed splitting in the β -sheet formation arises due to the transition dipole coupling mechanism (Barth 2007). The formation of β -sheets in IR *s*-SNOM spectra for

OmcS and OmcZ nanowires was evident from the presence of these two β -sheet bands(Barth 2007). All analyses were performed using IGOR Pro software (WaveMetrics Inc.).

7.8 Conducting-probe atomic force microscopy (CP-AFM) measurements

To measure the conductivity of nanowires using CP-AFM, 5 μ L of ethanolamine buffer solution containing nanowires were deposited on gold electrodes patterned with electron-beam lithography on a silicon wafer grown with 300 nm silicon dioxide as described above. The excess buffer was absorbed with filter paper. After air-drying, the sample was mounted on a metal puck and transferred to the sample stage inside the AFM (Oxford Instrument Co., Cypher ES). AFM and subsequent CP-AFM experiments were performed using soft cantilevers (ASYELEC-01, Oxford Instrument Co.) with a nominal force constant of 2 N/m and resonance frequencies of 70 KHz. The tip was coated with Pt/Ir. The free-air amplitude of the tip was calibrated with the Asylum Research software and the spring constant was captured by the thermal vibration method. For CP-AFM experiments, the dual gain ORCA holder was used (Asylum Research) to record both low and high current values. The sample was imaged with a Cypher ES scanner using intermittent tapping (AC-air topography) mode. AFM showed that gold electrodes were partially covered with nanowires to facilitate CP-AFM measurements. After identifying OmcZ nanowires across the electrodes and the substrate, the tip was withdrawn and brought into contact with the nanowires by switching on the contact mode. Points along the length of the nanowires were selected based on the AFM image and the corresponding distance was measured with Asylum Research Software that is used to

operate AFM. With partially gold-coated substrate as the first electrode and a metal-coated AFM tip as a second mobile electrode, the uncovered parts of the nanowires were electrically contacted, measuring the I - V characteristics as a function of the distance between the tip and the electrode by applying a bias ramp in the range - 0.2 V to + 0.2 V, and then the tip was withdrawn to the next point. To verify proper electrical contact during the measurements, the tip was frequently brought into contact with either gold or SiO₂ substrate. A loading force of 50 nN was used to obtain stable current and the same force was used for all experiments reported in this manuscript. The I - V characteristics were captured in the software and the analysis was performed in IGOR Pro software (WaveMetrics Inc.). I - V curves were processed using 75 points Savitzky-Golay smoothing function prior to fitting using IGOR Pro software (WaveMetrics Inc.). The linear regime of the I - V characteristics was used for calculation of resistance using the equation: $R=V/I$. The resistance from different points was then plotted as a function of distance (L). For each distance, at least 8 repeats were recorded and a minimum of three biological replicates were used to evaluate statistical significance.

7.9 Conductivity calculations

The conductivity (σ) of nanowires (Fig. 3d, 5b) was calculated using the relation $\sigma = G \cdot (L/A)$ where G is the conductance which is reciprocal of resistance R , L is the length of the nanowire, and $A = \pi r^2$ is the area of cross section of the nanowire with $2r$ as the height of the nanowire measured using AFM, taking into account pH-induced reduction in diameter. Due to the extremely small (~ 3 nm) height of the nanowires, the small cross-sectional area of the nanowires gives rise to higher conductivity.

As our W51W57 cell growth and filament preparation conditions were similar to previous studies (Tan, Adhikari et al. 2016), our results suggest that the nanowires reported to be tryptophan-substituted pili (Tan, Adhikari et al. 2016) are OmcZ nanowires and hence were used for conductivity comparison with OmcS.

7.10 Stiffness measurements

The OmcS and OmcZ nanowires were prepared for stiffness measurements in a manner similar to AFM sample preparation described earlier. Samples were imaged with a Cypher ES scanner using amplitude-modulation (AM)-frequency modulation (FM) bimodal imaging mode using Arrow UHFAuD (Nanoworld) cantilever with 6 N/m nominal force constant (k_1). The spring constant for both the first and second eigenmodes (k_1 and k_2) and the quality factor (Q) of the tip was calibrated by fitting the thermal vibration curves before the experiment. To operate in bimodal AM-FM imaging mode, the tip was tuned on both eigenmodes prior to tip sample interaction. Tuning of the cantilever was modulated with the blue drive aligned to the base of the cantilever to produce maximum driving power. The first cantilever eigenmode was excited to the resonant frequency ($f_1 \sim 2$ MHz) and tuned with the AFM software (Asylum Research) and the second eigenmode was excited to the second order resonant frequency ($f_2 \sim 7$ MHz) at least ~ 100 times lower in amplitude than the first eigenmode.

Upon approaching the sample, the tip was final tuned to compensate for the shift in drive frequency induced by tip-sample interaction. Repulsive imaging mode was used (phase $< 90^\circ$) to overcome adhesion force. Drive amplitude was adjusted to maintain a small indentation depth (~ 300 pm) and the maximum indentation depth δ was monitored

from the imaging feedback loop using the following relation: $\delta =$

$$\frac{3}{4} \left(\frac{k_1}{Q_1} A_{1,free} \cos \phi_1 \right) \left(\frac{2k_2 \Delta f_2}{f_2} \right)^{-1}$$

where $A_{1,free}$ is the free amplitude tuned for the first eigenmode, ϕ_1 is the phase response of the first eigenmode, and Δf_2 is the frequency shift monitored from the second eigenmode. The effective storage modulus of the interaction E_{eff} was calculated from the following equation using a Hertz punch model (Kocun, Labuda et al. 2017): $E_{eff} =$

$$\frac{\pi}{R} \sqrt{\frac{1}{6}} \left(\frac{k_1 A_{1,free}}{Q_1 A_{1,set}} \cos \phi_1 \right)^{-\frac{1}{2}} \left(\frac{2k_2 \Delta f_2}{f_2} \right)^{\frac{3}{2}}$$

where $A_{1,set}$ is the setpoint used for imaging and R (~ 7 nm) is the tip radius provided by the manufacturer. Correlated topography and Young's modulus images were generated with a resolution of 512 x 512 pixels. The mean value of the nanowire modulus was extracted by fitting a Gaussian function to the histograms created from the modulus map of three biological replicates. The same tip and imaging configuration were used for all samples to maintain consistency between measurements.

7.11 Grazing-incidence X-ray microdiffraction (GI μ XRD)

To visualize the stacking of hemes in nanowires and to investigate the effect of pH on the stacking, GI μ XRD data were collected in grazing incidence mode using a Rigaku D/Max Rapid II instrument equipped with a 2D image plate detector. The Aro5 strain was used to focus on OmcS nanowires whereas W51W57 strain was used to probe OmcZ nanowires. X-rays were generated by a MicroMax 007HF generator fitted with a rotating chromium anode ($\lambda = 2.2897$ Å) that was focused on the specimen through a 300 μ m diameter collimator. The instrument's correct sample-to-detector distance was verified by

measuring the lattice constant of a LaB₆ standard (NIST 660c). All nanowire samples were prepared using a centrifugation method without salts for precipitation (Malvankar, Vargas et al. 2011), such as ammonium sulphate, to eliminate background peaks. Samples were then dialyzed in 150 mM ethanolamine buffer at pH 10.5 and 20 μ L solutions containing nanowire samples were dropped from a micropipette onto glass substrates. To ensure data reproducibility, the experiments were repeated at multiple spots that yielded similar results. At least three different surface spots were scanned at a fixed 1° incident angle with no sample rotation in the sample plane. These multiple measurements yielded similar results. To further investigate the pH effect on the stacking, the pH of nanowire sample was changed by applying ethanolamine buffer at pH 7 and pH 2. The background was subtracted using smoothing procedure used for XRD data (Bruckner 2000) and the data was plotted using IGOR Pro (WaveMetrics Inc.). Rigaku's 2D Data Processing Software (Ver. 1.0, Rigaku, 2007) was used to integrate the diffraction rings captured by the detector. Peak fitting to determine *d*-spacings was carried out using JADE 9.5.1 (Materials Data, Inc.) with the Pseudo-Voigt peak profile function.

7.12 FTIR

We used the Agilent Cary 660 FTIR with a Pike Technologies GladiATR™ single reflection attenuated total reflection geometry with a diamond crystal. All FTIR spectra were collected with spectral resolution of 4 cm⁻¹. Final spectra represent an average of 144 individual spectra and are plotted as absorbance versus a background of air. Samples were prepared on a silicon wafer and the reference spectrum of 10 mM KPO₄ was subtracted from the nanowire spectra. An ATR correction and boxcar smoothing were

applied using Agilent software. Measurements on air-dried films were compared to samples fully hydrated in D₂O, which eliminates the strong H₂O IR absorption in the amide I band; these measurements were found to be equivalent.

7.13 Raman spectroscopy

Raman spectroscopy was performed using a 532 nm-green solid-state diode laser (continuous wave, power ~ 57 mW) with a synapse-cooled CCD detector, 600 grating/mm, and 50X objective (Horiba-Labram HR Evolution). Nanowires prepared in ethanolamine buffer were drop-casted on a silicon wafer. Data were collected with an accumulation time of 10 s, averaged over 80 iterations. A minimum of three different locations were measured on each sample. All experiments were repeated on multiple samples that yielded similar results. The instrument was calibrated using the silicon wafer as standard. Data were analyzed with IGOR Pro software (WaveMetrics Inc.).

7.14 CD spectroscopy

CD spectra and subsequent analysis with CDPro were conducted to estimate the secondary structure fractions of OmcZ and OmcS nanowires. Samples were initially dialyzed in 10 mM KH₂PO₄ buffer at pH 7; the protein concentration was determined via the standard bicinchoninic acid assay. CD scans of nanowire samples and buffer background (five replicates) were collected between 190 nm and 260 nm with a 10- or 2-mm-pathlength quartz cuvette using a spectrometer (Chirascan, Applied Photophysics). Using the Pro-Data Chirascan software (Applied Photophysics), all replicate spectra were averaged, the averaged buffer background spectrum was subtracted from all averaged nanowire spectra. Experiments examining the excitonic coupling of nanowires collected

spectra from 300 nm to 480 nm. The following formula (Greenfield 2006) was used to convert raw ellipticity values (mdeg; millidegrees) to molar ellipticity values ($[\theta]$; deg $\text{cm}^2 / \text{dmol}$) for secondary structure quantification:

$$[\theta] = \frac{mdeg \cdot MW}{l \cdot C}$$

where MW is the mean residue weight, l is the pathlength in centimetres, and C is the concentration in mg/ml. Nanowire spectra in molar ellipticity values were entered into the CDPro software using the CDSSTR method (Sreerama and Woody 2000). Solid-state CD experiments were performed similar to solution experiment except the solid sample holder (Chirascan, Applied Photophysics) was used and the film was prepared in manner similar to FTIR experiments.

7.15 Fluorescence microscopy of nanowires

A 600 μM Thioflavin T (ThT) stock solution was used to bring nanowire solutions to a final concentration of 100 μM ThT. Samples were incubated for 1 hour at room temperature before depositing 10 μl of solution on cleaned microscope slides and coverslips. Microscope slides (Fisherfinest Premium Catalogue No. 12-544-1) and coverslips were sonicated for 20 minutes each in 1 M KOH, Milli-Q water, and finally 70% ethanol before they were air-dried with nitrogen. Control samples that had only ThT or only nanowires did not show any fluorescent fibril structures, confirming that the observed fluorescence is due to ThT binding to nanowires. Samples were excited with a 445-nm CW laser (Agilent Technologies MLC 400B) used at 30% of maximum power (<10 mW). TIRF microscopy images were acquired on an Eclipse TiE microscope

(Nikon) equipped with an Andor iXonEM+ DU-897 camera. All images were processed and analyzed using ImageJ software.

Thioflavin T (ThT) was obtained from Sigma-Aldrich; 600 μM stock solutions were prepared by diluting ThT in 10 mM KPO_4 at pH 7, passing the solution through a 0.2 μm filter to remove dye aggregates, and verifying the final ThT concentration with UV-vis spectroscopy and the ThT extinction coefficient of ($36,000 \text{ M}^{-1} \text{ cm}^{-1}$) at 412 nm. Nanowire samples were diluted at a 1:1 ratio (v/v) with a solution of 100 μM ThT and incubated at room temperature for 1 hour before acquiring spectra with a Fluoromax-4 spectrofluorometer (Horiba Jobin Yvon) in an ultra-micro fluorescence cuvette with an optical path length of 10 mm (PerkinElmer Part No. B0631124). The excitation wavelength was set to 440 nm and emission was recorded at 465-600 nm with 5 nm excitation and emission slit widths.

7.16 Molecular Dynamics

We performed molecular dynamics (MD) simulations to sample the orientation of the imidazole rings of the histidine residues coordinating the heme iron atoms. We obtained the starting coordinates from the OmcS nanowire structure (PDB ID: 6EF8)(Wang, Gu et al. 2019) and built a dimer model of OmcS, composed of two consecutive protomers from 6EF8. We modelled the hemes in their deprotonated state and all ionizable protein residues were protonated according to their pKa values. The hemes were modeled in an oxidized state using previously computed partial charges (Barrozo, El-Naggar et al. 2018) for the heme atoms and covalently bound histidine and cysteine residues.

The MD simulation were performed using NAMD program (Phillips, Braun et al. 2005) with the CHARMM36 (Best, Zhu et al. 2012) force field parameters. The force field parameters for the hemes were obtained from reference 4 (Autenrieth, Tajkhorshid et al. 2004). We minimized the system followed by a 2.5 ns relaxation of the solvation water box. The model was equilibrated to 310 K in the NVT ensemble for 3.5 ns under harmonic restraints with a force constant of 0.1 kcal/mol to the amino acid sidechains and a force constant of 1.0 kcal/mol to the protein backbone and the hemes. A production run was then performed in an NPT ensemble for 20 ns with frames being written to the trajectory every 2.5 ps. The RMSD of the system was observed to converge within the first 10 ns of the simulation.

The orientation of the imidazole rings was extracted from a set of 1000 equally spaced snapshots (10 ps spacing) using a custom Tcl script. The angle between imidazole rings was determined by computing the angle between the two planes of the imidazole rings with defining basis vectors using the $N_{\epsilon} - C_{\delta}$ and $N_{\epsilon} - C_{\epsilon}$ bonds following translation of the N_{ϵ} atoms to the origin. The angle between the planes is computed via computation of the angle formed by the normal vectors of the two planes.

7.17 EPR Spectroscopy

The EPR samples at different pH conditions were prepared with ~200 μ M OmcS filament preparations: 1) 150 mM ethanolamine (ETA) in pH 10.5; 2) 50 mM Tris-HCl, 150 mM NaCl buffer in pH 7 or 150 mM ethanolamine (ETA) in pH 7; and 3) 150 mM ETA in pH 2. The samples were transferred into 4 mm o.d. quartz tubes and kept anaerobic under nitrogen atmosphere before cooling in liquid nitrogen. The continuous wave X-band (9-10 GHz) EPR measurements were collected using Bruker ELEXSYS

E500 EPR spectrometer equipped with a SHQ resonator and an Oxford ESR-900 continuous flow cryostat at 8-9 K. The EPR spectra were recorded using following EPR parameters: microwave frequency, 9.38 GHz; modulation frequency of 100 kHz; modulation amplitude of 10 G; microwave power of 2 mW; sweep time, 84-210 sec; time constant, 41 msec. Each spectrum was the average of 2 to 5 scans.

7.17.1 EPR Analysis

We used the ligand-field correlation analysis, based on the formalism introduced by Griffith (Griffith 1971) and developed by Taylor (Taylor 1977) to find the rhombic (V/λ) and axial (Δ/λ) crystal field parameters. The corresponding V/Δ ratio was applied for determination of system rhombicity and analysis of hemes coordination (Turner, Brennan et al. 2000, Ponomarenko, Niklas et al. 2018). A previously described model *G. sulfurreducens* multi-heme cytochromes (Ponomarenko, Niklas et al. 2018) for the heme molecular orbitals characterization and correlation of empirical g-value to the axial ligand geometry was used in this study. Data processing was performed using Igor Pro 7 (WaveMetrics, Inc., Lake Oswego, Oregon). Simulations, deconvolution analysis, and least square fitting were performed using the EasySpin software package (version 5.2.24). Further adjustment in assignments of g-tensor principal values were based on the complete EPR spectrum simulations. For simulation, the g_y and g_x parameters of high g_{\max} low-spin signals were estimated based on the normalization requirement (Griffith 1971, Taylor 1977) $g_z^2 + g_y^2 + g_x^2 = 16$.

7.18 X-ray absorption spectroscopy

The Fe K-edge X-ray absorption spectra of the OmcS nanowires at different pH were measured on solution samples in fluorescence mode. Internal energy calibration was accomplished by simultaneous measurement of the absorption of a Fe foil placed between two ionization chambers situated after the sample. pH 2 data were obtained at the National Synchrotron Light Source-2 (NSLS-2) on QAS (7-BM) beamline and pH 10.5 data were recorded at APS synchrotron on beamline 12-BM. Data processing and analysis were performed in Athena and Artemis (Ravel and Newville 2005). pH 2 Fe K-edge XAS trace was smoothed to reduce statistical noise in the data using IGOR Pro (WaveMetrics Inc.). EXAFS fittings were performed using theoretical Fe-N paths obtained from the Fe₂N model. The fits were performed in r-space, using k²-weighing. A narrower k-range was used for pH 2 data (1.8 to 7 Å⁻¹) compared to pH 10.5 (1.8 to 9 Å⁻¹) due to the higher noise level in the pH 2 data. The r-ranges were from 1 to 2.279 Å in the both data sets. The amplitude factor was set at 0.75 when performing EXAFS data best fit analysis of both pH 2 and 10.5 OmcS samples, as obtained independently by the analysis of Fe reference spectra.

7.19 UV-Vis spectroscopy

UV-Vis experiments were performed either in a solution or solid-state configuration with an integration sphere using an ultra-low stray light fiber optic spectrometer (Avantes). Band decomposition analysis was performed using a multi-peak fitting analysis program (IGOR Pro, Wavemetrics Inc.).

7.20 UV-vis Spectral Simulations

The *c*-type heme cofactors of OmcS were modelled as iron porphins, with the methyl, thioether, and propionic acid substituents of the macrocycle replaced by hydrogen atoms. The two axially coordinated histidine residues were truncated at the C_β - C_γ bond to give imidazole ligands. This model system has been extensively used in the past because it provides an appropriate balance between accuracy and computational efficiency to study the properties of the heme group (Reghu, Väkiparta et al. 1994, Smith, Dupuis et al. 2003, Lee, Parameswaran et al. 2008, Ali, Sanyal et al. 2012, Radon 2014). The number and type of axial ligands were varied, as described below, to compare with the pH-induced spectroscopic changes observed experimentally.

7.21 Spectroelectrochemistry Experiments

OmcS nanowire samples were dialyzed into pH 7.0 50 mM KPO₄ with 100 mM KCl as the spectroelectrochemistry buffer. A mediator soup containing phenazine methosulfate, phenazine ethosulfate, gallocyanine, methylene blue, indigo tetrasulfonate, indigo trisulfonate, indigo disulfonate, 2-hydroxy-1,4-naphthoquinone, anthraquinone-2, 6-disulfonate, anthraquinone-2-sulfonate, safranin 0, neutral red, benzyl viologen, diquat and methyl viologen that cover a range of potentials from -440 mV to +80 mV was added from stock solutions for a final concentration of ~1.5 μM, similar to prior studies (Inoue, Qian et al. 2010). An Avantes fiber-optic spectrometer was used to collect UV-vis spectra, while a Pine research honeycomb spectroelectrochemistry kit was used as the working and counter electrode, which were both made of gold. An Ag/AgCl reference electrode was tested with quinhydrone solutions at pH 7 and pH 4 prior to and after each

experiment to account for drift, and its performance was also checked before each experiment by comparison to a fresh reference electrode. The pH of the sample was measured after each experiment to ensure no changes were present as well. The experiments were completed at 25 °C. A Gamry potentiostat was used to control the potentials in chronoamperometry mode, and I waited at least two minutes for the capacitive current to flatten out before collecting UV-vis data corresponding to that potential. The results of collecting spectra at two minutes and at three minutes was compared and the differences were negligible. Nevertheless, data after waiting three minutes were used to calculate the apparent midpoint reduction potential. The reduced fractions were calculated by integrating the area between two isosbestic points in the Q-band of the OmcS nanowire UV-Vis, specifically from BLANK and BLANK. These values were normalized relative to fully reduced and fully oxidized spectra and the potentials converted to versus SHE values following methods presented in (Qian, Mester et al. 2011). In a similar manner to (Qian, Mester et al. 2011) the reduced fraction data were fit to a model for 6 independent Nernstian redox electron transfers to determine the potentials presented in **Table 2**.

The monomer/denatured OmcS control sample was prepared by heating the sample at 80 °C for 10 minutes, and then was allowed to cool to room temperature before adding in the mediator soup. The same experimental procedure was followed as for the OmcS nanowires to ensure a consistent comparison.

8 References

- Adhikari, R., N. Malvankar, M. Tuominen and D. Lovley (2016). "Conductivity of individual *Geobacter pili*." RSC Advances **6**: 8354 - 8357.
- Afkar, E., G. Reguera, M. Schiffer and D. R. Lovley (2005). "A novel *Geobacteraceae*-specific outer membrane protein J (OmpJ) is essential for electron transport to Fe(III) and Mn(IV) oxides in *Geobacter sulfurreducens*." BMC Microbiol **5**: 41.
- Akiyama, K., M. Fukuda, N. Kobayashi, A. Matsuoka and K. Shikama (1994). "The pH-dependent swinging-out of the distal histidine residue in ferric hemoglobin of a midge larva (*Tokunagayusurika akamusi*)." Biochimica et Biophysica Acta (BBA) - Protein Structure and Molecular Enzymology **1208**(2): 306-309.
- Ali, M. E., B. Sanyal and P. M. Oppeneer (2012). "Electronic structure, spin-states, and spin-crossover reaction of heme-related Fe-porphyrins: a theoretical perspective." J Phys Chem B **116**(20): 5849-5859.
- Amenabar, I., S. Poly, W. Nuansing, E. H. Hubrich, A. A. Govyadinov, F. Huth, R. Krutokhvostov, L. Zhang, M. Knez, J. Heberle, A. M. Bittner and R. Hillenbrand (2013). "Structural analysis and mapping of individual protein complexes by infrared nanospectroscopy." Nature Communications **4**: 2890.
- Andersson, K. K., J. D. Lipscomb, M. Valentine, E. Münck and A. B. Hooper (1986). "Tetraheme cytochrome c-554 from *Nitrosomonas europaea*: Heme-heme interactions and ligand binding." Journal of Biological Chemistry **261**(3): 1126-1138.
- Ashkenazy, H., S. Abadi, E. Martz, O. Chay, I. Mayrose, T. Pupko and N. Ben-Tal (2016). "ConSurf 2016: an improved methodology to estimate and visualize evolutionary conservation in macromolecules." Nucleic Acids Res **44**(W1): W344-350.
- Autenrieth, F., E. Tajkhorshid, J. Baudry and Z. Luthey-Schulten (2004). "Classical force field parameters for the heme prosthetic group of cytochrome c." Journal of Computational Chemistry **25**(13): 1613-1622.
- Barrozo, A., M. Y. El-Naggar and A. I. Krylov (2018). "Distinct electron conductance regimes in bacterial decaheme cytochromes." Angewandte Chemie International Edition **57**(23): 6805-6809.
- Barth, A. (2007). "Infrared spectroscopy of proteins." Biochimica et Biophysica Acta (BBA) - Bioenergetics **1767**(9): 1073-1101.
- Bertini, I., G. Cavallaro and A. Rosato (2006). "Cytochrome c: occurrence and functions." Chem Rev **106**(1): 90-115.
- Berweger, S., D. M. Nguyen, E. A. Muller, H. A. Bechtel, T. T. Perkins and M. B. Raschke (2013). "Nano-chemical infrared imaging of membrane proteins in lipid bilayers." Journal of the American Chemical Society **135**(49): 18292-18295.

- Best, R. B., X. Zhu, J. Shim, P. E. M. Lopes, J. Mittal, M. Feig and A. D. MacKerell (2012). "Optimization of the additive CHARMM all-atom protein force field targeting improved sampling of the backbone ϕ , ψ and side-chain χ_1 and χ_2 dihedral angles." Journal of Chemical Theory and Computation **8**(9): 3257-3273.
- Beyenal, H. and J. T. Babauta (2015). *Biofilms in bioelectrochemical systems : from laboratory practice to data interpretation*. Hoboken, Wiley, : 1 online resource.
- Blumberg, W. and J. Peisach (1971). Low—Spin Compounds of Heme Proteins. Bioinorganic Chemistry - Advances in chemistry series. . R. Dessy, J. Dillard and L. Taylor, ACS Publications: 271-291.
- Blumberg, W. and J. Peisach (1971). Low—Spin Compounds of Heme Proteins. Bioinorganic Chemistry - Advances in chemistry series. R. Dessy, J. Dillard and L. Taylor, ACS Publications: 271-291.
- Boyken, S. E., M. A. Benhaim, F. Busch, M. Jia, M. J. Bick, H. Choi, J. C. Klima, Z. Chen, C. Walkey and A. Mileant (2019). "De novo design of tunable, pH-driven conformational changes." Science **364**(6441): 658-664.
- Bruckner, S. (2000). "Estimation of the background in powder diffraction patterns through a robust smoothing procedure." Journal of Applied Crystallography **33**(3 Part 2): 977-979.
- Cerpa, R., F. E. Cohen and I. D. Kuntz (1996). "Conformational switching in designed peptides: the helix/sheet transition." Folding and Design **1**(2): 91-101.
- Chadwick, G. L., F. Jimenez Otero, J. A. Gralnick, D. R. Bond and V. J. Orphan (2019). "NanoSIMS imaging reveals metabolic stratification within current-producing biofilms." Proc Natl Acad Sci U S A **116**(41): 20716-20724.
- Childers, S. E., S. Ciuffo and D. R. Lovley (2002). "Geobacter metallireducens accesses insoluble Fe(III) oxide by chemotaxis." Nature **416**(6882): 767-769.
- Clarke, T. A., M. J. Edwards, A. J. Gates, A. Hall, G. F. White, J. Bradley, C. L. Reardon, L. Shi, A. S. Beliaev, M. J. Marshall, Z. Wang, N. J. Watmough, J. K. Fredrickson, J. M. Zachara, J. N. Butt and D. J. Richardson (2011). "Structure of a bacterial cell surface decaheme electron conduit." Proc Natl Acad Sci U S A **108**(23): 9384-9389.
- Coppi, M. V., C. Leang, S. J. Sandler and D. R. Lovley (2001). "Development of a genetic system for Geobacter sulfurreducens." Appl Environ Microbiol **67**(7): 3180-3187.
- Cote, Y., I. W. Fu, E. T. Dobson, J. E. Goldberger, H. D. Nguyen and J. K. Shen (2014). "Mechanism of the pH-controlled self-assembly of nanofibers from peptide amphiphiles." The Journal of Physical Chemistry C **118**(29): 16272-16278.
- D'Angelo, P., A. Lapi, V. Migliorati, A. Arcovito, M. Benfatto, O. M. Roscioni, W. Meyer-Klaucke and S. Della-Longa (2008). "X-ray Absorption Spectroscopy of Hemes and Hemeproteins in Solution: Multiple Scattering Analysis." Inorganic Chemistry **47**(21): 9905-9918.

- Dai, Z. and E. M. Boon (2011). "Probing the local electronic and geometric properties of the heme iron center in a H-NOX domain." Journal of inorganic biochemistry **105**(6): 784-792.
- Della Longa, S., S. Pin, R. Cortes, A. V. Soldatov and B. Alpert (1998). "Fe-heme conformations in ferric myoglobin." Biophys J **75**(6): 3154-3162.
- Dolla, A., L. Blanchard, F. Guerlesquin and M. Bruschi (1994). "The protein moiety modulates the redox potential in cytochromes c." Biochimie **76**(6): 471-479.
- Donhauser, Z. J., B. A. Mantooth, K. F. Kelly, L. A. Bumm, J. D. Monnell, J. J. Stapleton, D. W. Price, A. M. Rawlett, D. L. Allara, J. M. Tour and P. S. Weiss (2001). "Conductance switching in single molecules through conformational changes." Science **292**(5525): 2303-2307.
- Durchschlag, H. and P. Zipper (2004). "Modeling the hydration of proteins at different pH values." Analytical Ultracentrifugation VII **127**: 98-112.
- Egelman, E. H. (2000). "A robust algorithm for the reconstruction of helical filaments using single-particle methods." Ultramicroscopy **85**(4): 225-234.
- Esquerra, R. M., R. A. Jensen, S. Bhaskaran, M. L. Pillsbury, J. L. Mendoza, B. W. Lintner, D. S. Kliger and R. A. Goldbeck (2008). "The pH dependence of heme pocket hydration and ligand rebinding kinetics in photodissociated carbonmonoxymyoglobin." Journal of Biological Chemistry **283**(20): 14165-14175.
- Fonseca, B. M., C. M. Paquete, C. A. Salgueiro and R. O. Louro (2012). "The role of intramolecular interactions in the functional control of multiheme cytochromes c." FEBS Lett **586**(5): 504-509.
- Freund, J., J. Halbritter and J. Hörber (1999). "How dry are dried samples? Water adsorption measured by STM." Microscopy research and technique **44**(5): 327-338.
- Fry, H. C., A. R. Wood and L. A. Solomon (2017). "Supramolecular control of heme binding and electronic states in multi-heme peptide assemblies." Organic & biomolecular chemistry **15**(32): 6725-6730.
- Greenfield, N. J. (2006). "Using circular dichroism spectra to estimate protein secondary structure." Nature Protocols **1**(6): 2876-2890.
- Griffith, J. (1971). "Theory of EPR in low-spin ferric haemoproteins." Molecular Physics **21**(1): 135-139.
- Grossmann, J., B. Roschitzki, C. Panse, C. Fortes, S. Barkow-Oesterreicher, D. Rutishauser and R. Schlapbach (2010). "Implementation and evaluation of relative and absolute quantification in shotgun proteomics with label-free methods." Journal of proteomics **73**(9): 1740-1746.
- Guterman, T., M. Kornreich, A. Stern, L. Adler-Abramovich, D. Porath, R. Beck, L. J. W. Shimon and E. Gazit (2016). "Formation of bacterial pilus-like nanofibres by designed minimalistic self-assembling peptides." Nature Communications **7**: 13482.

- Hager, A. J., D. L. Bolton, M. R. Pelletier, M. J. Brittnacher, L. A. Gallagher, R. Kaul, S. J. Skerrett, S. I. Miller and T. Guina (2006). "Type IV pili-mediated secretion modulates *Francisella* virulence." Mol Microbiol **62**(1): 227-237.
- Haldar, S., P. Sil, M. Thangamuniyandi and K. Chattopadhyay (2015). "Conversion of Amyloid Fibrils of Cytochrome c to Mature Nanorods through a Honeycomb Morphology." Langmuir **31**(14): 4213-4223.
- Hayashi, T., M. Tinzl, T. Mori, U. Krengel, J. Proppe, J. Soetbeer, D. Klose, G. Jeschke, M. Reiher and D. Hilvert (2018). "Capture and characterization of a reactive haem-carbenoid complex in an artificial metalloenzyme." Nature Catalysis **1**(8): 578-584.
- Hirota, S., Y. Hattori, S. Nagao, M. Taketa, H. Komori, H. Kamikubo, Z. Wang, I. Takahashi, S. Negi, Y. Sugiura, M. Kataoka and Y. Higuchi (2010). "Cytochrome c polymerization by successive domain swapping at the C-terminal helix." Proc Natl Acad Sci U S A **107**(29): 12854-12859.
- Ho Choi, S., B. Kim and C. D. Frisbie (2008). "Electrical Resistance of Long Conjugated Molecular Wires." Science **320**(5882): 1482-1486.
- Holmes, D. E., S. K. Chaudhuri, K. P. Nevin, T. Mehta, B. A. Methe, A. Liu, J. E. Ward, T. L. Woodard, J. Webster and D. R. Lovley (2006). "Microarray and genetic analysis of electron transfer to electrodes in *Geobacter sulfurreducens*." Environ Microbiol **8**(10): 1805-1815.
- Ikezaki, A. and M. Nakamura (2002). "Models for cytochromes c: Spin states of mono (imidazole)-ligated (m-eso-tetramesitylporphyrinato) iron (iii) complexes as studied by UV-Vis, ¹³C NMR, ¹H NMR, and EPR spectroscopy." Inorganic chemistry **41**(24): 6225-6236.
- Inoue, K., C. Leang, A. E. Franks, T. L. Woodard, K. P. Nevin and D. R. Lovley (2010). "Specific localization of the c-type cytochrome OmcZ at the anode surface in current-producing biofilms of *Geobacter sulfurreducens*." Environmental Microbiology Reports **3**: 211-217.
- Inoue, K., X. Qian, L. Morgado, B. Kim, T. Mester, M. Izallalen, C. Salgueiro and D. Lovley (2010). "Purification and characterization of omcZ, an outer-surface, octaheme c-type cytochrome essential for optimal current production by *Geobacter sulfurreducens*." Applied and Environmental Microbiology **76**(12): 3999-4007.
- Janiak, C. (2000). "A critical account on π - π stacking in metal complexes with aromatic nitrogen-containing ligands." Journal of the Chemical Society, Dalton Transactions(21): 3885-3896.
- Jiang, X., Z. Futera, M. E. Ali, F. Gajdos, G. F. von Rudorff, A. Carof, M. Breuer and J. Blumberger (2017). "Cysteine Linkages Accelerate Electron Flow through Tetra-Heme Protein STC." J Am Chem Soc **139**(48): 17237-17240.
- Kleinfeld, O., A. Frenkel, J. M. Martin and I. Sagi (2003). "Active site electronic structure and dynamics during metalloenzyme catalysis." Nature structural biology **10**(2): 98-103.

- Kocun, M., A. Labuda, W. Meinhold, I. Revenko and R. Proksch (2017). "Fast, high resolution, and wide modulus range nanomechanical mapping with bimodal tapping mode." ACS Nano **11**(10): 10097-10105.
- Koga, T., K. Taguchi, Y. Kobuke, T. Kinoshita and M. Higuchi (2003). "Structural Regulation of a Peptide-Conjugated Graft Copolymer: A Simple Model for Amyloid Formation." Chemistry—A European Journal **9**(5): 1146-1156.
- Korshin, G. V., A. I. Frenkel and E. A. Stern (1998). "EXAFS Study of the Inner Shell Structure in Copper(II) Complexes with Humic Substances." Environmental Science & Technology **32**(18): 2699-2705.
- Kotloski, N. J. and J. A. Gralnick (2013). "Flavin electron shuttles dominate extracellular electron transfer by *Shewanella oneidensis*." mBio **4**(1).
- Krey, J. F., P. A. Wilmarth, J.-B. Shin, J. Klimek, N. E. Sherman, E. D. Jeffery, D. Choi, L. L. David and P. G. Barr-Gillespie (2013). "Accurate label-free protein quantitation with high-and low-resolution mass spectrometers." Journal of Proteome Research **13**(2): 1034-1044.
- Leang, C., N. S. Malvankar, A. E. Franks, K. P. Nevin and D. R. Lovley (2013). "Engineering *Geobacter sulfurreducens* to produce a highly cohesive conductive matrix with enhanced capacity for current production." Energy & Environmental Science **6**(6): 1901-1908.
- Leang, C., X. Qian, T. Mester and D. R. Lovley (2010). "Alignment of the c-type cytochrome OmcS along pili of *Geobacter sulfurreducens*." Appl Environ Microbiol **76**(12): 4080-4084.
- Lee, H. S., P. Parameswaran, A. Kato-Marcus, C. I. Torres and B. E. Rittmann (2008). "Evaluation of energy-conversion efficiencies in microbial fuel cells (MFCs) utilizing fermentable and non-fermentable substrates." Water Research **42**(6-7): 1501-1510.
- Lee, K., S. Cho, S. H. Park, A. J. Heeger, C. W. Lee and S. H. Lee (2006). "Metallic transport in polyaniline." Nature **441**(7089): 65-68.
- Levar, C. E., C. L. Hoffman, A. J. Dunshee, B. M. Toner and D. R. Bond (2017). "Redox potential as a master variable controlling pathways of metal reduction by *Geobacter sulfurreducens*." ISME J **11**(3): 741-752.
- Li, C., Z. Wang, Y. Lu, X. Liu and L. Wang (2017). "Conformation-based signal transfer and processing at the single-molecule level." Nature Nanotechnology **12**: 1071.
- Liu, J., S. Chakraborty, P. Hosseinzadeh, Y. Yu, S. Tian, I. Petrik, A. Bhagi and Y. Lu (2014). "Metalloproteins containing cytochrome, iron–sulfur, or copper redox centers." Chemical reviews **114**(8): 4366-4469.
- Liu, X., S. Zhuo, C. Rensing and S. Zhou (2018). "Syntrophic growth with direct interspecies electron transfer between pili-free *Geobacter* species." ISME J **12**(9): 2142-2151.
- Logan, B. E., B. Hamelers, R. Rozendal, U. Schroder, J. Keller, S. Freguia, P. Aelterman, W. Verstraete and K. Rabaey (2006). "Microbial fuel cells: methodology and technology." Environ Sci Technol **40**(17): 5181-5192.

- Logan, B. E. and K. Rabaey (2012). "Conversion of wastes into bioelectricity and chemicals by using microbial electrochemical technologies." Science **337**(6095): 686-690.
- Lovley, D. R. (2012). "Electromicrobiology." Annu Rev Microbiol **66**: 391-409.
- Lovley, D. R., D. E. Holmes and K. P. Nevin (2004). "Dissimilatory Fe(III) and Mn(IV) reduction." Adv Microb Physiol **49**: 219-286.
- Lovley, D. R. and K. P. Nevin (2013). "Electrobiocommodities: powering microbial production of fuels and commodity chemicals from carbon dioxide with electricity." Curr Opin Biotechnol **24**(3): 385-390.
- Mahadevan, R., D. R. Bond, J. E. Butler, A. Esteve-Nunez, M. V. Coppi, B. O. Palsson, C. H. Schilling and D. R. Lovley (2006). "Characterization of metabolism in the Fe(III)-reducing organism *Geobacter sulfurreducens* by constraint-based modeling." Appl Environ Microbiol **72**(2): 1558-1568.
- Malvankar, N. S., J. Lau, K. P. Nevin, A. E. Franks, M. T. Tuominen and D. R. Lovley (2012). "Electrical conductivity in a mixed-species biofilm." Appl Environ Microbiol **78**(16): 5967-5971.
- Malvankar, N. S., T. Mester, M. T. Tuominen and D. R. Lovley (2012). "Supercapacitors based on c-type cytochromes using conductive nanostructured networks of living bacteria." Chemphyschem **13**(2): 463-468.
- Malvankar, N. S., M. T. Tuominen and D. R. Lovley (2012). "Biofilm conductivity is a decisive variable for high-current-density *Geobacter sulfurreducens* microbial fuel cells." Energy & Environmental Science **5**(2): 5790-5797.
- Malvankar, N. S., M. T. Tuominen and D. R. Lovley (2012). "Lack of cytochrome involvement in long-range electron transport through conductive biofilms and nanowires of *Geobacter sulfurreducens*." Energy & Environmental Science **5**(9): 8651-8659.
- Malvankar, N. S., M. Vargas, K. Nevin, P. L. Tremblay, K. Evans-Lutterodt, D. Nykypanchuk, E. Martz, M. T. Tuominen and D. R. Lovley (2015). "Structural basis for metallic-like conductivity in microbial nanowires." mBio **6**(2): e00084-00015.
- Malvankar, N. S., M. Vargas, K. P. Nevin, A. E. Franks, C. Leang, B. C. Kim, K. Inoue, T. Mester, S. F. Covalla, J. P. Johnson, V. M. Rotello, M. T. Tuominen and D. R. Lovley (2011). "Tunable metallic-like conductivity in microbial nanowire networks." Nature Nanotechnology **6**(9): 573-579.
- Malvankar, N. S., M. Vargas, K. P. Nevin, A. E. Franks, C. Leang, B. C. Kim, K. Inoue, T. Mester, S. F. Covalla, J. P. Johnson, V. M. Rotello, M. T. Tuominen and D. R. Lovley (2011). "Tunable metallic-like conductivity in microbial nanowire networks." Nat Nanotechnol **6**(9): 573-579.
- Malvankar, N. S., S. E. Yalcin, M. T. Tuominen and D. R. Lovley (2014). "Visualization of charge propagation along individual pili proteins using ambient electrostatic force microscopy." Nat Nanotechnol **9**(12): 1012-1017.
- Margoliash, E. and J. Lustgarten (1962). "Interconversion of horse heart cytochrome C monomer and polymers." J Biol Chem **237**: 3397-3405.

- Marsili, E., J. Sun and D. R. Bond (2010). "Voltammetry and Growth Physiology of *Geobacter sulfurreducens* Biofilms as a Function of Growth Stage and Imposed Electrode Potential." Electroanalysis **22**(7-8): 865-874.
- Mattle, D., A. Zeltina, J.-S. Woo, B. A. Goetz and K. P. Locher (2010). "Two stacked heme molecules in the binding pocket of the periplasmic heme-binding protein HmuT from *Yersinia pestis*." Journal of molecular biology **404**(2): 220-231.
- Mehta, T., M. V. Coppi, S. E. Childers and D. R. Lovley (2005). "Outer membrane *c*-type cytochromes required for Fe (III) and Mn (IV) oxide reduction in *Geobacter sulfurreducens*." Applied and Environmental Microbiology **71**(12): 8634-8641.
- Methe, B. A., K. E. Nelson, J. A. Eisen, I. T. Paulsen, W. Nelson, J. F. Heidelberg, D. Wu, M. Wu, N. Ward, M. J. Beanan, R. J. Dodson, R. Madupu, L. M. Brinkac, S. C. Daugherty, R. T. DeBoy, A. S. Durkin, M. Gwinn, J. F. Kolonay, S. A. Sullivan, D. H. Haft, J. Selengut, T. M. Davidsen, N. Zafar, O. White, B. Tran, C. Romero, H. A. Forberger, J. Weidman, H. Khouri, T. V. Feldblyum, T. R. Utterback, S. E. Van Aken, D. R. Lovley and C. M. Fraser (2003). "Genome of *Geobacter sulfurreducens*: metal reduction in subsurface environments." Science **302**(5652): 1967-1969.
- Moore, E. J. and R. Fasan (2019). "Effect of proximal ligand substitutions on the carbene and nitrene transferase activity of myoglobin." Tetrahedron **75**(16): 2357-2363.
- Nevin, K. P., B. C. Kim, R. H. Glaven, J. P. Johnson, T. L. Woodard, B. A. Methé, R. J. DiDonato Jr, S. F. Covalla, A. E. Franks, A. Liu and D. R. Lovley (2009). "Anode biofilm transcriptomics reveals outer surface components essential for high density current production in *Geobacter sulfurreducens* fuel cells." PLoS ONE **4**(5): e5628.
- Nevin, K. P. and D. R. Lovley (2000). "Lack of production of electron-shuttling compounds or solubilization of Fe(III) during reduction of insoluble Fe(III) oxide by *Geobacter metallireducens*." Appl Environ Microbiol **66**(5): 2248-2251.
- Nevin, K. P. and D. R. Lovley (2002). "Mechanisms for Fe(III) Oxide Reduction in Sedimentary Environments." Geomicrobiology Journal **19**(2): 141-159.
- Nevin, K. P., H. Richter, S. F. Covalla, J. P. Johnson, T. L. Woodard, A. L. Orloff, H. Jia, M. Zhang and D. R. Lovley (2008). "Power output and columbic efficiencies from biofilms of *Geobacter sulfurreducens* comparable to mixed community microbial fuel cells." Environ Microbiol **10**(10): 2505-2514.
- Nivaskumar, M. and O. Francetic (2014). "Type II secretion system: a magic beanstalk or a protein escalator." Biochim Biophys Acta **1843**(8): 1568-1577.
- O'Brien, J. P. and N. S. Malvankar (2016). "A Simple and Low-Cost Procedure for Growing *Geobacter sulfurreducens* Cell Cultures and Biofilms in Bioelectrochemical Systems." Curr Protoc Microbiol **43**: A 4K 1-A 4K 27.
- Oohora, K., N. Fujimaki, R. Kajihara, H. Watanabe, T. Uchihashi and T. Hayashi (2018). "Supramolecular hemoprotein assembly with a periodic structure showing heme-heme exciton coupling." Journal of the American Chemical Society **140**(32): 10145-10148.

- Park, I. and B.-C. Kim (2011). "Homologous overexpression of *omcZ*, a gene for an outer surface c-type cytochrome of *Geobacter sulfurreducens* by single-step gene replacement." *Biotechnology Letters* **33**(10): 2043.
- Paulite, M., Z. Fakhraai, I. T. Li, N. Gunari, A. E. Tanur and G. C. Walker (2011). "Imaging secondary structure of individual amyloid fibrils of a β 2-microglobulin fragment using near-field infrared spectroscopy." *Journal of the American Chemical Society* **133**(19): 7376-7383.
- Peisach, J., W. Blumberg, S. Ogawa, E. Rachmilewitz and R. Oltzik (1971). "The effects of protein conformation on the heme symmetry in high spin ferric heme proteins as studied by electron paramagnetic resonance." *Journal of Biological Chemistry* **246**(10): 3342-3355.
- Phillips, J. C., R. Braun, W. Wang, J. Gumbart, E. Tajkhorshid, E. Villa, C. Chipot, R. D. Skeel, L. Kalé and K. Schulten (2005). "Scalable molecular dynamics with NAMD." *Journal of Computational Chemistry* **26**(16): 1781-1802.
- Piciooreanu, C., I. M. Head, K. P. Katuri, M. C. van Loosdrecht and K. Scott (2007). "A computational model for biofilm-based microbial fuel cells." *Water Res* **41**(13): 2921-2940.
- Ponomarenko, N., J. Niklas, P. R. Pokkuluri, O. Poluektov and D. M. Tiede (2018). "Electron paramagnetic resonance characterization of the triheme cytochrome from *Geobacter sulfurreducens*." *Biochemistry* **57**(11): 1722-1732.
- Qian, X., T. Mester, L. Morgado, T. Arakawa, M. L. Sharma, K. Inoue, C. Joseph, C. A. Salgueiro, M. J. Maroney and D. R. Lovley (2011). "Biochemical characterization of purified *OmcS*, a c-type cytochrome required for insoluble Fe(III) reduction in *Geobacter sulfurreducens*." *Biochim Biophys Acta* **1807**(4): 404-412.
- Qin, N., S. Zhang, J. Jiang, S. G. Corder, Z. Qian, Z. Zhou, W. Lee, K. Liu, X. Wang and X. Li (2016). "Nanoscale probing of electron-regulated structural transitions in silk proteins by near-field IR imaging and nano-spectroscopy." *Nature communications* **7**(1): 1-8.
- Radon, M. (2014). "Spin-State Energetics of Heme-Related Models from DFT and Coupled Cluster Calculations." *J Chem Theory Comput* **10**(6): 2306-2321.
- Ramer, G., F. S. Ruggeri, A. Levin, T. P. Knowles and A. Centrone (2018). "Determination of polypeptide conformation with nanoscale resolution in water." *ACS nano* **12**(7): 6612-6619.
- Ravel, B. and M. Newville (2005). "ATHENA, ARTEMIS, HEPHAESTUS: data analysis for X-ray absorption spectroscopy using IFEFFIT." *Journal of synchrotron radiation* **12**(4): 537-541.
- Reardon, P. N. and K. T. Mueller (2013). "Structure of the type IVa major pilin from the electrically conductive bacterial nanowires of *Geobacter sulfurreducens*." *J Biol Chem* **288**(41): 29260-29266.

- Reghu, M., K. Väkiparta, Y. Cao and D. Moses (1994). "Pressure dependence of the conductivity and magnetoconductance in oriented iodine-doped polyacetylene." Physical Review B **49**(23): 16162.
- Reguera, G., K. D. McCarthy, T. Mehta, J. S. Nicoll, M. T. Tuominen and D. R. Lovley (2005). "Extracellular electron transfer via microbial nanowires." Nature **435**(7045): 1098-1101.
- Reguera, G., K. P. Nevin, J. S. Nicoll, S. F. Covalla, T. L. Woodard and D. R. Lovley (2006). "Biofilm and nanowire production leads to increased current in *Geobacter sulfurreducens* fuel cells." Appl Environ Microbiol **72**(11): 7345-7348.
- Richter, L. V., S. J. Sandler and R. M. Weis (2012). "Two isoforms of *Geobacter sulfurreducens* PilA have distinct roles in pilus biogenesis, cytochrome localization, extracellular electron transfer, and biofilm formation." J Bacteriol **194**(10): 2551-2563.
- Ross, D. E., S. L. Brantley and M. Tien (2009). "Kinetic characterization of OmcA and MtrC, terminal reductases involved in respiratory electron transfer for dissimilatory iron reduction in *Shewanella oneidensis* MR-1." Appl Environ Microbiol **75**(16): 5218-5226.
- Ruggeri, F., G. Longo, S. Faggiano, E. Lipiec, A. Pastore and G. Dietler (2015). "Infrared nanospectroscopy characterization of oligomeric and fibrillar aggregates during amyloid formation." Nature communications **6**(1): 1-9.
- Ruggeri, F., S. Vieweg, U. Cendrowska, G. Longo, A. Chiki, H. Lashuel and G. Dietler (2016). "Nanoscale studies link amyloid maturity with polyglutamine diseases onset." Scientific reports **6**(1): 1-11.
- Rygula, A., Majzner K., Marzec K. M., Kaczor A., Pilarczyk M. and B. M. (2013). "Raman spectroscopy of proteins: a review." Journal of Raman Spectroscopy **44**(8): 1061-1076.
- Sanders, A. M., T. S. Kale, H. E. Katz and J. D. Tovar (2017). "Solid-phase synthesis of self-assembling multivalent π -conjugated peptides." ACS omega **2**(2): 409-419.
- Schroder, I., E. Johnson and S. de Vries (2003). "Microbial ferric iron reductases." FEMS Microbiol Rev **27**(2-3): 427-447.
- Seyedi, S. S., M. M. Waskasi and D. V. Matyushov (2017). "Theory and electrochemistry of cytochrome c." The Journal of Physical Chemistry B **121**(19): 4958-4967.
- Silva, J. C., M. V. Gorenstein, G.-Z. Li, J. P. Vissers and S. J. Geromanos (2006). "Absolute quantification of proteins by LCMSE: a virtue of parallel MS acquisition." Molecular & Cellular Proteomics **5**(1): 144-156.
- Simone, R. F., A. Jozef, J. J. Sun, L. H. A., M. Raffaele and D. Giovanni (2015). "Influence of the β -sheet content on the mechanical properties of aggregates during amyloid fibrillization." Angewandte Chemie International Edition **54**(8): 2462-2466.
- Smith, D. M., M. Dupuis, E. R. Vorpapel and T. P. Straatsma (2003). "Characterization of electronic structure and properties of a Bis(histidine) heme model complex." J Am Chem Soc **125**(9): 2711-2717.

- Someya, T., Z. Bao and G. G. Malliaras (2016). "The rise of plastic bioelectronics." Nature **540**(7633): 379-385.
- Speers, A. M., D. L. Cologgi and G. Reguera (2009). "Anaerobic cell culture." Curr Protoc Microbiol **Appendix 4**: Appendix 4F.
- Sreerama, N. and R. W. Woody (2000). "Estimation of protein secondary structure from circular dichroism spectra: Comparison of CONTIN, SELCON, and CDSSTR methods with an expanded reference set." Analytical Biochemistry **287**(2): 252-260.
- Su, T. A., H. Li, M. L. Steigerwald, L. Venkataraman and C. Nuckolls (2015). "Stereo-electronic switching in single-molecule junctions." Nature Chemistry **7**: 215-220.
- Summers, Z. M., H. E. Fogarty, C. Leang, A. E. Franks, N. S. Malvankar and D. R. Lovley (2010). "Direct exchange of electrons within aggregates of an evolved syntrophic coculture of anaerobic bacteria." Science **330**(6009): 1413-1415.
- Tan, Y., R. Y. Adhikari, N. S. Malvankar, S. Pi, J. E. Ward, T. L. Woodard, K. P. Nevin, Q. Xia, M. T. Tuominen and D. R. Lovley (2016). "Synthetic biological protein nanowires with high conductivity." Small **12**: 4481-4485.
- Tan, Y., R. Y. Adhikari, N. S. Malvankar, S. Pi, J. E. Ward, T. L. Woodard, K. P. Nevin, Q. Xia, M. T. Tuominen and D. R. Lovley (2016). "Synthetic Biological Protein Nanowires with High Conductivity." Small **12**(33): 4481-4485.
- Tan, Y., R. Y. Adhikari, N. S. Malvankar, J. E. Ward, K. P. Nevin, T. L. Woodard, J. A. Smith, O. L. Snoeyenbos-West, A. E. Franks, M. T. Tuominen and D. R. Lovley (2016). "The Low Conductivity of *Geobacter uraniireducens* Pili Suggests a Diversity of Extracellular Electron Transfer Mechanisms in the Genus *Geobacter*." Front Microbiol **7**: 980.
- Tan, Y., R. Y. Adhikari, N. S. Malvankar, J. E. Ward, T. L. Woodard, K. P. Nevin and D. R. Lovley (2017). "Expressing the *Geobacter metallireducens* PilA in *Geobacter sulfurreducens* Yields Pili with Exceptional Conductivity." mBio **8**(1).
- Taylor, C. (1977). "The EPR of low spin heme complexes Relation of the τ_2g hole model to the directional properties of the g tensor, and a new method for calculating the ligand field parameters." Biochimica et Biophysica Acta (BBA)-Protein Structure **491**(1): 137-148.
- Torres, C. I., A. K. Marcus, H. S. Lee, P. Parameswaran, R. Krajmalnik-Brown and B. E. Rittmann (2010). "A kinetic perspective on extracellular electron transfer by anode-respiring bacteria." FEMS Microbiol Rev **34**(1): 3-17.
- Tschirhart, T., E. Kim, R. McKay, H. Ueda, H.-C. Wu, A. E. Pottash, A. Zargar, A. Negrete, J. Shiloach, G. F. Payne and W. E. Bentley (2017). "Electronic control of gene expression and cell behaviour in *Escherichia coli* through redox signalling." Nature Communications **8**: 14030.
- Turner, D. L., L. Brennan, A. C. Messias, M. L. Teodoro and A. V. Xavier (2000). "Correlation of empirical magnetic susceptibility tensors and structure in low-spin haem proteins." European Biophysics Journal **29**(2): 104-112.

- Valasatava, Y., C. Andreini and A. Rosato (2015). "Hidden relationships between metalloproteins unveiled by structural comparison of their metal sites." Sci Rep **5**: 9486.
- Vargas, M., N. S. Malvankar, P. L. Tremblay, C. Leang, J. Smith, P. Patel, O. Synoeyenbos-West, K. P. Nevin and D. R. Lovley (2013). "Aromatic amino acids required for pili conductivity and long-range extracellular electron transport in *Geobacter sulfurreducens*." mBio **4**(2): e00105-00113.
- Vickery, L., T. Nozawa and K. Sauer (1976). "Magnetic circular dichroism studies of myoglobin complexes. Correlations with heme spin state and axial ligation." Journal of the American Chemical Society **98**(2): 343-350.
- Vignon, G., R. Kohler, E. Larquet, S. Giroux, M. C. Prevost, P. Roux and A. P. Pugsley (2003). "Type IV-like pili formed by the type II secretin: specificity, composition, bundling, polar localization, and surface presentation of peptides." J Bacteriol **185**(11): 3416-3428.
- Villari, V., P. Mineo, E. Scamporrino and N. Micali (2012). "Role of the hydrogen-bond in porphyrin J-aggregates." Rsc Advances **2**(33): 12989-12998.
- Wang, D. L., M. T. Stankovich, L. H. Eng and H. Y. Neujahr (1991). "Redox properties of cytochrome c3 from *Desulfovibrio desulfuricans* NCIMB 8372: Effects of electrode materials and sodium chloride." Journal of Electroanalytical Chemistry and Interfacial Electrochemistry **318**(1): 291-307.
- Wang, F., M. Coureuil, T. Osinski, A. Orlova, T. Altindal, G. Gesbert, X. Nassif, E. H. Egelman and L. Craig (2017). "Cryoelectron Microscopy Reconstructions of the *Pseudomonas aeruginosa* and *Neisseria gonorrhoeae* Type IV Pili at Sub-nanometer Resolution." Structure **25**(9): 1423-1435 e1424.
- Wang, F., Y. Gu, O'Brien J. Patrick, S. M. Yi, S. E. Yalcin, Srikanth Vishok, C. Shen, D. Vu, N. L. Ing, A. I. Hochbaum, E. Egelman and N. Malvankar (2019). "Structure of microbial nanowires reveals stacked hemes that transport electrons over micrometers." Cell **177**(2): 361-369.
- Wang, J., Y. Zhong, X. Wang, W. Yang, F. Bai, B. Zhang, L. Alarid, K. Bian and H. Fan (2017). "pH-dependent assembly of porphyrin-silica nanocomposites and their application in targeted photodynamic therapy." Nano Letters **17**(11): 6916-6921.
- Wang, X., X. Ye and G. Zhang (2015). "Investigation of pH-induced conformational change and hydration of poly (methacrylic acid) by analytical ultracentrifugation." Soft Matter **11**(26): 5381-5388.
- Xiao, H., F. B. Peters, P.-Y. Yang, S. Reed, J. R. Chittuluru and P. G. Schultz (2014). "Genetic incorporation of histidine derivatives using an engineered pyrrolysyl-tRNA synthetase." ACS chemical biology **9**(5): 1092-1096.
- Xu, Z., Q. Liao, Y. Wu, W. Ren, W. Li, L. Liu, S. Wang, Z. Gu, H. Zhang and H. Fu (2012). "Water-miscible organic J-aggregate nanoparticles as efficient two-photon fluorescent nano-probes for bio-imaging." Journal of Materials Chemistry **22**(34): 17737-17743.

Yalcin, S. E., B. A. Legg, M. Yeşilbaş, N. S. Malvankar and J. Boily (2020). "Direct observation of anisotropic growth of water films on minerals driven by defects and surface tension." Science Advances **6**: eaaz9708.

Yang, H., S. Yang, J. Kong, A. Dong and S. Yu (2015). "Obtaining information about protein secondary structures in aqueous solution using Fourier transform IR spectroscopy." Nat. Protocols **10**(3): 382-396.

Yatsunyk, L. A., A. Dawson, M. D. Carducci, G. S. Nichol and F. A. Walker (2006). "Models of the cytochromes: Crystal structures and EPR spectral characterization of low-spin bis-imidazole complexes of (OETPP) FeIII having intermediate ligand plane dihedral angles." Inorganic chemistry **45**(14): 5417-5428.